Università degli Studi di Padova

Department of Industrial Engineering

Master Thesis in Electrical Engineering

Control implementation aspects for a switchable n-phase machine

Supervisor
Silverio Bolognani
Università degli studi di Padova

Co-supervisor
Luca Peretti
KTH Royal Institute of Technology

Master Candidate
Fabio Toffoli

Academic year 2019/2020

ABSTRACT

This work is part of a research project developed at the Division of Electrical Machines and Drives of KTH Royal Institute of Technology, Stockholm (Sweden), on an induction multiphase machine with variable phase/pole configuration. The thesis is structured in two different parts.

Part I focuses on the control aspects of the so-called Wound Independely-Controlled Stator Coil (WICSC) machine prototype. After an introduction on multiphase machines in general and a description of their advantages over three-phase counterparts, the Vector Space Decomposition (VSD) theory is presented. It is used to model and develop an appropriate control scheme for regular multiphase machines. Unfortunately, the WICSC prototype, with its unique features, do not fit very well in this theory. In fact, when VSD is used and a change in the number of phases is performed, the size of the mathematical system change as well. To overcome this issue, a technique called at KTH Harmonic Plane Decomposition (HPD) has been developed. With HPD the size of the mathematical system do not change with the machine configuration. To test this theory, some simulations with Matlab and Simulink on a regular six-phase machine have been performed. The goal of this tests is to exploit the HPD approach in order to develop a control strategy capable of running the six-phase machine as usual, but also in a "virtual three-phase" mode, and switch between the two configurations during operation.

Part II of the thesis deals instead with the set up of the test-bench of the WICSC prototype. In particular, it shows the core aspects of the project of three signal conditioning boards, with the following features: conversion from current signals to voltage signals via measuring resistors, anti-aliasing filters, conversion from single-ended to differential signals, Analog Digital Converter (ADC) input protection, and management of IGBTs' fault signals.

ABSTRACT (IN ITALIANO)

Il lavoro di questa tesi si inserisce all'interno di un progetto di sviluppo di un motore a induzione multifase condotto dal Dipartimento di Electrical Machines and Drives del KTH Royal Institute of Technology, Stoccolma (Svezia). Il protipo che si vuole esaminare presenta particolari caratteristiche di design che permettono una variazione del numero di fasi e/o del numero di coppie polari durante il normale funzionamento.

Nella prima parte dell'elaborato viene affrontato il problema del controllo del prototipo denominato Wound Independely-Controlled Stator Coil (WICSC). Innanzitutto vengono descritte le caratteristiche generali delle macchine multifase e i relativi vantaggi rispetto ad una macchina trifase come ad esempio: la riduzione della corrente di fase a parità di potenza sviluppata, un migliore contenuto armonico della forza magnetomotrice generata, una riduzione della pulsazione della coppia, e la possibilità di continuare ad operare la macchina anche in caso di guasto. In seguito, viene presentata una tecnica denominata Vector Space Decomposition (VSD) che permette di modelizzare e gestire il controllo della maggior parte delle macchine multifase. Tramite la trasformata di Clarke, in una macchina trifase si ottengono solitamente un piano (formato dagli assi α e β, o d e q) e un asse che rappresenta la componente omopolare. Invece la VSD, tramite una trasformazione generalizzata di Clarke, rappresentata da una matrice con rango pari al numero di fasi n, permette di ottenere un numero maggiore di piani o spazi vettoriali, ed eventualmente un asse rappresentante l'omopolare nel caso di n dispari. Si può dimostrare che tutti questi piani sono ortogonali tra loro. Gli spazi vettoriali vengono etichettati con le prime armoniche dispari fino al numero di fasi n. Infatti, le prime armoniche temporali dispari si distribuiscono esattamente in questo modo. Ad esempio, per una macchina con sei fasi nel primo spazio vettoriale troveremo la fondamentale, nel terzo le terze armoniche, e nel quinto le quinte armoniche. Tuttavia, anche le armoniche di ordine superiore si distribuiscono nei vari sottospazi secondo una logica che dipende dalla disposizione degli avvolgimenti nella macchina. La conversione elettromeccanica avviene nello spazio vettoriale della fondamentale, che può quindi essere controllato come in una normale macchina trifase. Per quanto riguarda gli altri sottospazi vettoriali può essere utile controllarli a catena chiusa con riferimenti nulli per limitare le armoniche. In alcuni casi particolari possono anche essere sfruttati per aumentare la coppia mediamente prodotta. Tuttavia il prototipo di tipo WICSC, con le sue particolari caratteristiche, mal si adatta alla teoria della VSD. Infatti, ogni volta che si vuole cambiare il numero di fasi, la dimensione delle matrici in gioco cambia con n. Per ovviare a

questo problema si è cercato di sviluppare ulteriormente la VSD per ottenere una base di spazi vettoriali che resti uguale al variare delle configurazioni. Questa nuova tecnica viene denominata al KTH Harmonic Plane Decomposition (HPD), e consiste nel fare costantemente riferimento alla VSD di un caso-base, capace di inglobare le informazioni relative anche alle altre configurazioni con diverso numero di fasi e coppie polari. Gli spazi vettoriali del caso-base diventano i cosiddetti piani armonici dell'HPD. Per mettere alla prova questo approccio, sono state svolte delle simulazioni con Matlab e Simulink, con il modello di una normale macchina con sei fasi. Lo scopo di queste simulazioni è di riuscire, sfruttando l'HPD, a far operare la macchina anche in una modalità che si potrebbe definire "trifase virtuale" in cui le correnti delle sei fasi si equivalgono a due a due. Viene quindi dimostrato come sia possibile sviluppare un tale sistema di controllo, e vengono esposti i risultati ottenuti.

La seconda parte della tesi riguarda invece la messa in servizio del banco di prova necessario a testare il sopracitato prototipo di macchina di tipo WICSC. In particolare, viene affrontato il progetto delle schede elettroniche di condizionamento di segnale, necessarie ad adattare agli ingressi del convertitore analogico-digitale i segnali provenienti da 36 sensori di corrente e 12 sensori di livello di tensione. Questi segnali vengono generati nei moduli di potenza atti ad alimentare il prototipo attraverso un inverter con 36 gambe. Le schede di condizionamento progettate integrano le seguenti funzioni:

- trasformazione di segnali in corrente in segnali in tensione tramite resistenze di misurazione;
- filtri anti-aliasing;
- conversione dei segnali da *single-ended* a *differential*;
- limitazione dei segnali in uscita con lo scopo di proteggere il convertitore analogico-digitale;
- gestione dei segnali di guasto degli IGBT.

Il progetto di alcune parti dello schema elettrico delle schede viene affrontato nel dettaglio e inoltre viene svolta l'analisi della stabilità degli amplificatori operazionali. Infine, viene presentato il design definitivo del circuito stampato.

CONTENTS

I CONTROL IMPLEMENTATION ASPECTS
1 INTRODUCTION 3
1.1 What is a MultiPhase Electric Drive? 3
1.2 Brief History and Evolution of Multiphase Electric Drives 3
1.3 Advantages of Multiphase Machines 5
2 MODELLING AND DRIVE TECHNIQUES FOR MULTIPHASE MACHINES 9
2.1 Types of multi-phase machines 9
2.1.1 Symmetric Multi-Phase Machines (MPMs) 9
2.1.2 Asymmetric MPMs 10
2.2 Generalized Clarke and Park transformations for multiphase machines 11
2.2.1 The fundamental winding configuration 11
2.2.2 The generalized Clarke transformation 13
2.2.3 Harmonic mapping 14
2.2.4 The generalized Park transformation 15
2.3 Modelling of a multiphase induction machine 16
2.3.1 The stator model 17
2.3.2 The rotor model 23
2.3.3 The complex vector equivalent circuit 27
2.3.4 The torque expression 29
2.3.5 Considerations 30
2.4 Control strategy with FOC and VSD 31
3 THE WICSC MACHINE AND THE HPD APPROACH 33
3.1 The WICSC machine 33
3.1.1 ISCAD 33
3.1.2 WICSC design 34
3.1.3 WICSC pole and phase changing capabilities 36
3.2 Harmonic plane decomposition 38
3.2.1 Vector-space distribution 40
3.2.2 Generation of current references 42
4 A SWITCHABLE THREE AND SIX PHASE MACHINE WITH HPD 45
4.1 Modelling of a six phase, concentrated windings, induction machine 45
4.2 HPD-based control technique 48
4.3 Simulations 54
4.3.1 Inclusion of dead-time effects 60
4.4 Conclusions of Part I and future developments 64

II SIGNAL CONDITIONING BOARD PROJECT
5 INTRODUCTION 71

- 5.1 Test-bench configuration 71
- 5.2 The aliasing phenomenon 72

6 ELECTRICAL CIRCUITS SCHEMES 75
- 6.1 Measuring resistance 75
- 6.2 Anti-aliasing filters 76
- 6.3 Single-ended to differential signal conversion 77
  - 6.3.1 ADC compability issues 78
  - 6.3.2 ADC input requirements 80
  - 6.3.3 Conversion implementation with FDA 80
- 6.4 Final configuration of current and voltage measurement channels 82
  - 6.4.1 Ranges 82
  - 6.4.2 Frequency response 84
  - 6.4.3 DC response 84
- 6.5 Fault signals 84

7 STABILITY ANALYISIS 91

8 PCB DESIGN AND CONCLUSIONS 99
- 8.1 PCB design 99
- 8.2 Conclusions of Part II 101

CONCLUSIONS 103

BIBLIOGRAPHY 105

LIST OF FIGURES

Figure 2.1 Examples of symmetric MPMs. 9
Figure 2.2 A six-phase symmetric MPM 10
Figure 2.3 A six-phase asymmetric or split-phase MPM ($N = 2, m = 3$) 10
Figure 2.4 Transform flow principle of VSD 11
Figure 2.5 Reference frames of a five-phase symmetric MPMs. 12
Figure 2.6 Reference frames of a six-phase asymmetric MPMs. 12
Figure 2.7 Ideal winding function for the distributed winding case. 18
Figure 2.8 Ideal winding function for the concentrated winding case, and its Fourier series expansion with three terms. 18
Figure 2.9 Schematic of the squirrel cage rotor and definition of the elementary loops for mutual inductance calculation, [24]. 20
Figure 2.10 Ideal winding function for the j-th rotor bar in a squirrel-cage induction machine rotor, for n_b=12. 21
Figure 2.11 Model of the squirrel cage rotor with 12 rotor bars, [24]. 23
Figure 2.12 Relationship between stationary and rotating reference frames. 28
Figure 2.13 Complex vector equivalent circuit for the k-th vector subspace. 29
Figure 2.14 Control scheme for an Indirect Rotor Field Oriented Control (IRFOC) of a six-phase MPM. 32
Figure 3.1 Intelligent Stator CAge Drive (ISCAD) concept, [30]. 34
Figure 3.2 Gramme-type winding on the WICSC machine, wound around the stator core. 34
Figure 3.3 Renderings and picture of the WICSC prototype, without the rotor except for (c). 35
Figure 3.4 Schematic of the driveline of the prototype. 36
Figure 3.5 Virtual phase concept for the WICSC machine, side sectional view (18 phases - 2 poles configuration). 37
Figure 3.6 Some of the possible configurations for the WICSC machine. 38

Figure 3.7 A six-phase YY30 machine in a three-phase configuration. 39
Figure 3.8 HPD ($m_b = 18, p_b = 1$) of a three-phase/2 poles configuration. 41
Figure 3.9 HPD ($m_b = 18, p_b = 1$) of a six-phase/2 poles configuration, with 3-rd, 5-th, and 13-th time harmonics of the same amplitude of the fundamental in the instantaneous values of the currents in $abc/123$ reference frame. 43
Figure 4.1 Vector model of the $k - th$ vector subspace/harmonic plane in a stationary reference frame. 46
Figure 4.2 Model of the 3-rd vector subspace/harmonic plane. 47
Figure 4.3 Scheme of the motor model. 48
Figure 4.4 IRFOC scheme. 48
Figure 4.5 VSD coincident with HPD ($m_b = 6$) for the six-phase configuration. 51
Figure 4.6 HPD ($m_b = 6$) for the three-phase configuration. 52
Figure 4.7 Control scheme. 53
Figure 4.8 Simulation results (switch of configuration at $t = 30s$). 55
Figure 4.9 Simulation results (switch of configuration at $t = 30s$), details (beware of the different time-scale for the rotor). 56
Figure 4.10 Simulation results: HPD of reference voltages and consequent stator currents. 57
Figure 4.11 Improved control scheme, current references. 57
Figure 4.12 Simulation results with improved control scheme (switch of configuration at $t = 30s$). 58
Figure 4.13 Simulation results with improved control scheme (switch of configuration at $t = 30s$), details (beware of the different time-scale for the rotor). 59
Figure 4.14 Comparison between two different control schemes, detail of speed and torque (switch of configuration at $t = 30s$). 60
Figure 4.15 Dead-time effects on a leg voltage. 61
Figure 4.16 Simulation results with dead-time effects (switch of configuration at $t = 30s$). 62
Figure 4.17 Simulation results with dead-time effects (switch of configuration at $t = 30s$), details (beware of the different time-scale for the rotor). 63
Figure 4.18 Simulation results with dead-time effects: HPD of reference voltages and consequent stator currents. 64

Figure 4.19 Fast Fourier Transform (FFT) of a stator phase current. 65
Figure 5.1 Schematic representation of the test-bench configuration for the WICSC prototype. 71
Figure 5.2 Intelligent Power Module (IPM) pictures. 72
Figure 5.3 Sampling effects. 73
Figure 6.1 Implementation of the current transducer 75
Figure 6.2 Measuring resistance circuit. 75
Figure 6.3 General Sallen-key low-pass filter. 76
Figure 6.4 Anti-aliasing filter scheme of one current measurement channel. 77
Figure 6.5 Anti-aliasing filter scheme of one voltage measurement channel. 77
Figure 6.6 Differential double balun input configuration for baseband applications, [1] 78
Figure 6.7 AC transfer characteristics, input configuration of the AD9249-65EBZ. 79
Figure 6.8 Modifications to be done on the analog-front end of the AD9249-65EBZ. 79
Figure 6.9 AD9249-65EBZ before and after the required modifications 80
Figure 6.10 AD9249 input requirements 81
Figure 6.11 Single-ended bipolar input circuit, [17]. 81
Figure 6.12 Transient simulation of the current measurement channel outputs, when the input is a $1V$ amplitude, $50Hz$, sine wave. 83
Figure 6.13 Transient simulation of the current measurement channel outputs, when the input is a $2V$ amplitude, $50Hz$, sine wave. 83
Figure 6.14 Complete scheme of one current measurement channel. 85
Figure 6.15 Complete scheme of one voltage measurement channel. 86
Figure 6.16 AC transfer characteristics of the current measuring channel. 87
Figure 6.17 AC transfer characteristics of the voltage measuring channel. 87
Figure 6.18 DC transfer characteristics of the current measuring channel. 88
Figure 6.19 DC transfer characteristics of the voltage measuring channel. 88
Figure 6.20 Fault signals management 89
Figure 7.1 Control loop equivalent scheme of a feedback op amp circuit. 91
Figure 7.2 Control loop equivalent scheme of a dual feedback op amp circuit. 92

Figure 7.3 Double L Loop Gain Break Test circuit, example. 92
Figure 7.4 Double L Loop Gain Break Test circuit, filter of current measurement channel. 93
Figure 7.5 Loop gain AC transfer characteristics, filter of current measurement channel. 93
Figure 7.6 Double L Loop Gain Break Test circuit, filter of voltage measurement channel. 94
Figure 7.7 Loop gain AC transfer characteristics, filter of voltage measurement channel. 94
Figure 7.8 Loop gain test circuit, Fully Differential Amplifier (FDA). 95
Figure 7.9 Loop gain AC transfer characteristics, FDA. 95
Figure 7.10 Loop gain test circuit, buffer of the FDA's V_{ocm} reference. 96
Figure 7.11 Loop gain AC transfer characteristics, buffer. 96
Figure 7.12 Loop gain AC transfer characteristics with added output isolation resistor, buffer. 97
Figure 8.1 Rendering of the signal conditioning board, front side. 100
Figure 8.2 Signal conditioning board picture. 101

LIST OF TABLES

Table 2.1 Stator self inductance, stator leakage inductance, stator-rotor mutual inductance, for each vector subspace, for five-phase and six-phase machines, distributed or full-pitch concentrated windings, analytically obtained as described in [28]. 22
Table 2.2 Rotor self inductance, rotor-stator mutual inductance, for each vector subspace, for five-phase and six-phase machines, distributed or full-pitch concentrated windings, analytically obtained as described in [28]. 26
Table 3.1 Phase and pole configurations 37
Table 4.1 Parameters of the considered YY30 six-phase motor. 49

ACRONYMS

PWM	Pulse Width Modulation
IM	Induction Machine
MPM	Multi-Phase Machine
FOC	Field Oriented Control
IRFOC	Indirect Rotor Field Oriented Control
ADC	Analog Digital Converter
PCB	Printed Circuit Board
WICSC	Wound Independely-Controlled Stator Coil
ISCAD	Intelligent Stator CAge Drive
FPGA	Field Programmable Gate Array
FMC	FPGA Mezzanine Card
VSD	Vector Space Decomposition
DSP	Digital Signal Processor
MMF	Magneto-Motive Force
DOF	Degree Of Freedom
HPD	Harmonic Plane Decomposition
EV	Electric Vehicle
DFT	Discrete Fourier Transformation
FFT	Fast Fourier Transform
THD	Total Harmonic Distortion
IPM	Intelligent Power Module
FDA	Fully Differential Amplifier
SMD	Surface-Mount Device

Part I

CONTROL IMPLEMENTATION ASPECTS

In the first part of the thesis, the theoretical aspects of the control approach for the multiphase induction machine developed at KTH Royal Institute of Technology, the so called WICSC machine, will be discussed. In chapter 1 the multiphase electric drives field is introduced. Chapter 2 presents how regular Multi-Phase Machines (MPMs) can be modelled and driven, while in Chapter 3 the focus is on the peculiarities of the WICSC machine. A possible control scheme is presented, which is able to deal with an on-the-fly change of the number of phases, without any electromechanical switch. Finally, in chapter 4 a simplified version of the control algorithm is tested with some simulations and conclusions are drawn.

1

INTRODUCTION

In the last couple of decades the area of multiphase electric drives has experienced a substantial growth and re-emerged as potential solution for various industrial applications. The use of three-phase drives continue to be the default choice, but there is a trend to reevaluate the optimum number of phases for certain applications, especially where the whole system is built from scratch, and machine and converter may not be available off-the-shelf. At KTH Royal Institute of Technology a research group, lead by teachers Peretti L. and Wallmark O., is setting up a prototype of a multiphase induction machine with even more complexity than a regular multiphase machine. The project, in collaboration with Scania AB and ABB, aims at building and studying a reduced-scale prototype of the so-called WICSC machine, as introduced by Bitsi, Wallmark and Bosga in [3]. The prototype is still a preliminary solution and it does not cover all the design features of the original idea, which aims to a solution for propulsion in electric trucks. However, the basic concept of a variable phase/pole machine and its related control can be tested with such prototype.

1.1 WHAT IS A MULTIPHASE ELECTRIC DRIVE?

An electric machine is termed multiphase if the stator number of phases is higher than three ($n > 3$). This is usually achieved by redesigning the stator frame or simply rewinding the stator of a three-phase machine to obtain n independent windings and $2n$ terminals. In a multiphase electric drive, the electromechanical energy conversion is achieved using a multiphase machine that is supplied from a multiphase converter using a particular control strategy. The control action needs especially to take into account some additional degrees of freedom that are unique of multiphase systems, enabling unconventional modes of operation.

1.2 BRIEF HISTORY AND EVOLUTION OF MULTIPHASE ELECTRIC DRIVES

Although the first record of a multiphase motor drive dates back to 1969 [36], in the next 20 years it attracted a limited attention because in those days both microprocessors and power electronics were still in an early stage of development. In the early 1980s there was a first proposal for a fault-tolerant multiphase drive [15], and in the early 1990s it was demonstrated the capability of multiphase drives to increase the power density by injecting specific current harmonics [34]. During the 1990*s* the pace started accelerating thank to the steady improvements in power electronics and the maturation of the theory, but it was not until the beginning of this century that multiphase motor drives became valid alternatives for various applications. In the first decade another important feature of multiphase machines was tested, i.e. the capability to independently control different machines supplied by the same inverter [12]. The development continued to increase extending the use of multiphase drives to different applications and covering different topologies, types of converters, machine design, winding arrangements, control strategies, modulation techniques, and innovative modes of operation. If we restrict to Induction Machines (IMs), which share the working principle with the WICSC machine, we realize that nowadays an increasing number of them are not connected anymore directly to three-phase supplies. Instead they are fed from a power electronic converter (the input of which is connected to a three-phase supply). The output stage of the converter has to match the number of phases of the stator winding of the electrical machine, but provided this simple requirement is met, any number of phases may be used. In the era of extremely powerful Digital Signal Processors (DSPs), the three-phase paradigm needs to be revisited and it becomes necessary to rethink and research which is the optimum solution for each specific application. Some companies have followed this path and as a result multiphase drives have been successfully used and resulted predominant in three specific areas in particular, namely electric ship propulsion, traction (including electric and hybrid vehicles) and the concept of "more-electric" aircraft (examples are aircraft actuators for the nose wheel steering or the engine fuel pump). A detailed overview of the state-of-the-art in the area of multiphase electric drives in general, and in multiphase induction motor drives in particular, has been made by Emil Levi et al. in [7], [18] and [19]. A more recent review, made by a research group from Tsinghua University, highlights the various developments on MPMs that are being made by different research groups spread worldwide [21]. Among the many we can cite T. A. Lipo's group from the University of Winsconsin-Madison, which first introduced a Field Oriented Control (FOC) technique for a six phase (dual three-phase) IM called Vector Space Decomposition (VSD) [40], also under open-circuit faults [41], and the research group lead by the already mentioned E. Levi from Liverpool John Moores University, which spent effort on the Pulse Width Modulation (PWM) techniques of multiphase converters [6].

1.3 ADVANTAGES OF MULTIPHASE MACHINES

The following are some of the potential benefits of MPMs that may justify the increased complexity, as described in [28] and in the others aforementioned reports.

- *Reduction of phase currents at constant power and voltage levels:* the first advantage of a MPM is the capability of lowering the current rating per phase by keeping the same voltage and power ratings of a conventional three-phase machine. The equation of the active power in a n-phase balanced system is:

  $$P = \frac{n}{2} \cdot \hat{U} \cdot \hat{I} \cdot \cos(\phi) \tag{1.1}$$

  where P is the active power, $\hat{U}$ is the peak voltage, $\hat{I}$ is the peak current, and $\cos(\phi)$ is the power factor. By keeping the same P and $\hat{U}$, and approximately a similar power factor, it is immediate that lower values of $\hat{I}$ can be obtained by increasing the phase number n. This can be beneficial in high-power applications where $\hat{U}$ is kept costant, but the converters cannot provide the required current in three-phase machines due to semiconductor technological reasons.

- *Space harmonics related to the generated Magneto-Motive Force (MMF):* the MMF distribution around the air gap, interacting with time harmonics introduced by sinusoidal or non-sinusoidal input voltages at the machine terminals, generate space harmonics that affect the flux linkage geometric distribution, ultimately affecting the torque. [37] shows how an increase in the number of phases n causes a shift of the space harmonics (different from the fundamental one), induced by the fundamental frequency excitation, towards the higher frequencies, i.e. making the MMF a "smoother" sinusoidal wave. However it is also shown that for others time harmonics in the excitation, low order space harmonics could be generated depending on the value of n. On the stator Joule losses perspective [37] shows that a five-phase machine could theoretically achieve 5.75% less losses than the three-phase counterpart. This reduction, though, does not increase sensibly more than that, as it shown that an hypothetical machine with infinite number of phases would bring a loss reduction of 8.81%. Generally speaking there is some potential for loss reduction, but the overall efficiency greatly depends on the geometric design (not considered in this discussion), and by the control strategy.

- *Torque pulsations:* in general terms pulsating torques arise from the interaction between air-gap field components with the same pole number but rotating at different speeds. The product of the magnitude of the two interacting fields determine the magnitude of the torque pulsation, while its frequency depends on the difference between their speeds. Again [37] shows that the largest magnitude torque pulsations are those that arise when the main $2p$-pole field is involved. The time harmonics components of the excitation that can generate a $2p$-pole field are of order q, determined by:

$$q = 2kn \pm 1, \qquad k = 1, 2, 3, \ldots \tag{1.2}$$

In particular the time harmonic of order $2kn + 1$ generates a $2p$-pole field that rotates in the same direction as the main field (but $2kn + 1$times faster), while the time harmonic of order $2kn - 1$ generates a $2p$-pole field that rotates backwards (and $2kn - 1$ times faster) respect to the main field. In both cases the frequency of the resulting torque pulsation is given by:

$$\omega_{pulse} = 2kn\omega \tag{1.3}$$

where ω is the pulsating frequency of the fundamental excitation (i.e. of the main field). Equation (1.2) may be used to determine which excitation harmonics are potentially troublesome and should be avoided. For example, for a nine-phase machine the excitation harmonics to avoid are of order $18k \pm 1$ (i.e. 17th, 19th, 35th, 37th, etc.), because if present (1.3) shows that pulsations at 18 and 36 times the main excitation frequency will be produced. These results where produced assuming a smooth air-gap surface on both stator and rotor. The effect of stator and rotor slotting is to perturb the harmonic fields, and hence it is more difficult to make general statements on the relative merits of multiphase machines. Anyhow (1.3) indicates that the torque pulsations are located at higher frequencies if multi-phase designs are chosen and if avoiding in the voltage source those frequencies identified by (1.2) is not possible, the fact that by nature the higher time harmonics are usually of lower magnitude may help in further reducing the magnitude of the torque pulsations in multi-phase designs.

- *Fault handling:*
  a multi-phase machine can continue to operate with a rotating field as long as no more than $n - 3$ phases are faulted [18, 19]. In other words, as long as a minimum of three phases are guaranteed, a rotating magnetic field can be produced to make rotate the machine, although with different power/torque ratings. The amount of power and torque that can be produced depends on the fault strategy, but also on the machine design. For instance, six-phase machines built with a split-phase configuration (two sets of three-phase windings spatially shifted by 30 electric de-

grees) will have different fault handling possibilities depending on whether the star point is isolated between the two sets of windings, or not. In the first case, the typical fault handling strategy in case of a phase loss is the removal of a complete set of three-phase windings (clearly the one containing the faulted phase), thus reducing by 50% the rating of the machine. Different possibilities are available with a common star point connection, where the current shape can be altered in order to maintain a rotating magnetic field (introducing some asymmetry in the currents, though). Some fault-tolerant strategies are:

  - keep the current magnitude in the remaining phases as before: this approximately reduces the stator Joule losses by a factor of $(n-1)/n$, when one phase is faulted;
  - Increase the current magnitude in the healthy phases by a factor $\sqrt{n/(n-1)}$, keeping approximately the same stator Joule losses;
  - Increase the current magnitude in the healthy phases by a factor $n/(n-1)$, increasing the stator Joule losses but keeping the same torque level.

- *Exploitation of the increased Degrees Of Freedom (DOFs)*:
  since only two currents are required for the average flux or average torque control, regardless of the number of phases, the remaining DOFs can be exploited for other purposes, such as:

  - *Enchance torque density:*
    the presence of space harmonics usually just cause unwanted currents and torque ripple in conventional three-phase machines, but in MPMs could possibly be used for generating average torque and thus increase the torque density of some specific designs. This is usually achieved injecting some precise time harmonics in the current in machines with concentrated windings. Furthermore this phenomenon is better appreciated in odd-phase symmetric machines (i.e. machines with five, seven, nine phases, etc.). According to [34], the highest gain, of at least 10% compared to conventional three-phase IMs, seems to be achieved with five-phase machines and an injection of third harmonics in the stator currents. On the downside this causes presence of harmonics in the air-gap flux, increasing the flux density and therefore the iron losses.

  - *Multimotor drive systems:*
    only for machines with sinusoidal MMF distribution, it is possible to independently control multiple multiphase machines in series with a single power electronic converter supply, [18]. This is achieved with a suitable transposition

in the connection of the machine's phases, in such a manner that flux/torque producing components (in VSD) of one machine appear as non flux/torque producing currents for all the others machine and viceversa.

2

MODELLING AND DRIVE TECHNIQUES FOR MULTIPHASE MACHINES

In this chapter we see how regular multiphase machines are usually approached, from the modelling to the control strategy. We will follow the most important passages described in [28], in which a general approach methodology is proposed, and we will focus on Induction Machines (IMs). This is necessary in order to understand why the proposed WICSC machine will need some extraordinary expedients.

2.1 TYPES OF MULTI-PHASE MACHINES

There exist two main types of Multi-Phase Machines (MPMs), i.e. the symmetric and the asymmetric ones.

2.1.1 *Symmetric MPMs*

In symmetric MPMs, the phases are equally distributed over the stator circumference with a displacement angle of $2\pi/n$ electric radians. This machine type is an extension of the conventional symmetric three-phase machine as shown in Fig. 2.1. The arrows represent the direction of the positive magnetomotive force produced by a machine phase, while the dashed lines indicate the negative magnetomotive force direction in the same phase. Note that in case of symmetric machines with an even number of phases, each phase shares the magnetic axis with another phase, and the magnetomotive force of a phase adds or subtracts from the one produced by a phase in the opposite direction. Fig. 2.2 shows the example of a six-phase

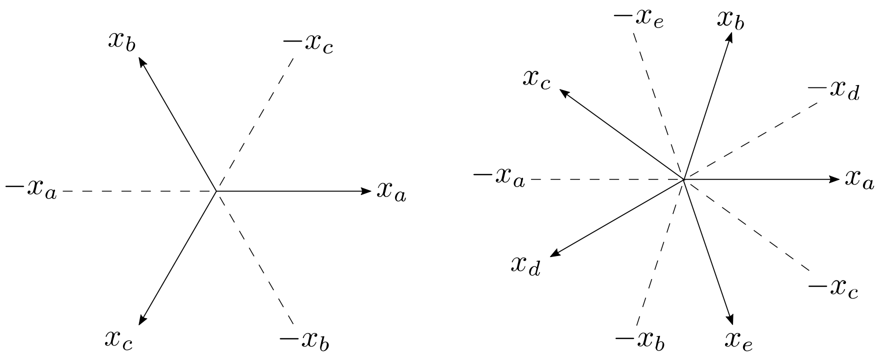

(a) Three-phase.

(b) Five-phase.

Figure 2.1: Examples of symmetric MPMs.

symmetric MPM, where it is evident that such machine is topologically not different from a three-phase counterpart, since producing positive magnetomotive force sequentially in the symmetric six-phase machine can be equally achieved in the three-phase machine with positive and negative magnetomotive force sequences. For this reason, even-phase symmetric machines are not of significant importance.

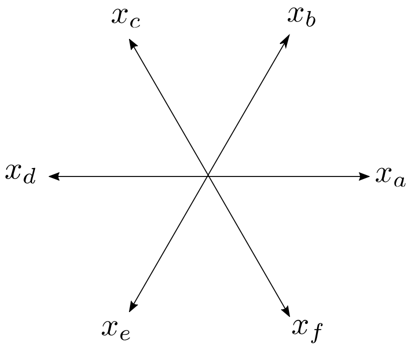

Figure 2.2: A six-phase symmetric MPM

2.1.2 *Asymmetric MPMs*

In asymmetric multi-phase machines (also known as split-phase or multiple-star machines), a number N of identical m-phase sets are geometrically distributed with a displacement of $\pi/(mN)$ electric radians between the different sets. The most common case of split-phase machines combines N identical three-phase sets ($m = 3$), i.e. with a displacement of $\pi/3N$ electric radians between the sets. Fig. 2.3 shows the example of a six-phase MPM with 2 three-phase sets displaced of 30 electric degrees (also known as YY30). There exists also some machines with $m \neq 3$, a common one is for example the ten-phase machine with two five-phase sets displaced of 10 electrical degrees. However only asymmetric MPMs with $m = 3$, differently from the sym-metric MPMs, have the potential advantage that they may be supplied by N three-phase converters.

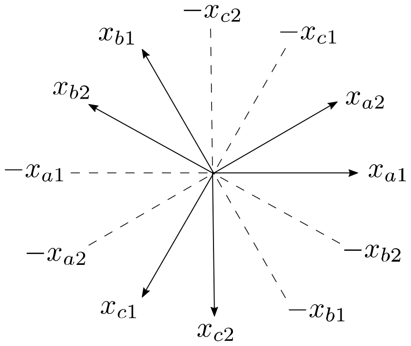

Figure 2.3: A six-phase asymmetric or split-phase MPM ($N = 2, m = 3$)

2.2 GENERALIZED CLARKE AND PARK TRANSFORMATIONS FOR MULTI-PHASE MACHINES

In order to approach the analytical modelling and the control of MPMs, one of the most important steps are the transformations between stationary and rotating reference frames. The generalized transformations methodology, has been introduced in [40] and [29], starting from an approach known as Vector Space Decomposition (VSD). The method is general for any number of phases, for symmetric and asymmetric machines, employs matrices with real values, leads two main d and q currents as in the conventional three-phase theory, and in addition is able to describe the behaviour of higher harmonics in the machine. This is not achievable when conventional three-phase dq models are put in parallel as one could do for example to describe an asymmetric split-phase machines with m three-phase sets. Compared to conventional $\alpha\beta 0$ and $dq0$ for three-phase machines, VSD requires an intermediate reference frame named "fundamental winding configuration". Except from that, the remaining approach is the same, with the only difference that it involves n-by-n matrices. Fig. 2.4 shows the transform flow principle of VSD, where $\mathbf{x}$ is a vector representing any machine variable (for example current or voltage vectors).

$$\begin{tikzcd}
\mathbf{x}_{abc} \arrow[r, "\mathbf{T}_{abc\rightarrow 123}"] & \mathbf{x}_{123} \arrow[r, "\mathbf{T}_{123\rightarrow \alpha\beta 0}"] & \mathbf{x}_{\alpha\beta 0} \arrow[r, "\mathbf{T}_{\alpha\beta 0\rightarrow dq0}"] & \mathbf{x}_{dq0} \\
\text{Practical} & \text{Fundamental} & \text{Stator} & \text{Rotor} \\
\text{ref. frame} & \text{ref. frame} & \text{ref. frame} & \text{ref. frame}
\end{tikzcd}$$

Figure 2.4: Transform flow principle of VSD

2.2.1 *The fundamental winding configuration*

The fundamental winding reference frame (or fundamental winding configuration) was introduced so that the generalized Clarke transformation could be applied without any concerns about the machine phase topology, [29]. It is applied to the so-called practical configuration (also known as actual or natural configuration) which is simply the schematic representation of the phases as already shown in Sect. 2.1. The fundamental winding configuration is a reference frame where the phases are shifted by $\delta = \pi/n$ electric radians. Independently on whether the machine is of the symmetric or asymmetric type, it is always composed by a sequence of n phases with the same phase shift between them, as well explained by Fig. 2.5 and Fig. 2.6 where practical and fundamental winding configurations are shown for a five-phase symmetric and a six-phase asymmetric machines, respectively. With $\mathbf{x}_{abc}$ we refer to the general vector describing any machine variable in the practical reference frame, regardless the num-

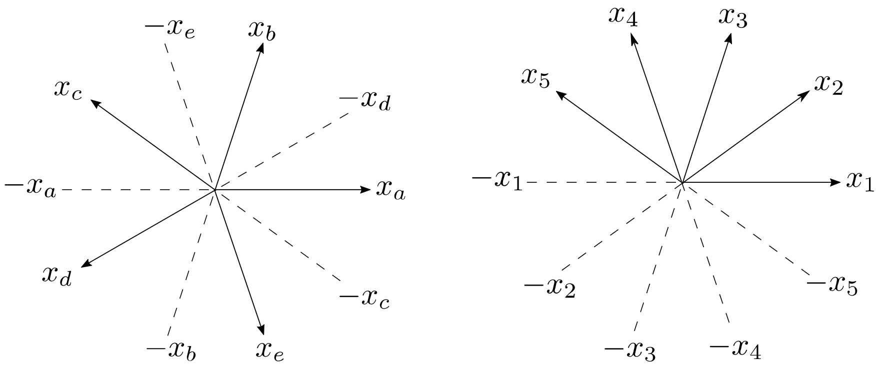

(a) Practical reference frame. (b) Fundamental reference frame.

Figure 2.5: Reference frames of a five-phase symmetric MPMs.

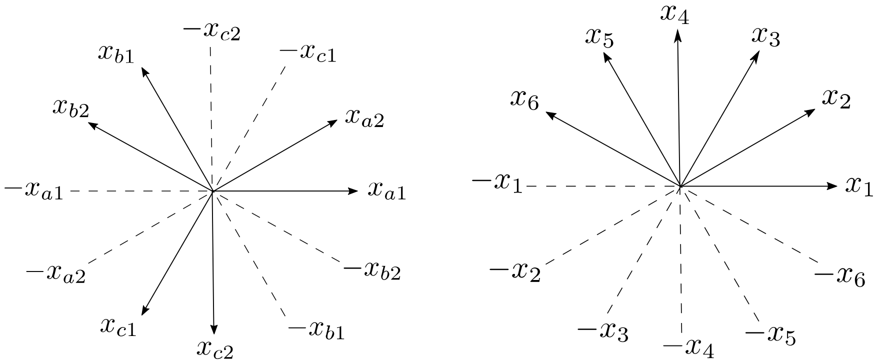

(a) Practical reference frame. (b) Fundamental reference frame.

Figure 2.6: Reference frames of a six-phase asymmetric MPMs.

ber of phases. For the five-phase symmetric MPM it assumes the form $\mathbf{x}_{abc} = [x_a \; x_b \; x_c \; x_d \; x_e]^T$, while for the six-phase asymmetric MPM it is $\mathbf{x}_{abc} = [x_{a1} \; x_{b1} \; x_{c1} \; x_{a2} \; x_{b2} \; x_{c2}]^T$ with the conventional use of the first set of three phases followed by the second set of three phases. Similarly, with $\mathbf{x}_{123}$, we refer to the fundamental reference frame, regardless of the number of phases. The transformation matrix $\mathbf{T}_{abc \to 123}$, which has dimension n-by-n and whose elements depend on whether the machine is symmetric or asymmetric, can be found with a simple comparison between Fig. 2.5a and Fig. 2.5b for the five-phase symmetric machine, and between Fig. 2.6a and Fig. 2.6b for the six-phase asymmetric one. For the five-phase symmetric MPM we get:

$$\mathbf{x}_{123} = \mathbf{T}_{abc\to 123} \cdot \mathbf{x}_{abc} \tag{2.1}$$

$$\begin{bmatrix} x_1 \\ x_2 \\ x_3 \\ x_4 \\ x_5 \end{bmatrix} = \begin{bmatrix} 1 & 0 & 0 & 0 & 0 \\ 0 & 0 & 0 & -1 & 0 \\ 0 & 1 & 0 & 0 & 0 \\ 0 & 0 & 0 & 0 & -1 \\ 0 & 0 & 1 & 0 & 0 \end{bmatrix} \times \begin{bmatrix} x_a \\ x_b \\ x_c \\ x_d \\ x_e \end{bmatrix}. \tag{2.2}$$

Instead for the six-phase asymmetric MPM we get:

$$\mathbf{x}_{123} = \mathbf{T}_{abc\to 123} \cdot \mathbf{x}_{abc} \tag{2.3}$$

$$\begin{bmatrix} x_1 \\ x_2 \\ x_3 \\ x_4 \\ x_5 \\ x_6 \end{bmatrix} = \begin{bmatrix} 1 & 0 & 0 & 0 & 0 & 0 \\ 0 & 0 & 0 & 1 & 0 & 0 \\ 0 & 0 & -1 & 0 & 0 & 0 \\ 0 & 0 & 0 & 0 & 0 & -1 \\ 0 & 1 & 0 & 0 & 0 & 0 \\ 0 & 0 & 0 & 0 & 1 & 0 \end{bmatrix} \times \begin{bmatrix} x_{a1} \\ x_{b1} \\ x_{c1} \\ x_{a2} \\ x_{b2} \\ x_{c2} \end{bmatrix}. \tag{2.4}$$

For any multi-phase machine type with any value of n, N or m the transformation matrix $\mathbf{T}_{abc\to 123}$ is orthogonal [29], which leads to the property:

$$\mathbf{T}_{123\to abc} = \left(\mathbf{T}_{abc\to 123}\right)^{-1} = \left(\mathbf{T}_{abc\to 123}\right)^{T}. \tag{2.5}$$

2.2.2 *The generalized Clarke transformation*

The development of the generalized transformation follows Clarke's main passages starting from the method of symmetric components [10], where the most relevant modification is performed. The operator $\underline{\alpha} = e^{j2\pi/3}$ is substituted by $\underline{a} = e^{j\pi/n}$. In short $\underline{\alpha} = e^{j2\pi/3}$, or $\underline{\alpha} = e^{j2\pi/n}$ in a more general form, has a two-pole symmetry, while the fundamental reference frame has its components distributed over π electric radians to allow the description of MPMs in a generalized form. With the complex operator $\underline{a} = e^{j\pi/n}$ it is possible to define a modified method of symmetrical components calculation for the fundamental reference frame, where its components have a one-pole symmetry. After some math, described in [29], one can derive the generalized Clarke transformation, which in its amplitude-invariant version, takes the form:

$$\mathbf{T}_{123\to\alpha\beta 0} = \left(\mathbf{T}_{\alpha\beta 0\to 123}\right)^{-1} = \frac{2}{n} \cdot \left(\mathbf{T}_{\alpha\beta 0\to 123}\right)^{T} \tag{2.6}$$

where again $\delta = \pi/n$, and

$$\mathbf{T}_{\alpha\beta0\rightarrow123} = \begin{bmatrix} 1 & 0 & 1 & 0 & 1 & \cdots & \frac{1}{\sqrt{2}} \\ \cos\delta & \sin\delta & \cos 3\delta & \sin 3\delta & \cos 5\delta & \cdots & -\frac{1}{\sqrt{2}} \\ \cos 2\delta & \sin 2\delta & \cos 6\delta & \sin 6\delta & \cos 10\delta & \cdots & \frac{1}{\sqrt{2}} \\ \cos 3\delta & \sin 3\delta & \cos 9\delta & \sin 9\delta & \cos 15\delta & \cdots & -\frac{1}{\sqrt{2}} \\ \vdots & \vdots & \vdots & \vdots & \vdots & \ddots & \vdots \\ \cos(n-2)\delta & \sin(n-2)\delta & \cos(n-6)\delta & \sin(n-6)\delta & \cos(n-10)\delta & \cdots & -\frac{1}{\sqrt{2}} \\ \cos(n-1)\delta & \sin(n-1)\delta & \cos(n-3)\delta & \sin(n-3)\delta & \cos(n-5)\delta & \cdots & \frac{1}{\sqrt{2}} \end{bmatrix} \tag{2.7}$$

where the last column is present only when the number of phases n is odd. The transformation matrices that go directly from the practical reference frame to the "$\alpha\beta0$" reference frame, and viceversa, then are:

$$\mathbf{T}_{abc\rightarrow\alpha\beta0} = \mathbf{T}_{123\rightarrow\alpha\beta0}\mathbf{T}_{abc\rightarrow123}, \tag{2.8}$$

$$\mathbf{T}_{\alpha\beta0\rightarrow123} = \mathbf{T}_{123\rightarrow abc}\mathbf{T}_{\alpha\beta0\rightarrow123}. \tag{2.9}$$

Note that (2.8) for the three-phase case becomes:

$$\mathbf{T}_{123\rightarrow\alpha\beta0} = \frac{2}{3}\begin{bmatrix} 1 & -\frac{1}{2} & -\frac{1}{2} \\ 0 & \frac{\sqrt{3}}{2} & -\frac{\sqrt{3}}{2} \\ \frac{1}{2} & \frac{1}{2} & \frac{1}{2} \end{bmatrix} \tag{2.10}$$

which is the conventional amplitude-invariant Clarke transformation.

2.2.3 *Harmonic mapping*

When we apply (2.8) to the general vector $\mathbf{x}_{abc}$ we get the vector $\mathbf{x}_{\alpha\beta0}$, that looks like:

$$\mathbf{x}_{\alpha\beta0} = \mathbf{T}_{123\rightarrow\alpha\beta0}\mathbf{x}_{abc}, \tag{2.11}$$

$$\mathbf{x}_{\alpha\beta0} = \begin{bmatrix} x_{\alpha1} \\ x_{\beta1} \\ x_{\alpha3} \\ x_{\beta3} \\ \vdots \\ x_{\alpha(n-1)} \\ x_{\beta(n-1)} \\ x_0 \end{bmatrix}. \tag{2.12}$$

Its elements are real values. The terms $x_{\alpha k}$ and $x_{\beta k}$ represent the coordinates of a k-th geometric plane, which can be demonstrated to be orthogonal to the other planes, [29]. We will refer to this orthogonal planes also as vector subspaces, as the VSD theory suggests. The union of the orthogonal planes forms $\mathbf{x}_{\alpha\beta 0}$. The last component x_0 is present only for system with odd n, represent an axis orthogonal to all the other planes, and it is what we are used to call the zero-sequence component. In systems with an even number of phases, $\mathbf{x}_{\alpha\beta 0}$ does not contain an explicit form of the zero-sequence component, but it is possible that the machine configuration would transform one of the harmonics into a zero-sequence component. For example, in the already mentioned YY30 machine, when the two star points are isolated, the third harmonic cannot produce currents and thus $x_{\alpha 3}$ and $x_{\beta 3}$ act as a zero sequence component. This is why in literature, for six-phase machines, is common to see a different nomenclature for the $\mathbf{x}_{\alpha\beta 0}$ components and a reference to the $\alpha\beta$, 0^+0^- and xy orthogonal planes. The reason to use the $\alpha_k\beta_k$ nomenclature is that the first *odd* k-th harmonics, up to n, are mapped into the $\alpha_k\beta_k$ subspace. By the way those are not the only harmonics mapped into the subspace: for example in the three-phase case, except homopolar components, all the other harmonics are mapped into the only available $\alpha\beta$ plane. How higher order harmonics are mapped into the various planes depends on many factors such as the winding configuration (symmetric or asymmetric) and the neutral point configuration (one single neutral point ore many isolated neutral points). In addition some are mapped as a direct sequence and some others as indirect sequence. In [22] and [39] a graphic method to determine the higher order harmonics mapping is presented, for different symmetric and asymmetric winding arrangements respectively.

2.2.4 *The generalized Park transformation*

The Park transformation matrix for multi-phase machines is a natural extension of the three-phase version, where each of the couples $(x_{\alpha k}, x_{\beta k})$, representative of the k-th harmonic component for odd k, is transformed into a separate rotating reference frame. Its generalized form is:

$$\mathbf{T}_{\alpha\beta 0\to dq0} = \begin{bmatrix} \cos\left(\theta_{r,f}\right) & \sin\left(\theta_{r,f}\right) & 0 & 0 & 0 & 0 & \cdots & 0 \\ -\sin\left(\theta_{r,f}\right) & \cos\left(\theta_{r,f}\right) & 0 & 0 & 0 & 0 & \cdots & 0 \\ 0 & 0 & \cos\left(3\theta_{r,f}\right) & \sin\left(3\theta_{r,f}\right) & 0 & 0 & \cdots & 0 \\ 0 & 0 & -\sin\left(3\theta_{r,f}\right) & \cos\left(3\theta_{r,f}\right) & 0 & 0 & \cdots & 0 \\ 0 & 0 & 0 & 0 & \cos\left(5\theta_{r,f}\right) & \sin\left(5\theta_{r,f}\right) & \cdots & 0 \\ 0 & 0 & 0 & 0 & -\sin\left(5\theta_{r,f}\right) & \cos\left(5\theta_{r,f}\right) & \cdots & 0 \\ \vdots & \vdots & \vdots & \vdots & \vdots & \vdots & \ddots & \vdots \\ 0 & 0 & 0 & 0 & 0 & 0 & \cdots & 1 \end{bmatrix}. \tag{2.13}$$

Each $(x_{\alpha k}, x_{\beta k})$ couple is transformed into a reference frame rotating with the angle $k\theta_{r,f}$, where $\theta_{r,f}$ is the electric angle of the rotor flux with respect to the phase a of the machine. Again the last column, and the last row, of (2.13) are present only if n is odd, and the zero-sequence component is maintained by the presence of the value 1 in the diagonal.

2.3 MODELLING OF A MULTIPHASE INDUCTION MACHINE

In [28] a complex space-vector approach is exploited, leading to a model which is simplified with respect to the one obtained with a full matrix approach. The approach was first proposed in [24], but it was focused only on three-phase machines. In [28] the work is extended to MPMs. Both implicitly assume assume a machine having only one pair of poles, but the extention to multipole structures is quite straightforward. The following assumptions are made:

- negligible magnetic saturation;
- uniform air-gap;
- negligible inter-bar current;

The amplitude-invariant k-th order complex space-vector is defined in [28] as follows:

$$\underline{\mathbf{x}}_k = \frac{2}{n} \sum_{i=1}^{n} \underline{a}^{k(i-1)} x_i \tag{2.14}$$

where $\underline{a} = e^{j\pi/n}$, as already introduced in 2.2.2, and x_i is the i-th component of the general vector in the fundamental reference frame $\mathbf{x}_{123}$. The real and imaginary part of $\underline{\mathbf{x}}_k$ are respectively $x_{\alpha k}$ and $x_{\beta k}$. In presence of homopolar components, a homopolar complex space-vector can be defined too:

$$\underline{\mathbf{x}}_0 = \frac{2}{n} \frac{\sqrt{2}}{2} \sum_{i=1}^{n} (-1)^{(i-1)} x_i. \tag{2.15}$$

Again, note that applying Eq. (2.14) to a three-phase system gives the familiar space-vector we are used to, in fact it becomes:

$$\underline{\mathbf{x}}_1 = \frac{2}{3}(x_1 + \underline{a}x_2 + \underline{a}^2 x_3) = \cdots = \frac{2}{3}(x_a + \underline{\alpha}x_b + \underline{\alpha}^2 x_c) \tag{2.16}$$

where $\underline{\alpha} = e^{j2\pi/3}$.

2.3.1 *The stator model*

The voltage balance equation for the stator windings of an induction machine, in complex space-vector notation for the k-th harmonic is:

$$\underline{\mathbf{v}}_{s,k} = R_s \underline{\mathbf{i}}_{s,k} + \frac{d\underline{\boldsymbol{\lambda}}_{s,k}}{dt} + \frac{d\underline{\boldsymbol{\lambda}}_{s,l}}{dt} \tag{2.17}$$

where $\underline{\mathbf{v}}_{s,k}$, $\underline{\mathbf{i}}_{s,k}$, $\underline{\boldsymbol{\lambda}}_{s,k}$, $\underline{\boldsymbol{\lambda}}_{s,l}$ are the stator k-th harmonic voltage, current, flux linkage, flux leakage complex space-vector respectively, and R_s is the stator resistance. The stator flux linkage space-vector $\underline{\boldsymbol{\lambda}}_{s,k}$ can be divided in the contribution of the stator currents $\underline{\boldsymbol{\lambda}}_{ss,k}$ and the contribution of the rotor currents through the mutual coupling $\underline{\boldsymbol{\lambda}}_{sr,k}$. The two components will be treated separately below.

2.3.1.1 *Stator flux linkage due to stator currents*

The stator flux linkage space-vector for the k-th harmonic can be written as:

$$\underline{\boldsymbol{\lambda}}_{ss,k} = L_{ss,k} \underline{\mathbf{i}}_{s,k}. \tag{2.18}$$

It can be obtained applying the definition of complex space-vector as given in (2.14) to the equation in the fundamental reference frame:

$$\boldsymbol{\lambda}_{ss,123} = \mathbf{L}_{ss,123} \mathbf{i}_{s,123} \tag{2.19}$$

where $\mathbf{L}_{ss,123}$ is the n-by-n stator inductance matrix. Its elements can be obtained following a geometric approach that make use of the winding functions. The theoretical foundation of this method is described in depth in [20] (which the Reader is redirected to for a deeper investigation). One of the most important result is that the inductance between two generic phases i and j, when the the air gap is considered constant, is calculated as follows:

$$L_{i,j} = \frac{\mu_0 r l}{g} \int_0^{2\pi} N_i(\phi) N_j(\phi) d\phi, \qquad i, j = 1, 2, \ldots, n \tag{2.20}$$

where μ_0 is the magnetic permeability of air, r is the radius of the inner shell of the stator, g is the air gap value (which could be substituted by the effective air gap g_e), and l is the axial length of the rotor. $N_i(\phi)$ and $N_j(\phi)$ are the winding functions of the i-th and j-th phase. The ideal profile for the distributed winding case is shown in Fig. 2.7 and can be mathematically expressed as:

$$N(\phi) = \frac{N_t}{2p} \cos(\phi) \tag{2.21}$$

where N_t is the number of turns and $2p$ is the number of poles of the machine. In case of distributed windings the ideal profile would be a square wave, but to ease the calculation of the inductances it is beneficial to express it with the equivalent Fourier series, truncated for example to the third therm. In this case we get:

$$N(\phi)_{Fourier} = \frac{4}{\pi}\frac{N_t}{2p}\left(\cos(\phi) - \frac{1}{3}cos(3\phi) + \frac{1}{5}cos(5\phi)\right). \tag{2.22}$$

The ideal and the Fourier series profiles for the full-pitch concentrated windings are shown in Fig. 2.8.

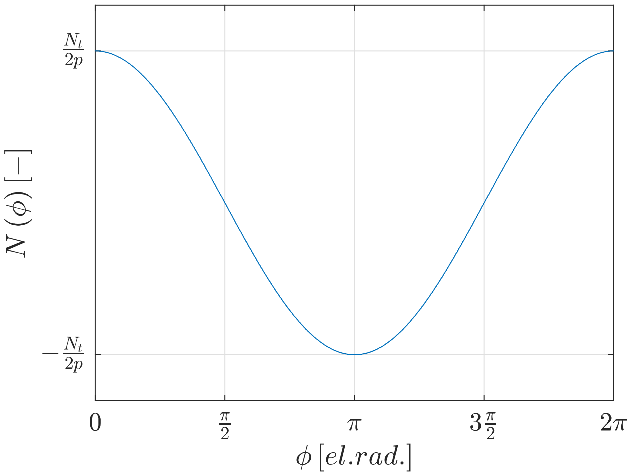

Figure 2.7: Ideal winding function for the distributed winding case.

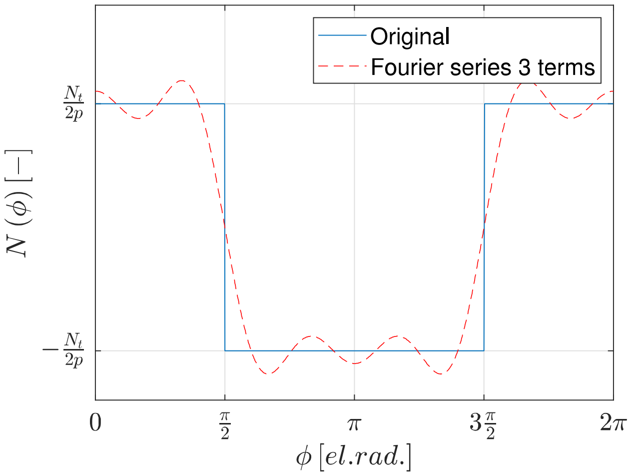

Figure 2.8: Ideal winding function for the concentrated winding case, and its Fourier series expansion with three terms.

What we have shown are the profiles of the winding functions, when we calculate the inductances we have to take into account that two adjacent phase have the winding function shifted by $\delta = \frac{\pi}{n}$. Once obtained $\mathbf{L}_{ss,123}$, definition (2.14) can be applied to eq. (2.19) in order to get (2.18). The parameters $L_{ss,k}$ that you get in case of five or six-phase machine, distributed or full-pitch concentrated windings are shown in Table 2.1. It is to note that if the generalized and Clarke and Park transformations are applied to the matrix $\mathbf{L}_{ss,123}$ you get a matrix $\mathbf{L}_{ss,dq0}$ in which only diagonal terms are non-zeroes, and they corresponds to the $L_{ss,k}$ terms (first two diagonal terms corresponds to $L_{ss,1}$, next two to $L_{ss,3}$, and so on). If the matrix $\mathbf{L}_{ss,dq0}$ presents some off-diagonal terms this mean that the various vector subspaces are not independent but somehow coupled, this can happen for example in synchronous machine with anisotropic rotor, for which Eq. (2.20) has a different formulation because the air-gap function is not constant anymore. The same can be true for any machine which present some eccentricity in the rotor. This cases will be not treated here, but a formulation of the winding functions for a squirrel-cage induction machine with a non-uniform air gap can be found in [9].

2.3.1.2 *Stator flux leakage*

In case of linear magnetic circuit, phases geometrically balanced and leakage flux independent on the rotor position, [33] states that the leakage inductance matrix in the fundamental reference frame $\mathbf{L}_{l,123}$ exhibits a Toeplitz structure because the leakage inductance linking two generic phases i and $i+j$ depends only on their mutual phase displacement $j\delta$. The leakage flux can be expressed as:

$$\boldsymbol{\lambda}_{l,123} = \mathbf{L}_{l,123}\mathbf{i}_{s,123} \tag{2.23}$$

and by applying (2.14) to it, one can get:

$$\underline{\boldsymbol{\lambda}}_{l,k} = L_{l,k}\underline{\mathbf{i}}_{l,k}. \tag{2.24}$$

in which the leakage inductance for the k-th vector subspace can be expressed as:

$$L_{sl,k} = l_0 + 2\sum_{j=1}^{\chi} l_j \cos\left(kj\frac{\pi}{n}\right), \qquad \text{with} \quad \chi = trunc\left(\frac{n-1}{2}\right) \tag{2.25}$$

where l_j is the mutual inductance between the i-th and the $(i+j)$-th stator winding. Again, results for five and six-phase machine, distributed and full-pitch concentrated windings case are shown in Table 2.1.

2.3.1.3 *Stator flux linkage due to the rotor currents*

For the analysis of the flux linkage contribution related to the mutual coupling between the stator and the rotor circuits it is necessary to introduce a model for the squirrel cage rotor with N_b number of bars. The analysis performed in [24] and [28] assumes the rotor cage as a circuit with N_b identical and equally spaced loops, as shown in Fig. 2.9. In the fundamental reference frame the stator flux linkage due to the

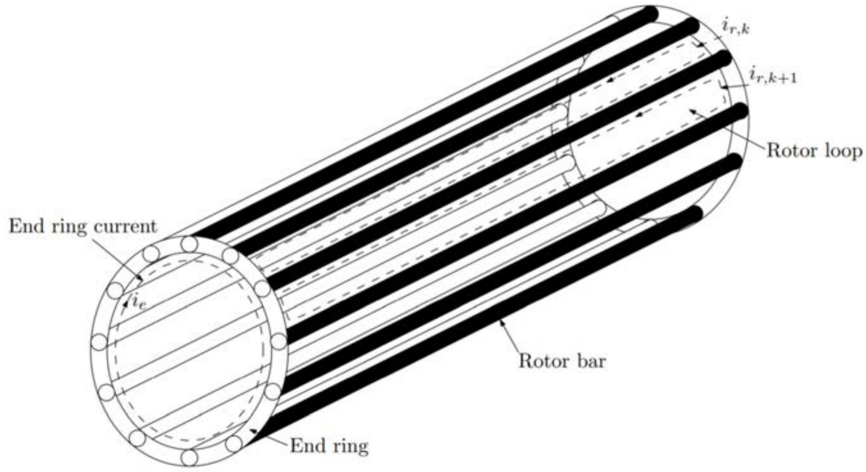

Figure 2.9: Schematic of the squirrel cage rotor and definition of the elementary loops for mutual inductance calculation, [24].

rotor currents can be expressed with:

$$\boldsymbol{\lambda}_{sr,123} = \mathbf{L}_{sr,123}\mathbf{i}_{r,123} \tag{2.26}$$

where $\mathbf{i}_{r,123}$ is a vector of size n_b with the rotor loops currents, and $\mathbf{L}_{sr,123}$ is a n-by-n_b matrix, being $n_b = N_b$ for a two-pole machine, and $n_b = \frac{N_b}{p}$ number of rotor bars per pole-pair in its extension to multi-pole machines. In this regard, [24] states that, given a symmetrical structure of the rotor, the model of the rotor cage as identical magnetically coupled circuits can be used also with non-integral number of bars per pole-pair. In a similar way to the analysis done in 2.3.1.1, the mutual inductances can be calculated provided that the winding functions of the stator phases and of the rotor loops are known. Nevertheless note that this time rotor loop winding functions are dependent on the rotor position θ_{me}, since their relative position to the stator windings depends on the rotor position itself. Thus, the mutual inductances $L_{sr,ij}$ between the i-th stator phase and the j-th rotor loop, that compose the $\mathbf{L}_{sr,123}$ matrix, are also position-dependent, and they can be calculated with:

$$L_{sr,ij}\left(\theta_{me}\right) = \frac{\mu_0 r l}{g}\int_0^{2\pi} N_i(\phi) N_j\left(\phi,\theta_{me}\right) d\phi, \qquad i,j = 1,2,\ldots,n. \tag{2.27}$$

The normalized winding function for the j-th rotor loop is shown in Fig. 2.10. The winding functions for all the other loops are the same but phase-shifted by an angle defined by the position of each loop with respect to an initial reference angle θ_r. We can write:

$$\theta_j = \theta_r + (j-1)\alpha_r \tag{2.28}$$

$$\theta_{j+1} = \theta_j + \alpha_r \tag{2.29}$$

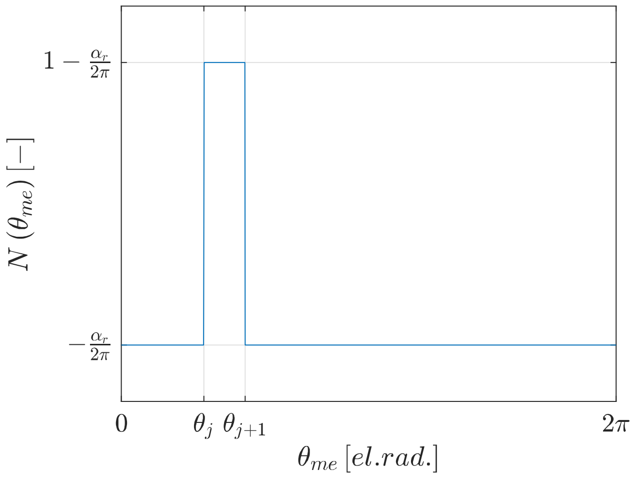

Figure 2.10: Ideal winding function for the j-th rotor bar in a squirrel-cage induction machine rotor, for n_b=12.

where

$$\alpha_r = \frac{2\pi}{n_b} \tag{2.30}$$

is the angle between two adjacent rotor bars. After some mathematical elaborations, involving the use of the the Euler formula to express cosine functions in terms of complex exponentials and the use of the definition of complex space-vector, as well shown both in [24] and [28], one can eventually get to the following space-vector relations:

$$\underline{\boldsymbol{\lambda}}_{sr,1} = \frac{n_b}{2} L_m^d e^{j\left(\theta_r + \dfrac{\alpha_r}{2}\right)} \underline{\boldsymbol{i}}_{r,1} \tag{2.31}$$

for the distributed winding case, where we have interaction only in the fisrt/fundamental vector subspace, and

$$\underline{\boldsymbol{\lambda}}_{sr,k} = \frac{n_b}{2} L_{m,k}^c e^{jk\left(\theta_r + \dfrac{\alpha_r}{2} + \dfrac{\gamma_k}{k}\right)} \underline{\boldsymbol{i}}_{r,k} \tag{2.32}$$

for the k-th vector subspace of the full-pitch concentrated winding case. Parameters L_m^d and $L_{m,k}^c$ are expressed as:

$$L_m^d = \frac{\mu_0 r l N_t}{g} \sin\left(\frac{\alpha_r}{2}\right) \tag{2.33}$$

$$L_{m,k}^c = \frac{\mu_0 r l N_t \alpha_r}{g} \left|\frac{\sin\left(k\frac{\alpha_r}{2}\right)}{k\frac{\alpha_r}{2}}\right| \left|\frac{\sin\left(k\frac{\pi}{2}\right)}{k\frac{\pi}{2}}\right| \tag{2.34}$$

Table 2.1: Stator self inductance, stator leakage inductance, stator-rotor mutual inductance, for each vector subspace, for five-phase and six-phase machines, distributed or full-pitch concentrated windings, analytically obtained as described in [28].

	n	k	$L_{ss,k}$	$L_{sl,k}$	$\underline{L}_{sr,k}$
Distributed windings	5	1	$\frac{5}{2}L_{ss}$	$l_0+\frac{l_1}{2}\left(1+\sqrt{5}\right)-\frac{l_2}{2}\left(1-\sqrt{5}\right)$	$\frac{n_b}{2}L_m^d e^{j\left(\theta_{me}+\frac{\alpha_r}{2}\right)}$
		3	0	$l_0+\frac{l_1}{2}\left(1-\sqrt{5}\right)-\frac{l_2}{2}\left(1+\sqrt{5}\right)$	0
	6	1	$3L_{ss}$	$l_0+l_2+\sqrt{3}l_1$	$\frac{n_b}{2}L_m^d e^{j\left(\theta_{me}+\frac{\alpha_r}{2}\right)}$
		3	0	l_0-2l_2	0
		5	0	$l_0+l_2-\sqrt{3}l_2$	0
Full-pitch concentrated windings	5	1	$\frac{4}{5}\left(3+\sqrt{5}\right)L_{ss}$	$l_0+\frac{l_1}{2}\left(1+\sqrt{5}\right)-\frac{l_2}{2}\left(1-\sqrt{5}\right)$	$\frac{n_b}{2}L_{m,1}^c e^{j\left(\theta_{me}+\frac{\alpha_r}{2}\right)}$
		3	$\frac{4}{5}\left(3-\sqrt{5}\right)L_{ss}$	$l_0+\frac{l_1}{2}\left(1-\sqrt{5}\right)-\frac{l_2}{2}\left(1+\sqrt{5}\right)$	$\frac{n_b}{2}L_{m,1}^c e^{j3\left(\theta_{me}+\frac{\alpha_r}{2}+\frac{\pi}{3}\right)}$
	6	1	$\frac{4}{3}\left(2+\sqrt{3}\right)L_{ss}$	$l_0+l_2+\sqrt{3}l_1$	$\frac{n_b}{2}L_{m,1}^c e^{j\left(\theta_{me}+\frac{\alpha_r}{2}\right)}$
		3	$\frac{2}{5}L_{ss}$	l_0-2l_2	$\frac{n_b}{2}L_{m,3}^c e^{j3\left(\theta_{me}+\frac{\alpha_r}{2}+\frac{\pi}{3}\right)}$
		5	$\frac{4}{3}\left(2-\sqrt{3}\right)L_{ss}$	$l_0+l_2-\sqrt{3}l_1$	$\frac{n_b}{2}L_{m,5}^c e^{j5\left(\theta_{me}+\frac{\alpha_r}{2}\right)}$

$$L_{ss}=\frac{\mu_0 r l \pi N_t^2}{2g}$$

l_j is the mutual inductance between the i-th and the $(i+j)$-th stator winding

$$L_m^d=\frac{\mu_0 r l N_t}{g}\sin\left(\frac{\alpha_r}{2}\right)$$

$$L_{m,k}^c=\frac{\mu_0 r l N_t \alpha_r}{g}\left|\frac{\sin\left(k\frac{\alpha_r}{2}\right)}{k\frac{\alpha_r}{2}}\right|\left|\frac{\sin\left(k\frac{\pi}{2}\right)}{k\frac{\pi}{2}}\right|$$

while γ_k has the following expression:

$$\gamma_k=k\frac{\pi}{2}+\angle\left[e^{-jk\frac{\pi}{2}}\sin\left(\frac{\pi}{2}\right)\right]=\begin{cases}0 & \text{for}k=1,5,9,\ldots\\ \pi & \text{for}k=3,7,11,\ldots\end{cases}\tag{2.35}$$

If equations (2.31) and (2.32) are written in the general form

$$\underline{\boldsymbol{\lambda}}_{sr,k}=\underline{L}_{sr,k}\underline{\boldsymbol{i}}_{r,k}\tag{2.36}$$

then the corresponding expressions of $\underline{L}_{sr,k}$ for five and six-phase machines, distributed and full-pitch concentrated windings case, are reported in Table 2.1, where the reference angle on the rotor θ_r has been replaced by θ_{me}, being it integral with rotor.

2.3.2 *The rotor model*

We continue to consider the same rotor model introduced in 2.3.1.3. If each rotor bar and segment of end ring is substituted by an equivalent circuit representing its resistive and inductive nature we get an equivalent circuit that looks like the one shown in Fig. 2.11. Carrying out an anlysis based on mesh currents as independent variables, there are $n_b + 1$ independent meshes defined by n_b rotor loops (plus one formed by any one of the end rings that we will not consider because in absence of an axial flux component the circumferential current in the end ring is identically zero). The equation for the j-th rotor loop is:

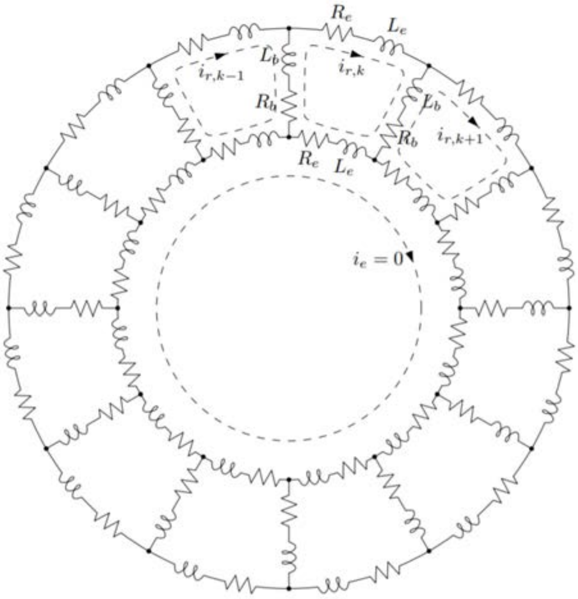

Figure 2.11: Model of the squirrel cage rotor with 12 rotor bars, [24].

$$0 = 2(R_b + R_e)i_{r,j} - R_b i_{r,j-1} - R_b i_{r,j+1} + \frac{d\lambda_{r,j}}{dt} \tag{2.37}$$

where R_b is the bar resistance, R_e is the end-ring segment resistance, $\lambda_{r,j}$ is the total flux linked by the j-th loop, and $i_{r,j}$ is the loop current. It is valid for every loop, therefore, the rotor voltage equation in matrix form assumes the form:

$$\begin{bmatrix} 0 \\ 0 \\ \vdots \\ 0 \end{bmatrix} = \begin{bmatrix} R_o & -R_b & \cdots & -R_b \\ -R_b & R_o & \cdots & 0 \\ \vdots & \vdots & \ddots & \vdots \\ -R_b & 0 & \cdots & R_o \end{bmatrix} \begin{bmatrix} i_{r,1} \\ i_{r,2} \\ \vdots \\ i_{r,n_b} \end{bmatrix} + \frac{d}{dt} \begin{bmatrix} \lambda_{r,1} \\ \lambda_{r,2} \\ \vdots \\ \lambda_{r,n_b} \end{bmatrix} \tag{2.38}$$

where $R_o = 2(R_b + R_e)$. As for the stator, a complex space-vector for a generic rotor quantity x_r can be defined:

$$\underline{\mathbf{x}}_{r,k} = \frac{2}{n_b} \sum_{i=1}^{n_b} \underline{b}^{k(i-1)} x_{r,i} \tag{2.39}$$

where $\underline{b} = e^{j\alpha_r}$. Note that this is equivalent of applying to a vector with the rotor loop quantities $\mathbf{x}_{r,123} = [x_{r,1}\ x_{r,2}\ \dots\ x_{r,n_b}]^T$ the generalized Clarke transformation as defined in Eq (2.6), but with α_r instead of δ and n_b instead of n (we could refer to it as $T^r_{123\rightarrow\alpha\beta0}$ of size $n_b \times n_b$). In fact doing so, you would get a vector in which the two first components correspond to the real and imaginary part of the first complex space-vector, and so on. If the new complex space-vector definition of Eq. (2.39) is applied to the matrix equation (2.38), for the k-th vector subspace we obtain:

$$\underline{0} = R_r \underline{\mathbf{i}}_{r,k} + \frac{d\underline{\boldsymbol{\lambda}}_{r,k}}{dt} \tag{2.40}$$

where R_r is the rotor resistance in the subspace and its final expression can be shown to be qual to:

$$R_r = 2R_e + 2R_b(1 - \cos(\alpha_r)). \tag{2.41}$$

It is obtained after multiplying each row of the first term in (2.38) by $1, \underline{b}, \dots, \underline{b}^{n_b-1}$, adding the rows, and simplifying, [24]. The rotor flux linkage space-vector $\underline{\boldsymbol{\lambda}}_{r,k}$ can be divided in the contribution of the rotor currents $\underline{\boldsymbol{\lambda}}_{rr,k}$ and the contribution of the stator currents through the mutual coupling $\underline{\boldsymbol{\lambda}}_{rs,k}$. The two components will be treated separately below.

2.3.2.1 *Rotor flux linkage due to the stator currents*

In the fundamental reference frame the rotor flux linkage due to the stator currents can be expressed with:

$$\boldsymbol{\lambda}_{rs,123} = \mathbf{L}_{rs,123} \mathbf{i}_{s,123} \tag{2.42}$$

where $\mathbf{L}_{rs,123}$ is an n_b-by-n matrix which is the transpose of $\mathbf{L}_{sr,123}$ seen in 2.3.1.3, being $L_{rs,ij} = L_{sr,ij}$ based on energy consideration. Following a similar mathematical elaboration as in 2.3.1.3, one can eventually get to the following space-vector relations:

$$\underline{\boldsymbol{\lambda}}_{rs,1} = \frac{n_b}{2} L_m^d e^{-j\left(\theta_r + \frac{\alpha_r}{2}\right)} \underline{\boldsymbol{i}}_{s,1} \tag{2.43}$$

for the distributed winding case, where we have interaction only in the fisrt/fundamental vector subspace, and

$$\underline{\boldsymbol{\lambda}}_{rs,k} = \frac{n_b}{2} L^c_{m,k} e^{-jk\left(\theta_r + \frac{\alpha_r}{2} + \frac{\gamma_k}{k}\right)} \underline{\boldsymbol{i}}_{s,k} \tag{2.44}$$

for the k-th vector subspace of the full-pitch concentrated winding case. If equations (2.43) and (2.44) are written in the general form

$$\underline{\boldsymbol{\lambda}}_{rs,k} = \underline{L}_{rs,k} \underline{\boldsymbol{i}}_{s,k} \tag{2.45}$$

then the correspondant expressions of $\underline{L}_{rs,k}$ for five and six-phase machines, distributed and full-pitch concentrated windings case, are reported in Table 2.2.

2.3.2.2 *Rotor flux linkage due to the rotor currents*

Using always the same model of the rotor, the total flux linked by j-th rotor loop and due only to rotor currents is expressed as:

$$\begin{aligned}\lambda_{rr,j} = L_{rr,j1} i_{r,1} + L_{rr,j2} i_{r,2} + \cdots + L_{rr,jn_b} i_{r,n_b} + \\ + 2(L_e + L_b) i_{r,j} - L_b (i_{r,j-1} + i_{r,j+1})\end{aligned} \tag{2.46}$$

where $L_{rr,j1}$ is the mutual inductance between the j-th and the i-th rotor loops, L_e is the inductance of the end-ring segment, and L_b is the inductance of one rotor bar. Given the structural symmetry of the rotor,the same equation can be written for all the other loops, and in matrix form it becomes:

$$\begin{bmatrix} \lambda_{rr,1} \\ \lambda_{rr,2} \\ \vdots \\ \lambda_{rr,n_b} \end{bmatrix} = \begin{bmatrix} L_{rr,11} + L_{rr,o} & L_{rr,12} - L_b & \cdots & L_{rr,1n_b} - L_b \\ L_{rr,21} - L_b & L_{rr,22} + L_{rr,o} & \cdots & L_{rr,2n_b} \\ \vdots & \vdots & \ddots & \vdots \\ L_{rr,n_b1} - L_b & L_{rr,n_b2} & \cdots & L_{rr,n_bn_b} + L_{rr,o} \end{bmatrix} \begin{bmatrix} i_{r,1} \\ i_{r,2} \\ \vdots \\ i_{r,n_b} \end{bmatrix} + \frac{d}{dt} \begin{bmatrix} \lambda_{r,1} \\ \lambda_{r,2} \\ \vdots \\ \lambda_{r,n_b} \end{bmatrix} \tag{2.47}$$

where $L_{rr,o} = 2(L_e + L_b)$. The self and mutual inductances of the rotor loops can be obtained again with the winding functions theory:

$$L_{rr,ij} = \frac{\mu_0 l r}{g} \int_0^{2\pi} N_i(\phi) N_j(\phi) d\phi = \begin{cases} \dfrac{\mu_0 l r}{g} \alpha_r \left(1 - \dfrac{\alpha_r}{2\pi}\right) & i = j \\ \dfrac{\mu_0 l r}{g} \alpha_r \left(-\dfrac{\alpha_r^2}{2\pi}\right) & i \neq j \end{cases} \tag{2.48}$$

Note that these inductances are independent on the mutual loop position. Substituting (2.48) into (2.47), then multiplying the rows of (2.47)

Table 2.2: Rotor self inductance, rotor-stator mutual inductance, for each vector subspace, for five-phase and six-phase machines, distributed or full-pitch concentrated windings, analytically obtained as described in [28].

	n	k	$L_{rr,k}$	$\underline{L}_{rs,k}$
Distributed windings	5	1	L_{rr}	$\frac{5}{2}L_m^d e^{-j\left(\theta_{me}+\frac{\alpha_r}{2}\right)}$
	6	1	L_{rr}	$3L_m^d e^{-j\left(\theta_{me}+\frac{\alpha_r}{2}\right)}$
Full-pitch concentrated windings	5	1	L_{rr}	$\frac{5}{2}L_{m,1}^c e^{-j\left(\theta_{me}+\frac{\alpha_r}{2}\right)}$
		3	L_{rr}	$\frac{5}{2}L_{m,3}^c e^{-j3\left(\theta_{me}+\frac{\alpha_r}{2}+\frac{\pi}{3}\right)}$
	6	1	L_{rr}	$3L_{m,1}^c e^{-j\left(\theta_{me}+\frac{\alpha_r}{2}\right)}$
		3	L_{rr}	$3L_{m,3}^c e^{-j3\left(\theta_{me}+\frac{\alpha_r}{2}+\frac{\pi}{3}\right)}$
		5	L_{rr}	$3L_{m,5}^c e^{-j5\left(\theta_{me}+\frac{\alpha_r}{2}\right)}$

$$L_{rr} = \left(2L_b\left(1 - cos(\alpha_r)\right) + 2L_e + \frac{\mu_0 lr}{g}\alpha_r\right)$$

$$L_m^d = \frac{\mu_0 rlN_t}{g}\sin\left(\frac{\alpha_r}{2}\right)$$

$$L_{m,h}^c = \frac{\mu_0 rlN_t\alpha_r}{g}\left|\frac{\sin\left(h\frac{\alpha_r}{2}\right)}{h\frac{\alpha_r}{2}}\right|\left|\frac{\sin\left(h\frac{\pi}{2}\right)}{h\frac{\pi}{2}}\right|$$

by $1, \underline{b}, \ldots, \underline{b}^{n_b-1}$, then adding the rows and finally simplifiying yelds to the following complex space-vector equation:

$$\underline{\boldsymbol{\lambda}}_{rr,1} = L_{rr}\underline{\mathbf{i}}_{r,1} \tag{2.49}$$

where

$$L_{rr} = \left(2L_b\left(1 - cos(\alpha_r)\right) + 2L_e + \frac{\mu_0 lr}{g}\alpha_r\right). \tag{2.50}$$

Since L_{rr} is independent on the relative position of the rotor loops it can be shown that the same expression is found for the k-th harmonic complex space-vector:

$$\underline{\boldsymbol{\lambda}}_{rr,k} = L_{rr}\underline{\mathbf{i}}_{r,k}. \tag{2.51}$$

This result is also reported in Table 2.2.

2.3.3 *The complex vector equivalent circuit*

So far we have found the following set of equations, for each k-th vector subspace:

$$\underline{\mathbf{v}}_{s,k} = R_s \underline{\mathbf{i}}_{s,k} + \frac{d\underline{\boldsymbol{\lambda}}_{s,k}}{dt} \tag{2.52}$$

$$\underline{\boldsymbol{\lambda}}_{ss,k} = L_{ss,k} \underline{\mathbf{i}}_{s,k} \tag{2.53}$$

$$\underline{\boldsymbol{\lambda}}_{sr,k} = \underline{L}_{sr,k} \underline{\boldsymbol{i}}_{r,k} \tag{2.54}$$

$$\underline{0} = R_r \underline{\mathbf{i}}_{r,k} + \frac{d\underline{\boldsymbol{\lambda}}_{r,k}}{dt} \tag{2.55}$$

$$\underline{\boldsymbol{\lambda}}_{rs,k} = \underline{L}_{rs,k} \underline{\boldsymbol{i}}_{s,k} \tag{2.56}$$

$$\underline{\boldsymbol{\lambda}}_{rr,k} = L_{rr} \underline{\mathbf{i}}_{r,k} \tag{2.57}$$

where the leakage component of the stator flux has been neglected for ease of analysis. By putting together the components of the stator and the rotor flux respectively, we can write:

$$\underline{\boldsymbol{\lambda}}_{s,k} = L_{ss,k} \underline{\mathbf{i}}_{s,k} + \frac{n_b}{2} L_{m,k} e^{jk\left(\theta'_k\right)} \underline{\mathbf{i}}_{r,k} \tag{2.58}$$

$$\underline{\boldsymbol{\lambda}}_{r,k} = \frac{n}{2} L_{m,k} e^{-jk\left(\theta'_k\right)} \underline{\mathbf{i}}_{s,k} + L_{rr} \underline{\mathbf{i}}_{r,k} \tag{2.59}$$

where $L_{m,k}$ represent $L^d_{m,1} = L^d_m$ for the distributed winding case, or $L^c_{m,k}$ for the full-pitch concentrated winding case, and

$$\theta'_k = \left(\theta_{me} + \frac{\alpha_r}{2} + \frac{\gamma_k}{k}\right) \tag{2.60}$$

where the refernce angle θ_r has been replaced by θ_{me}, being it integral with the rotor. Note that for how the approach has been set-up, the equations we have obtained so far, for the stator are referred to k independet $\alpha_k\beta_k$ reference frames which are stationary, while for the rotor they are referred to k independent d_kq_k reference frames which rotate at different angular speed $k\omega_{me}$ defined by the angle $k\theta'_k$ with respect to the stationary one. It is convenient to refer the equations to k common, generic, reference frames $d^x_kq^x_k$, rotating at angular speed $k\omega_x$ defined by the angle $k\theta_x$ with respect to the stationary one. The different reference frames are shown in Fig. 2.12. The generic complex space-vector in the k-th vector subspace $\underline{\mathbf{g}}_k$ of amplitude g_k can be expressed in the various reference frame as follows:

$$\begin{aligned} \underline{\mathbf{g}}_k &= g_k e^{j\nu^s_k} \qquad \text{in} \quad \alpha_k\beta_k \\ \underline{\mathbf{g}}_k &= g_k e^{j\nu^r_k} \qquad \text{in} \quad d_kq_k \\ \underline{\mathbf{g}}_k &= g_k e^{j\nu^x_k} \qquad \text{in} \quad d^x_kq^x_k \end{aligned} \tag{2.61}$$

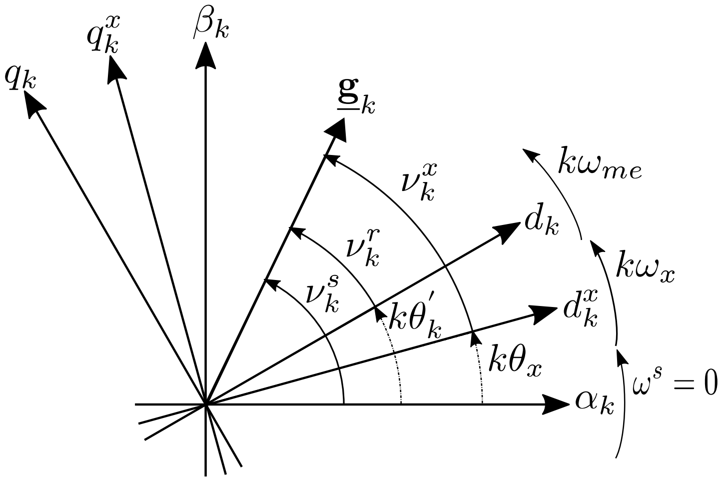

Figure 2.12: Relationship between stationary and rotating reference frames.

If equations (2.58) and (2.59) are written referring all the complex space-vector in the generic common reference frame $d_k^x q_k^x$ they become:

$$\underline{\boldsymbol{\lambda}}_{s,k} = L_{ss,k}\underline{\mathbf{i}}_{s,k} + \frac{n_b}{2} L_{m,k}\underline{\mathbf{i}}_{r,k} \tag{2.62}$$

$$\underline{\boldsymbol{\lambda}}_{r,k} = \frac{n}{2} L_{m,k}\underline{\mathbf{i}}_{s,k} + L_{rr}\underline{\mathbf{i}}_{r,k}. \tag{2.63}$$

Then, by substituting them into (2.52) and (2.55) respectively, with all the vectors referred to $d^x q^x$ as well, we obtain:

$$\underline{\mathbf{v}}_{s,k} = R_s\underline{\mathbf{i}}_{s,k} + L_{ss,k}\frac{d\underline{\mathbf{i}}_{s,k}}{dt} + \frac{n_b}{2} L_{m,k}\frac{d\underline{\mathbf{i}}_{r,k}}{dt} + jk\omega_x\underline{\boldsymbol{\lambda}}_{s,k} \tag{2.64}$$

$$\underline{0} = R_r\underline{\mathbf{i}}_{r,k} + L_{rr}\frac{d\underline{\mathbf{i}}_{r,k}}{dt} + \frac{n}{2} L_{m,k}\frac{d\underline{\mathbf{i}}_{s,k}}{dt} - jk\left(\omega_{me} - \omega_x\right)\underline{\boldsymbol{\lambda}}_{r,k} \tag{2.65}$$

In addition, extending to a multiphase case the approach used in [24], if we define the following vector transformations:

$$\underline{\mathbf{i}}_{s,k}^{'} = \frac{2}{n}\underline{\mathbf{i}}_{s,k} \tag{2.66}$$

$$\underline{\mathbf{i}}_{r,k}^{'} = \frac{2}{n}\sqrt{\frac{n_b}{n}}\underline{\mathbf{i}}_{r,k} \tag{2.67}$$

we can write:

$$\underline{\mathbf{v}}_{s,k} = R_s\underline{\mathbf{i}}_{s,k}^{'} + L_{ss,k}\frac{d\underline{\mathbf{i}}_{s,k}^{'}}{dt} + L_{m,k}^{'}\frac{d\underline{\mathbf{i}}_{r,k}^{'}}{dt} + jk\omega_x\underline{\boldsymbol{\lambda}}_{s,k} \tag{2.68}$$

$$\underline{0} = R_r\underline{\mathbf{i}}_{r,k}^{'} + L_{rr}\frac{d\underline{\mathbf{i}}_{r,k}^{'}}{dt} + L_{m,k}^{'}\frac{d\underline{\mathbf{i}}_{s,k}^{'}}{dt} - jk\left(\omega_{me} - \omega_x\right)\underline{\boldsymbol{\lambda}}_{r,k} \tag{2.69}$$

where

$$L_{m,k}^{'} = \frac{n}{2}\sqrt{\frac{n_b}{n}} L_{m,k}. \tag{2.70}$$

The corresponding equivalent circuit is shown in Fig. 2.13. It represent the k-th vector subspace of the machine, in an arbitrary rotating reference frame.

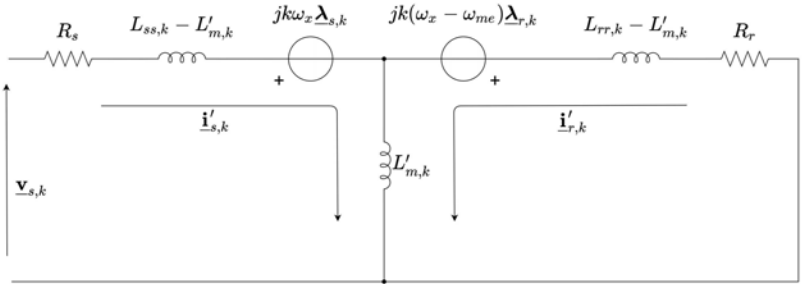

Figure 2.13: Complex vector equivalent circuit for the k-th vector subspace.

2.3.4 *The torque expression*

To complete the model we need also a formulation for the torque. In [28], with the use of the the co-energy function, the following expressions for the torque of 2-poles machines, with distributed and full-pitch concentrated winding respectively, are found:

$$\tau_m = -\frac{n}{2}\frac{n_b}{2} L_m^d \Im \left[e^{j\left(\theta_{me} + \frac{\alpha_r}{2}\right)} \underline{\mathbf{i}}_s^* \underline{\mathbf{i}}_r \right] \tag{2.71}$$

$$\tau_m = -\frac{n}{2}\frac{n_b}{2} \sum_{k=1}^{+\infty} L_{m,k}^c \Im \left[e^{jk\left(\theta_{me} + \frac{\alpha_r}{2} + \frac{\gamma_k}{k}\right)} \underline{\mathbf{i}}_{s,k}^* \underline{\mathbf{i}}_{r,k} \right] . \tag{2.72}$$

These expressions are similar to those derived for three-phase wound-rotor machines. The term $\frac{nb}{2}$ arises from the arbitrary constant in the definition of the rotor current complex space-vector and the inductance the sum of the $L_{m,k}$'s includes the equivalent of the turns ratio found in the usual model. Note that in these equations the complex space-vectors are defined in different reference frames, i.e. the stator current ones was defined in stationary reference frames, while the rotor current ones in rotating vector subspaces with angular speed $k\omega_{me}$. If we refer both the complex space-vectors, for each k-th vector subspace, in a common reference frame, and extend to any number of poles, we can write in a more general form:

$$\tau_m = -p\frac{n}{2}\frac{n_b}{2} \sum_{k=1}^{+\infty} L_{m,k} \Im \left[\underline{\mathbf{i}}_{s,k}^* \underline{\mathbf{i}}_{r,k} \right] \tag{2.73}$$

If we express each k-th harmonic components in its $d_k q_k$ reference frame, and expand the expression by writing the complex space-vectors as a complex number with their d_k axis and q_k axis components it becomes:

$$\tau_m = -p\frac{n}{2}\frac{n_b}{2}\sum_{k=1}^{+\infty} L_{m,k}\left(i_{r,d_k} i_{s,q_k} - i_{s,d_k} i_{r,q_k}\right) \tag{2.74}$$

where we can appreciate that the contribution of the first vector subspace (k=1) is identical to the one of a three-phase system.

2.3.5 *Considerations*

By looking at Table 2.1 and 2.2, and at the torque expressions that we have just described, we can generalize some considerations about MPMs with distributed or concentrated windings. In the tables for the five-phase machine the zero sequence is not shown because with a single and isolated neutral point, which usually is the case, it cannot exist. In the six-phase YY30 machine instead, the third vector subspace can be eventually excited, but only if the two three-phase sets share the same neutral point available also to the converter.

For the distributed winding cases, the only contribution to the torque generation comes from the fundamental reference frame, with no influence of the multiple harmonics available in the multiphase machine. This may make the control strategy a bit easier, but on the other hand, the control may face some issues due to the use of voltage source converters with PWM, because the absence of any inductance in the reference frames of the harmonics leaves the leakage inductances alone as the only reactive components. Since the value of these leakage inductances is typically very small, the inductive-resistive time constant of the harmonics equivalent circuit is very small as well and the voltage balance equation for the third and fifth harmonic will exhibit a very fast dynamic. As a consequence, the sudden rising or falling voltage edges of PWM will cause non-negligible harmonic current ripples. This effect could be mitigated with the selection of a suitable voltage modulation, but it cannot be completely eliminated.

For the full-pitch concentrated windings machines instead there are inductive contributions from the fundamental reference frame as well as from the harmonic reference frames. This aspect is design dependant, but it is important because it means that the leakage inductances are not alone anymore in the voltage dynamics of the harmonics, and the inductive-resistive time constant that affects the current ripple is larger. Moreover these harmonics can be exploited to produce a positive average electromagnetic torque. In particular the six-phase YY30 machine could potentially produce torque with third harmonics (as already mentioned, a common star point which is available to the converter is needed). The presence of coupling terms between harmonics of different order in full-pitch concentrated windings machines makes the torque regulation slightly more complicated. Such coupling terms, however, should be quantified for the specific design under consideration, in order to evaluate their overall importance.

2.4 CONTROL STRATEGY WITH FOC AND VSD

The theoretical principles of Field Oriented Control (FOC) aims to independently regulate the flux and torque of an AC machine, achieving the required decoupling by means of a mathematical transformation performed in real time. For this purpose, it is necessary to align the flux producing d-axis current with the flux axis, and this is done by proper selection of the reference frame in the Park's transformation. In Indirect Rotor Field Oriented Control (IRFOC) for IMs this alignment is performed based on an estimation of the slip. Then the flux is regulated solely by the d-axis current whereas the torque can be regulated through the q-axis current. Since the energy conversion for multiphase machines in the d_1q_1 plane ($\alpha_1\beta_1$ plane in the stationary reference frame) is exactly the same as in the three-phase case, as seen in (2.74), the principle of operation of field orientation is directly applicable to any n-phase machine if spatial harmonics are neglected. The control structure also follows the same nested approach used in three-phase machines, where reference voltages are obtained from the inner current control loops and the speed is regulated in an outer speed loop, see Fig. 2.14. In this typical structure, the speed loop provides the q_1-current reference whereas the d_1-current reference it is set to a constant value that provides rated flux in the base speed region and decreases in the field weakening zone. The controllers in both speed and current loops are typically of anti-wind-up proportional–integral (PI) type with limiters, that keep the drive operation within rated values. By setting appropriate d_1q_1 voltages, the VSD voltage references are then transformed into phase voltage references using the inverse generalized Park and Clarke transformations. The control action provided by the switching state is finally obtained from a pulse width modulator. So far, the FOC scheme is basically the same of a three phase machine, but it is still necessary to consider the additional degrees of freedom given by the others vector subspaces' components. In this regard, it is advisable to implement close-loop control with PIs also in the d_kq_k. In MPMs with some kind of concentration in the winding distribution these new control loops can be exploited to inject some precise harmonics in order to increase the average torque production. Nevertheless, also in distributed windings machine, where the currents in the vector subspaces that are not the fundamental one do not generate flux/torque, and thus must be kept to zero to avoid additional copper losses, it is advisable to close the control loops in the vector subspaces. Although in ideal conditions it seems sufficient an open-loop mode using zero inputs for the PWM stage, in actual

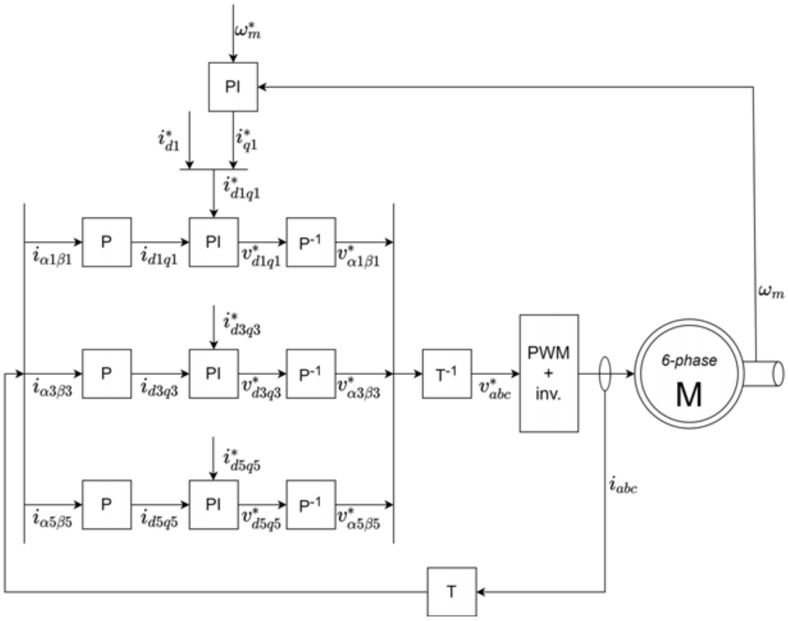

Figure 2.14: Control scheme for an IRFOC of a six-phase MPM.

machines the stator windings have some degree of asymmetry, while the power converter has a dead time that also induce k-th harmonic voltages, that will still produce unwanted k-th harmonic currents. The regulation of d_kq_k currents with $k \neq 3$ is sufficient in machines with multiple three-phase windings and multiple isolated neutral points. However, in machines with multiple three-phase windings and single neutral point, the control scheme must include additional loops for the zero sequence currents (d_3q_3), which can flow from one three-phase set to another, [37]. For example, in the six-phase YY30 machine, if the two three-phase set share the same neutral point isolated from the converter, then there can be triplen harmonics, but not in a standard form, in fact they have to comply the condition $i_{\alpha3} = -i_{\beta3}$, which is compatible with triplen harmonics of the form m $i_{a1} = i_{b1} = i_{c1} = I\cos(3\omega t)$ and $i_{a2} = i_{b2} = i_{c2} = -I\cos(3\omega t)$ flowing from the set $a_1b_1c_1$ to the set $a_2b_2c_2$, which generate only additional copper losses. In Fig. 2.14 the PI for the harmonics planes different from the fundamental are collocated in the d_kq_k rotating reference frames, however for harmonic suppression it may be more convenient to avoid the Park transformation and set the PIs in the $\alpha_k\beta_k$ reference frames (leaving only the fundamental component controlled in the d_1q_1 rotating reference frame), because the asymmetries induce currents in both synchronous and antisynchronous directions. PI controllers in stationary frame need to deal with the suppression of AC components and this can be problematic due to the limited bandwidth of PI controllers, however assuming that the degree of asymmetry is low, [37] states that this approach provides good performance.

3

THE WICSC MACHINE AND THE HPD APPROACH

In this chapter the design of the Wound Independely-Controlled Stator Coil (WICSC) machine is presented, and its capabilities are explained. Then, a possible control strategy under development is briefly presented. We will see that this strategy, called Harmonic Plane Decomposition (HPD) at KTH, takes advantage of an extension of the VSD theory seen in the previous chapter.

3.1 THE WICSC MACHINE

Requirements of electrical machines for Electric Vehicles (EVs) applications span various aspects such as high torque density, operation speed, efficiency, low rotor losses and thermal stress. For this reason designers often focus on distributed windings with high number of coils per pole, achieving high quality magnetomotive force and air-gap flux density, thus reducing rotor losses, rotor heating and vibrations. On the other hand, such configurations have drawbacks such as high costs of manufacturing and low slotting fill factor. In addition all the conventional industrial electric motors, have a fixed number of poles for their nature, and this means that they rely only on one specific maximum efficiency point. *Dajaku* and *Gerling* recently proposed and patented a novel stator cage winding for electrical machines trying to overcome some of these issues, [5]. The traction drive has been named Intelligent Stator CAge Drive (ISCAD). We will briefly introduce some of its innovative concepts from which also the WICSC machine has been derived.

3.1.1 *ISCAD*

The main peculiarity of ISCAD is undoubtedly its stator cage. In fact its stator winding consists of conductor bars in each slot, short-circuited at one axial end as it normally happens in a squirrel cage rotor. On the other end, the conductors are connected to the supply converter. The resulting design, shown in Fig. 3.1 can be considered multi-phase and multi-pole, as each conductor can be seen as a phase winding itself somehow. At low speed/high torque the machine can be controlled to operate with a high number of pole pairs, while at high speed/low torque the number of pole pairs can be reduced. Some other advantages of the stator cage design are very high fill factors, compact end winding, high thermal capability (because of low thermal resistance between the stator bars and the core), the possibility to use

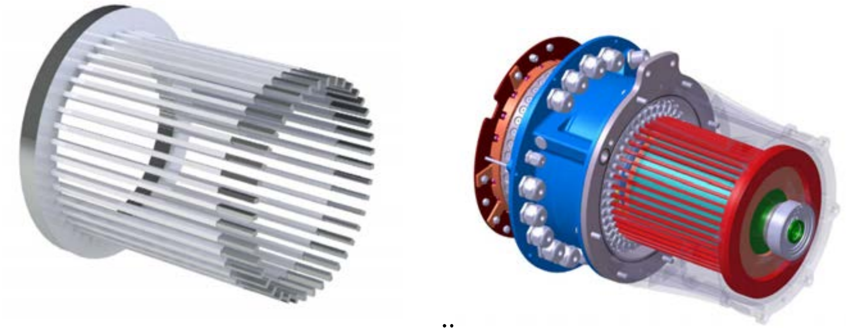

(a) Stator cage with massive alluminum bars.

(b) CAD of the ISCAD machine.

Figure 3.1: ISCAD concept, [30].

aluminium instead of copper (lighter and less expensive), and easier manufacturing. Another key aspect of ISCAD is that it works with low voltage ($48V$). This is benefical for the battery design, as it allow a significant reduction of the number of cells connected in series, but carries also some major downsides. In fact low voltage implies high currents, which means that the converter and the battery need to be specifically designed for the purpose, since they are not compatible with standard EVs high-voltage system.

3.1.2 *WICSC design*

In order to decrease the high currents that ISCAD needs to cope with, a wound stator is needed. Bitsi, Wallmark and Bosga proposed in [3] a design that maintains the pole and phase changing capabilities, with a Gramme-type winding (or Pacinotti-type winding in a more Italian fashion), made of multiturn coils wound around the stator core as described in Fig. 3.2. Each stator coil is wound independently from the others, therefore the machine is called Wound Independely-Controlled Stator Coil (WICSC). The stator core has Q_s slots in which

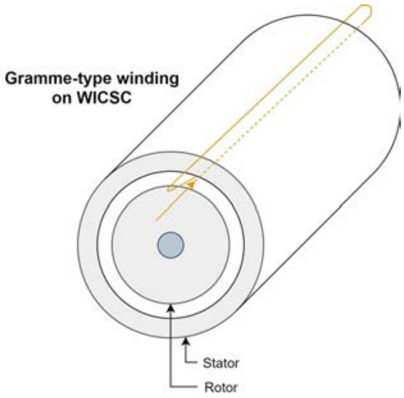

Figure 3.2: Gramme-type winding on the WICSC machine, wound around the stator core.

N_t turns of copper conductors are wound. The prototype that is being built and set-up at KTH laboratories has $Q_s = 36$, and it is shown in Fig. 3.3, where the conductors in the outside can be noticed. The external conductors do not play an active role, and they contribute in terms of losses, but they are needed as return conductors: it is the only way to build a machine with ISCAD concepts but with a number of turns higher than one to reduce the currents in favour of high voltages. Another downside of this winding technique is that at the moment it is expensive, since it requires complex and time-consuming handwork, and the quantity of copper needed is higher compared to a normal machine. Also thermal heat dissipation could be affected by this design, but this aspect has not ben investigated yet, and will not be taken into consideration in this work. Since the prototype is built on the basis of a standard three-phase 15kW ABB induction motor, it shares with it also the regular squirrel cage rotor with $N_b = 28$ rotor bars.

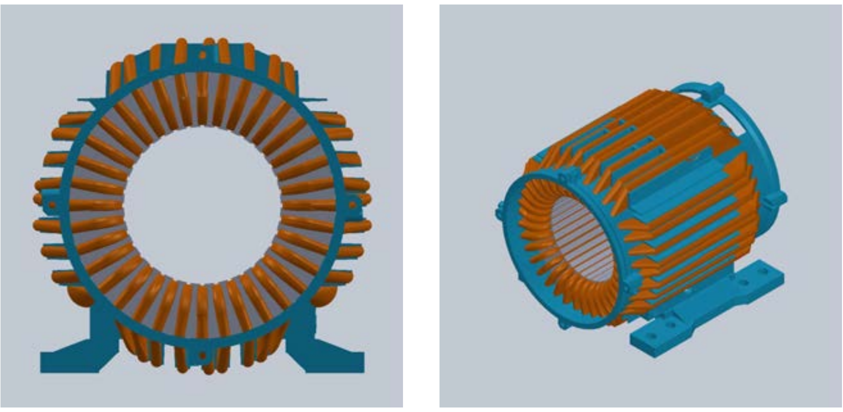
(a) Axial view.
(b) Isometric view.

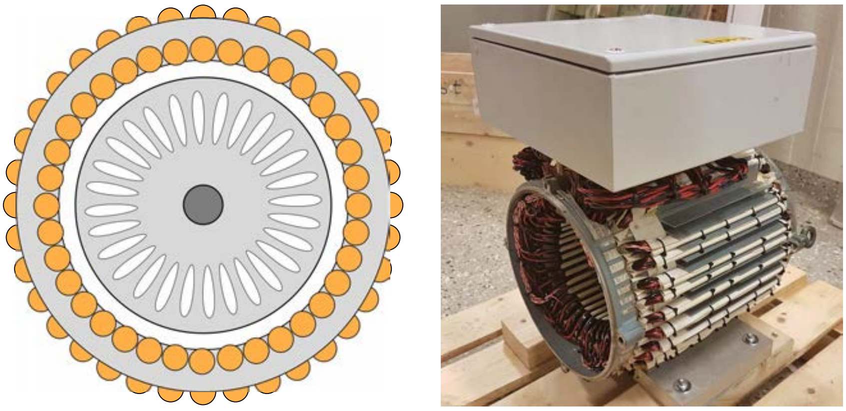
(c) Cross-sectional scheme.
(d) Actual prototype.

Figure 3.3: Renderings and picture of the WICSC prototype, without the rotor except for (c).

3.1.3 *WICSC pole and phase changing capabilities*

The Q_s stator coils are individually wound in separated stator slots around the stator joke, and considering only one of them, it produces flux in the $\pm\phi$ azimuthal direction. Therefore supplying only one stator coil would result only in a leakage field penetrating the air-gap (especially if the iron of the stator is assumed to have high relative permeability). To redirect magnetic flux density in the rotor like in a traditional machine, at least two stator coils with opposite current are needed. The terminals of the stator coils are individually accessible, and in the considered prototype all the positive terminals are connected to a dedicated half-bridge output of an inverter, whereas the negative terminals are shorted together in a single isolated star point, as shown in Fig. 3.4. The individually inverter-connected stator coils give the freedom to control the currents in each slot independently, provided that the sum of the currents entering the neutral point sum to zero, which is not a problem since supplying configurations with non-zero sum currents would only contribute to magnetize the stator joke and should be avoided. This configuration provides the possibility to reconfigure online the number of phases n, and the number of poles $2p$, during operation. In common machines the windings belonging to one phase are series-connected such that the resulting magnetic axis points in the radial direction across the airgap, and each phase is connected to one inverter-output. In the WICSC machine, the voltage of different coils can be controlled to produce the same or opposite current, so that a virtual phase can be achieved. The concept of virtual phase is explicated in Fig. 3.5, where the simplest case is taken in consideration, i.e. the case 18 phases - 2 pole configuration, in which to produce virtual phases replicating a regular machine two adjacent coils need to carry currents shifted by $\pi/18$, and a virtual phase is made up of a coil and its opposite (placed after π mechanical degrees), which carry the opposite current. All the possible integer-slot phase-pole configurations for the 36 slots machine are shown in Table 3.1. In Fig. 3.6, where the external conductors have been neglected since as

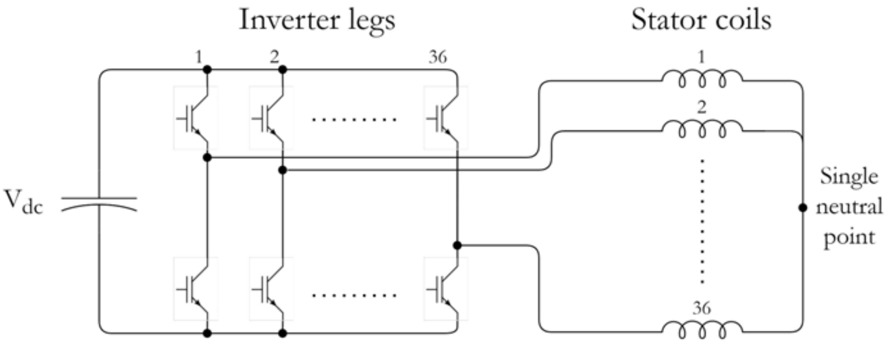

Figure 3.4: Schematic of the driveline of the prototype.

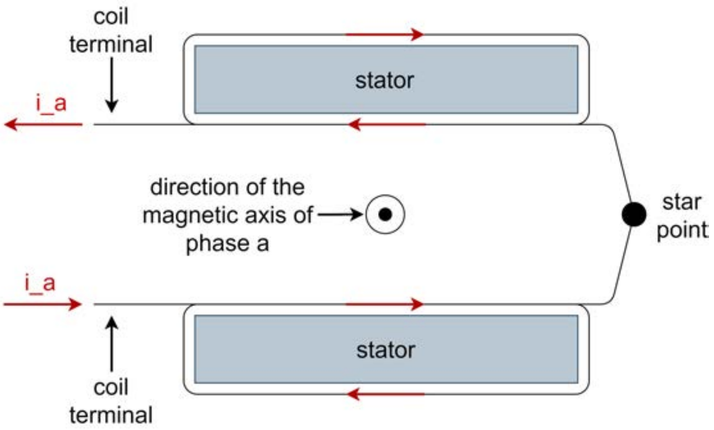

Figure 3.5: Virtual phase concept for the WICSC machine, side sectional view (18 phases - 2 poles configuration).

Table 3.1: Phase and pole configurations

Phases (n)	Pole-pairs (p)	Slots per pole per phase (q_s)
3	1	6
	2	3
	3	2
	6	1
6	1	3
	3	1
9	1	4
	2	2
18	1	1

already mentioned they do not play an active role, it is shown how to achieve some of the possible phase-pole configurations.

It is important to underline that the coils belonging to the same virtual phase are not connected in series, thus it is necessary to ensure by means of current controllers that in the case of configurations with more than one slot per pole per phase ($q_s > 1$), two adjacent slots belonging to the same virtual phase conduct the same current. In addition, it is also to be ensured that two opposing slots (in electrical degrees) belonging to the same virtual phase conduct the same current in amplitude but with opposite sign. In principle this last point should be ensured by simply supply opposite voltages at the coils terminals, but in real world conditions special voltage control is required to compensate practical differences between stator coils. This particular aspect, however, will be not considered in this work.

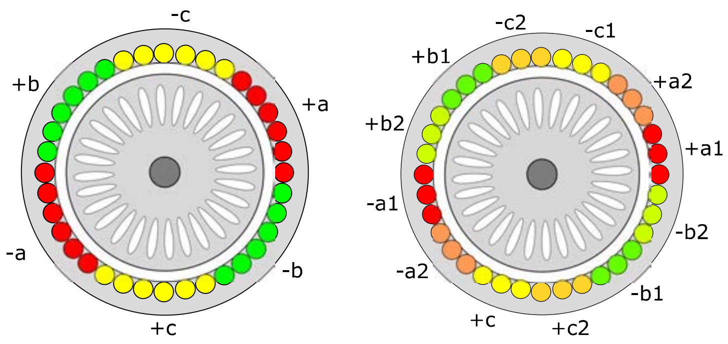

(a) 3 phases, 2 poles. (b) 6 phases, 2 poles.

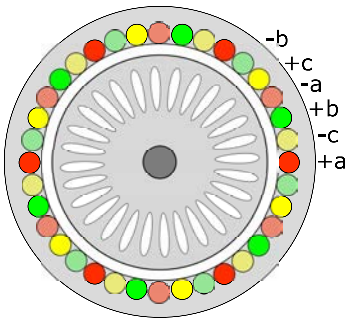

(c) 3 phases, 12 poles.

Figure 3.6: Some of the possible configurations for the WICSC machine.

3.2 HARMONIC PLANE DECOMPOSITION

In multiphase electrical machine with variable phase-pole configurations, the VSD theory, presented in Chapt. 2, leads to a varying numbers of vector spaces when changing the number of phases. Consequently, the model and current control can become discontinuous. For this reason the research group of the Division of Electric Power and Energy System at KTH Royal Institute of Technology is developing a technique that unifies the Clarke transformation for all possible phase-pole configurations such that a fixed number of orthogonal harmonic planes are created, which facilitates the current control during reconfigurations. They called this technique Harmonic Plane Decomposition (HPD). A detailed theoretical formulation will be soon be presented by the KTH research group in [27, 38], where also a Discrete Fourier Transformation (DFT) interpretation will be given, but here a simplified overview is given.

The sequence of transformations of HPD is very similar to VSD, however they are based on the physical winding arrangement, which is fixed and common to all phase-pole configurations, rather than on the phase within one electrical pole. A base case, with m_b phases and p_b pole-pairs, needs to be identified. The base case is the only phase-pole configuration which can describe all the possible others, with a suitable redefinition of its magnetic axes. In short, always the same generalized Clarke transformation is used, i.e. the one of the base case, even when the number of phases is lower than m_b and according to VSD a lower rank matrix would be sufficient. This means that we will always deal with the same vector-spaces generated by the VSD of the base-case. We will rename those vector-spaces as harmonic planes when we work with different configurations, in order to distinguish them from the VSD approach. For the sake of understanding and without loss of generality let us take into consideration as an example the six phase YY30 machine introduced in Chapt. 2. Its magnetic axis in the practical or fundamental reference frame are shown in Fig. 2.6. The same magnetic axis distribution can be used to represent a three-phase machine, where the two sets of three-phase windings are supplied with the same current. In that case, the phase belts of the phases a_1 and a_2 conduct the same current, and the generic vector variables becomes $x_{a1} = x_{a2} = x_a$ and the same for phase b and c, as shown in Fig. 3.7.

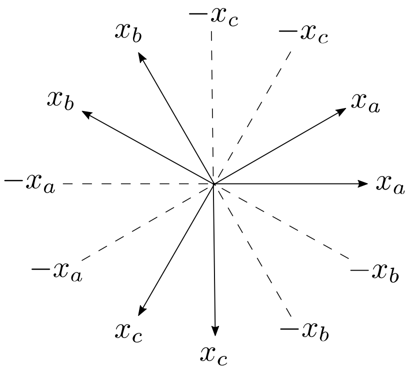

Figure 3.7: A six-phase YY30 machine in a three-phase configuration.

Note that is not true for all the quantities, this is very important and is somehow the core of why HPD is necessary. In fact, if for the currents a vector that has the form $\mathbf{i}_{abc} = [i_a \; i_a \; i_b \; i_b \; i_c \; i_c]^T$ is indeed what we want to achieve, the same cannot be true for the voltages, since the two phase belts $a1$ and $a2$ do not share the same flux linkage (remember that they are not series connected), and thus simply applying the same voltage would not end up in equal currents. Nevertheless, HPD with a base-case with $m_b = 6$ can provide us the current references needed to supply the correct voltages of a three-phase configuration (i.e. that make the currents two-by-two equals). More about the six-phase YY30 machine and operating it as a three-phase one will follow in the next chapter, but for the moment let us go back to the WICSC machine, and consider a base-case with $m_b = Q_s/2 = 18$. Similarly to the YY30 machine, also in this case the magnetic axes can be redefined to recreate different configurations, and for example if we want a three-phase/2 poles configuration, we want the currents of the first six coils to be equal and so on (see Fig. 3.6a). Furthermore, also in this case the coils belonging to the same virtual phase do not share the same flux linkage, and thus the configuration cannot be achieved simply supplying the same voltage. The only difference is that in the WICSC machine also the base-case is achieved with virtual phases, while in the previous example of the YY30 machine in the base-case we are dealing with a regular machine, but this does not affect the generation of current references with HPD.

3.2.1 *Vector-space distribution*

To have a better understanding of HPD we can see what happens when we apply the Generalized Clarke transformation to the vector of currents that we want to achieve in the fundamental reference frame when we want to run the WICSC machine with a configuration different from the base-case. For example for the aforementioned three-phase/2 poles configuration the current vector has the first six currents equal, the next six equal and shifted by $\pi/3$ electrical degrees with respect to the first six, and the last six equal and shifted by $2\pi/3$ with respect to the first six. If the generalized Clarke transformation of the base-case ($m_b = 18$) is applied to such a vector what we get in the harmonic planes, i.e. the components i_{α_h} and i_{β_h}, is shown in Fig. 3.8, where currents of $1A$ at $50Hz$ for the input vector have been considered as an example. What we notice in Fig. 3.8 is the presence of components at fundamental frequency in the first harmonic plane but also in the 5-th, 7-th, 11-th, 13-th, and 17-th. We could say that the space-vector $\underline{\mathbf{i}}_1$ that you normally get in the three-phase VSD, in the HPD with a base case with higher number of phases spreads on multiple harmonic planes. In addition, it can appear with different amplitude, show some shifting angle, and could even appear as a negative sequence (β component leading the α component). Then we can talk about vector-space distribution, which by the way is different from harmonic mapping. This can be clarified looking at Fig. 3.9, in which the input current vector in the fundamental reference frame replicates a six-phase configuration (groups of three slots of the WICSC machine carry the same current), but time harmonics have been superimposed. In that particular example there is $1A$ at fundamental frequency of $50Hz$, $1A$ of 3-rd order time-harmonic, $1A$ of 5-th order, and $0.2A$ of 13-th time harmonic. According to the VSD theory for a six-phase asymmetric machine (see [39]):

- the first and 13-th time harmonic are mapped into the first vector subspace (i.e. into the space vector $\underline{\mathbf{i}}_1$);
- the 3-rd time harmonic is mapped into the 3-rd vector subspace (i.e. into the space vector $\underline{\mathbf{i}}_3$);
- the 5-th time harmonic is mapped into the 5-th vector subspace (i.e. into the space vector $\underline{\mathbf{i}}_5$);

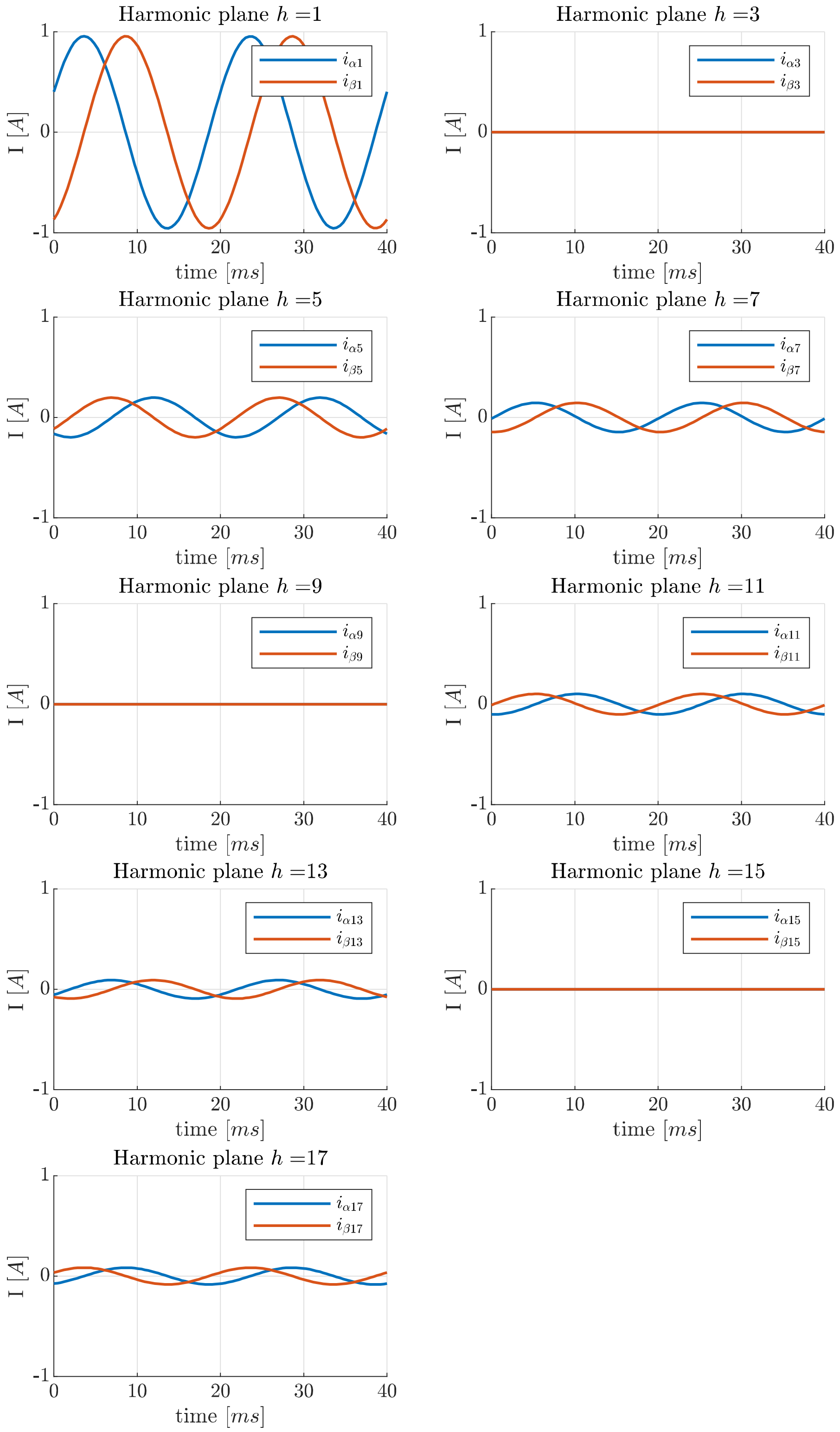

Figure 3.8: HPD ($m_b = 18$, $p_b = 1$) of a three-phase/2 poles configuration.

and this is the harmonic mapping. Then, the space-vector mapping is how this space-vectors spreads into the different harmonic planes of the base case, which in this particular case is the following:

- $\underline{\mathbf{i}}_1$ appear in the first and in the 13-th harmonic plane as a positive sequence, and in the 11-th as a negative sequence;
- $\underline{\mathbf{i}}_3$ appear in the 3-rd and in the 15-th harmonic plane as a positive sequence, and in the 9-th as a negative sequence;
- $\underline{\mathbf{i}}_5$ appear in the 5-th and in the 17-th harmonic plane as a positive sequence, and in the 7-th as a negative sequence;

The 13-th order time harmonic has been added for the sake of understanding that higher-order time harmonics that are mapped into the same vector subspace according to the VSD theory for a n-phase machine, follow the main one (the fundamental in this example) in the harmonic planes of the base case with m_b phases, thus we can talk about the whole vector distribution.

With the DFT interpretation of the HPD it can be shown that the the amplitude of the k-th space-vector that appear in the h-th harmonic plane is scaled by a factor:

$$K_{d,h} = \frac{\sin\left(\dfrac{h\pi}{n2p/p_b}\right)}{q_s \sin\left(\dfrac{h\pi}{q_s n2p/p_b}\right)} \tag{3.1}$$

where we p is the number of pole-pairs, and q_s the number of slot per poles per phase, in the n-phase configuration. It has been termed $K_{d,h}$ because in case of $p_b = 1$ it coincides with the winding distribution factor.

It is also to note that the configurations with an even number of pole-pairs, with $p_b = 1$, would result in even-order space harmonics in mechanical angles, which cannot be represented from VSD and HPD which consider only odd-order harmonics. Therefore another appropriate base-case for even pole-pairs configurations while retaining the dimensions of the original base case needs to be defined. Anyhow, this work is focused on the investigation of the change of the number of phases only, and this is left for future research projects on the WICSC machine.

3.2.2 *Generation of current references*

Let us suppose that to control the base-case we have a set of PIs that control d and q components of the vector subspaces or harmonic planes (since for the base-case they coincide). If we want to create a different configuration we can use a "reverse engineering" approach. For example we know that if we want to have a three-phase current

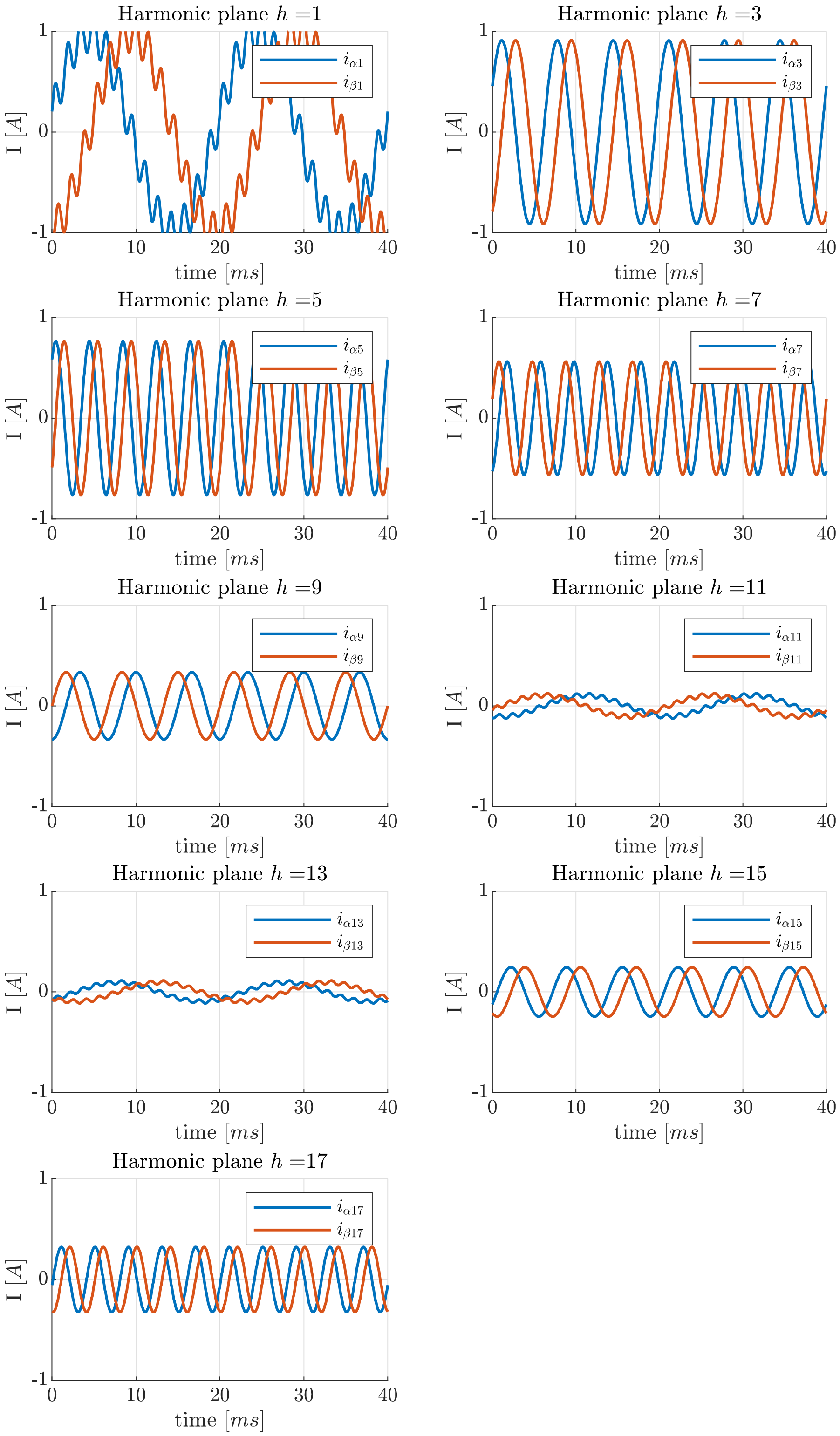

Figure 3.9: HPD ($m_b = 18, p_b = 1$) of a six-phase/2 poles configuration, with 3-rd, 5-th, and 13-th time harmonics of the same amplitude of the fundamental in the instantaneous values of the currents in $abc/123$ reference frame.

configuration on the WICSC machine, the HPD of such a configuration should look like Fig. 3.8. This means that in some harmonic planes components must be generated at fundamental frequency (as a direct or indirect sequence), with an amplitude scaled by a factor that is given by Eq. (3.1), and with a certain phase angle with respect to the others harmonic planes. To do so, since the PI controllers are supposed to be in rotating reference frames, the Park transformation needs to be adapted. Instead of synchronizing the h-th harmonic plane components with an angle that is h times the rotor flux angle $\theta_{\underline{\lambda}_{r,1}}$, only $\left(\pm\theta_{\underline{\lambda}_{r,1}} + \sigma\right)$ is used, with the plus sign in the harmonic planes where a direct sequence is needed, or the minus sign in the harmonic planes where an inverse sequence is needed, and where σ is responsible of the required phase shift. To summarize:

1. The d and q axis current references of the fundamental complex-space vector are given as usual by the flux and torque references;
2. Those references are scaled by the factors given by Eq. (3.1) and become the reference to the d and q axis of the various harmonic planes;
3. The modified inverse-Park transformation generates voltages references at fundamental frequencies in all the harmonic planes where it is necessary.

These passages will become clearer in the next chapter.

4

A SWITCHABLE THREE AND SIX PHASE MACHINE WITH HPD

In this chapter the phase-changing capabilities of the HPD approach are finally put to the test with a six phase YY30 machine. It has not been used a WICSC machine model not only because simply it was not ready (theory of Chapt. 2 cannot be applied straightforward to such a machine), but also because there was the will to start from a simple example, reducing the complexity of the system (for example in such a machine we will define a base-case with real and not virtual phases), and for the moment proving the feasibility of such a challenge.

4.1 MODELLING OF A SIX PHASE, CONCENTRATED WINDINGS, INDUCTION MACHINE

First of all, a model of a YY30 machine needs to be built. We have already seen how to do that extensively in Chapt. 2. If we choose a stationary reference frame (i.e. $\omega_x = 0$), the equations needed for an $\alpha\beta$ model of the machine are the following:

$$\underline{\mathbf{v}}_{s,k} = R_s \underline{\mathbf{i}}_{s,k} + \frac{d\underline{\boldsymbol{\lambda}}_{s,k}}{dt} \tag{4.1}$$

$$\underline{0} = R_r \underline{\mathbf{i}}_{r,k} + \frac{d\underline{\boldsymbol{\lambda}}_{r,k}}{dt} - jk\omega_{me}\underline{\boldsymbol{\lambda}}_{r,k} \tag{4.2}$$

$$\underline{\boldsymbol{\lambda}}_{s,k} = L_{ss,k}\underline{\mathbf{i}}_{s,k} + \frac{n_b}{2} L_{m,k}\underline{\mathbf{i}}_{r,k} \tag{4.3}$$

$$\underline{\boldsymbol{\lambda}}_{r,k} = \frac{n}{2} L_{m,k}\underline{\mathbf{i}}_{s,k} + L_{rr}\underline{\mathbf{i}}_{r,k}. \tag{4.4}$$

These equations can be easily implemented in the Simulink environment. Fig. 4.1 shows the vector model of the generic $k-th$ vector subspace, and in the case of the YY30 machine that we want to consider, only the first and 5-th need to be modelled like that. In fact if we consider a single isolated neutral point, homopolar components can flow only from one three-phase set to the other, and we have already seen in Chapt. 2 that in this case for the 3-rd vector subspace there is the constraint $i_{\alpha 3} = -i_{\beta 3}$, [37]. Then if we write the real and imaginary part of the voltage balance equations, i.e. write the equations for $\alpha 3$

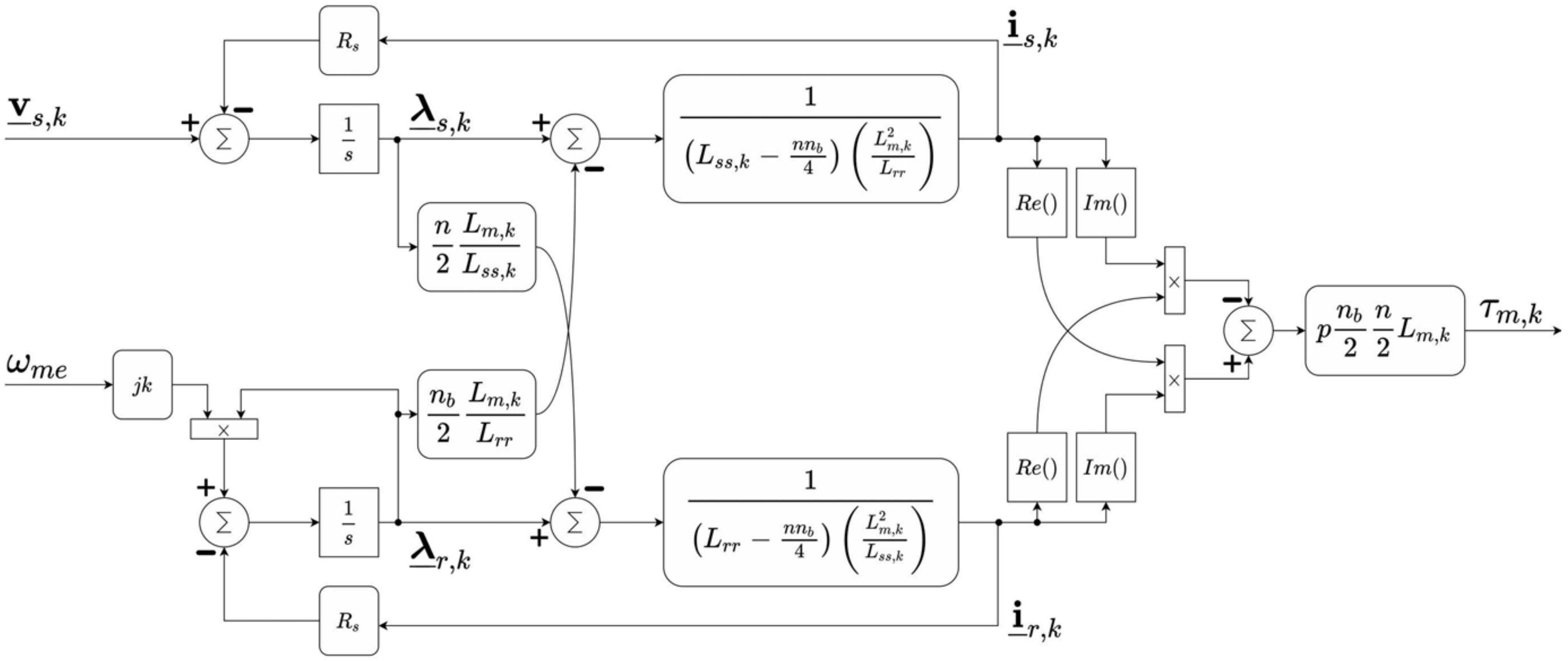

Figure 4.1: Vector model of the $k-th$ vector subspace/harmonic plane in a stationary reference frame.

and β_3 separately, and then subtract them and use the constraint, we can get to the following set of equations:

$$\begin{aligned}
v_{s,\alpha 3} - v_{s,\beta 3} &= 2R_s i_{s,\alpha 3} + 2\frac{d\lambda_{s,\alpha 3}}{dt} && (4.5)\\
0 &= 2R_r i_{r,\alpha 3} + 2\frac{d\lambda_{r,\alpha 3}}{dt} && (4.6)\\
\lambda_{s,\alpha 3} &= L_{ss,3} i_{s,\alpha 3} + \frac{n_b}{2} L_{m,3} i_{r,\alpha 3} && (4.7)\\
\lambda_{r,\alpha 3} &= \frac{n}{2} L_{m,3} i_{s,\alpha 3} + L_{rr} i_{r,\alpha 3} && (4.8)\\
i_{s,\alpha 3} &= -i_{s,\beta 3} && (4.9)\\
i_{r,\alpha 3} &= -i_{r,\beta 3}. && (4.10)
\end{aligned}$$

which can also be implemented in Simulink as shown in Fig. 4.2. Remember that these currents do not produce any torque, and are responsible only of losses.

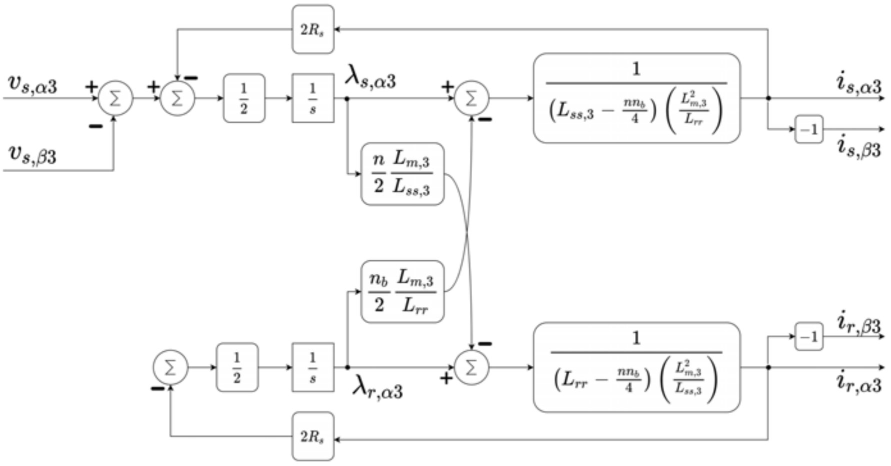

Figure 4.2: Model of the 3-rd vector subspace/harmonic plane.

The complete motor model is shown in Fig. 4.3. The vector of voltages fed by the inverter is transformed into the practical reference frame and the generalised Clarke transformation as defined in (2.6) is applied. Then the components of the obtained vector $\mathbf{v}_{\alpha\beta 0}$ corresponds to real and imaginary part of the k-th space-vector, which becomes the input of the k-th vector subspace/harmonic plane model, i.e. the ones shown in Fig. 4.1 and 4.2. The output torques are then added together, and stator currents are simply transformed back to the practical reference frame. For the rotor currents, the obtained space-vectors $\underline{\mathbf{i}}_{r,k}$ are referred to a stationary reference frame, different from the definition in Eq. (2.39). They can be adjusted with the factor $e^{jk\theta_k'}$, where θ_k' is the one defined in (2.60), before transforming them into the rotor loops currents. The parameters of the YY30 six-phase motor used in the simulation that will come are shown in Tab. 4.1. Inductances of the

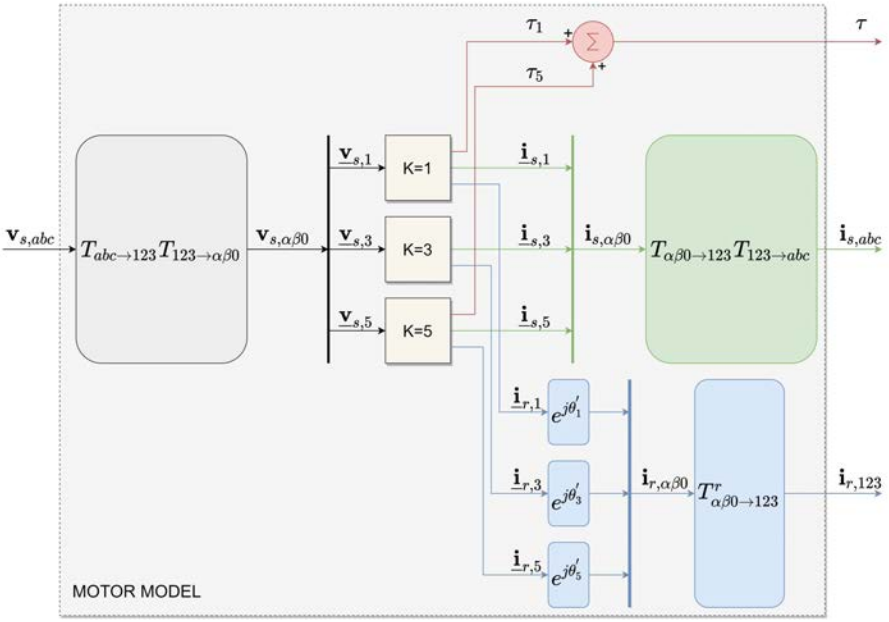

Figure 4.3: Scheme of the motor model.

various vector subspaces have been calculated as shown in Chapt. 2, for the full-pitch concentrated winding case.

4.2 HPD-BASED CONTROL TECHNIQUE

For the six-phase mode of operation the scheme of Fig. 2.14 and described in Chapt. 2. For the first vector subspace/harmonic plane, the current references are as usual given by the reference flux and the torque demand. An IRFOC needs to be implemented, for the synchronization with the rotor flux, but it does not change from the usual three-phase implementation. The scheme used is shown in Fig. 4.4. To

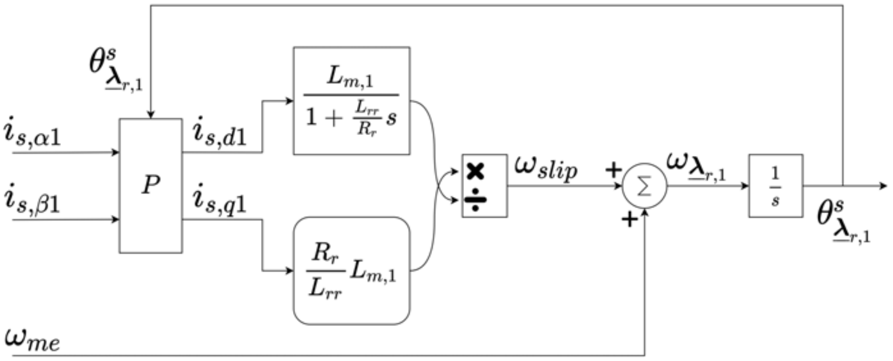

Figure 4.4: IRFOC scheme.

change the configuration to a virtual three-phase during operation, an HPD approach is used, so that the size of the vectors and matrices that

Table 4.1: Parameters of the considered YY30 six-phase motor.

	symbol	*value*	*unit*
phases	n	6	/
pole-pairs	p	4	/
rotor bars	N_b	40	/
rotor bars per pole-pair	n_b	10	/
stator turns	N_t	36	/
stator resistance	R_s	1.3	$[\Omega]$
rotor bar resistance	R_b	0.4	$[m\Omega]$
end-ring segment resistance	R_e	0	$[m\Omega]$
rotor bar inductance	L_b	0.043	$[\mu H]$
end-ring segment inductance	L_e	0	$[\mu H]$
stator model inductances	$L_{ss,1}$	102.2	$[mH]$
	$L_{ss,3}$	13.7	$[mH]$
	$L_{ss,5}$	7.3	$[mH]$
model mutual inductances	$L_{m,1}$	285.9	$[\mu H]$
	$L_{m,3}$	83.2	$[\mu H]$
	$L_{m,5}$	37	$[\mu H]$
rotor model inductance	L_{rr}	12.7	$[\mu H]$
rotor model resistance	R_r	0.153	$[m\Omega]$
friction	B	0.001	$[kg \cdot m^2]$
inertia	J	0.095	$[N \cdot m \cdot s]$
DC-bus voltage	V_{DC}	150	$[V]$

we are dealing with never changes. The base-case set is the regular six-phase configuration, with its normal number of pole-pairs since we will perform only a switch of the number of phases and not of the number of poles. The VSD, coincident with the HPD of a set of balanced six phase currents, is shown in Fig. 4.5. It can be compared with the HPD of six currents replicating a balanced three-phase configuration ($i_{a1} = i_{a2}, i_{b1} = i_{b2}, i_{c1} = i_{c2}$) shown in Fig. 4.6. The space-vector of a three-phase machine spreads into the first and 5-th harmonic planes of the six-phase machine. The amplitude is scaled by the factors given by Eq. (3.1), where we can consider $q_s = 2$ for the three-phase configuration ($q_s = 1$ for six-phase). What we get in this case is:

$$K_{d,1} = 0.9659 \tag{4.11}$$

$$K_{d,5} = 0.2588 \tag{4.12}$$

This factors can be used to scale the d_1q_1 references that regulate flux and torque in the six phase configuration before passing them as references for the first and 5-th harmonic (the latter in the six-phase mode is kept with null reference). Anyhow this is not enough since we still need to modify the Park transformation when we want to recreate the three-phase configuration. The one defined in (2.13) synchronize the 5-th vector subspace components with five times the rotor flux angle, but in Fig. 4.6 it is clear that in the 5-th harmonic plane we want a negative sequence at fundamental frequency. This is why we need to substitute $5\theta_{\underline{\lambda}_{r,1}}$ with $-\theta_{\underline{\lambda}_{r,1}}$. Then the Park transformation used in the three-phase mode becomes:

$$P_{3ph} = \begin{bmatrix} \cos(\theta_{\underline{\lambda}_{r,1}}) & \sin(\theta_{\underline{\lambda}_{r,1}}) & 0 & 0 & 0 & 0 \\ -\sin(\theta_{\underline{\lambda}_{r,1}}) & \cos(\theta_{\underline{\lambda}_{r,1}}) & 0 & 0 & 0 & 0 \\ 0 & 0 & \cos(3\theta_{\underline{\lambda}_{r,1}}) & \sin(3\theta_{\underline{\lambda}_{r,1}}) & 0 & 0 \\ 0 & 0 & -\sin(3\theta_{\underline{\lambda}_{r,1}}) & \cos(3\theta_{\underline{\lambda}_{r,1}}) & 0 & 0 \\ 0 & 0 & 0 & 0 & \cos(-\theta_{\underline{\lambda}_{r,1}}) & \sin(-\theta_{\underline{\lambda}_{r,1}}) \\ 0 & 0 & 0 & 0 & -\sin(-\theta_{\underline{\lambda}_{r,1}}) & \cos(-\theta_{\underline{\lambda}_{r,1}}) \end{bmatrix} . \tag{4.13}$$

In addition also a fixed angle should be added to $-\theta_{\underline{\lambda}_{r,1}}$ in the 5-th harmonic plane because we want a particular shift with respect to the fundamental harmonic plane, but in this very particular case we can see from Fig. 4.6 that the α_5 component is perfectly in phase with the β_1 component, and the β_5 component is perfectly in phase with the α_1 component, thus the scaled (by $K_{d,5}$) flux and torque regulating current references can be exchanged in the 5-th harmonic plane, without any further modifications to the Park transformation. The complete control scheme is shown in Fig. 4.7. When the three-phase mode is triggered, the flux and torque reference currents are scaled by the factor $K_{d,1}$ before passing them as a reference for the d_1 and q_1 axis respectively,

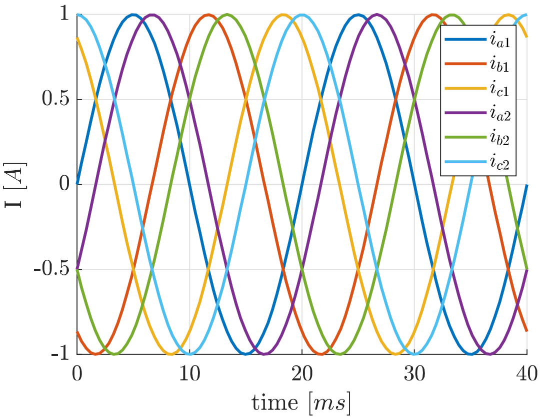

(a) Practical reference frame.

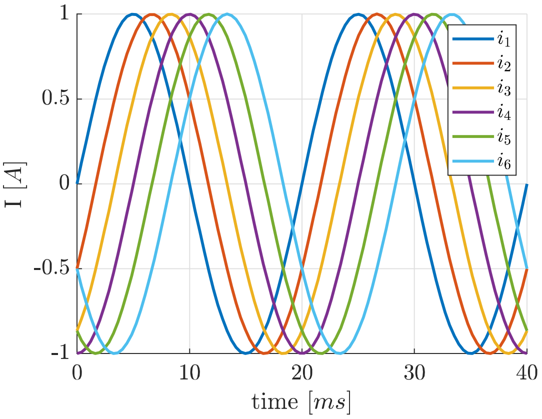

(b) Fundamental reference frame.

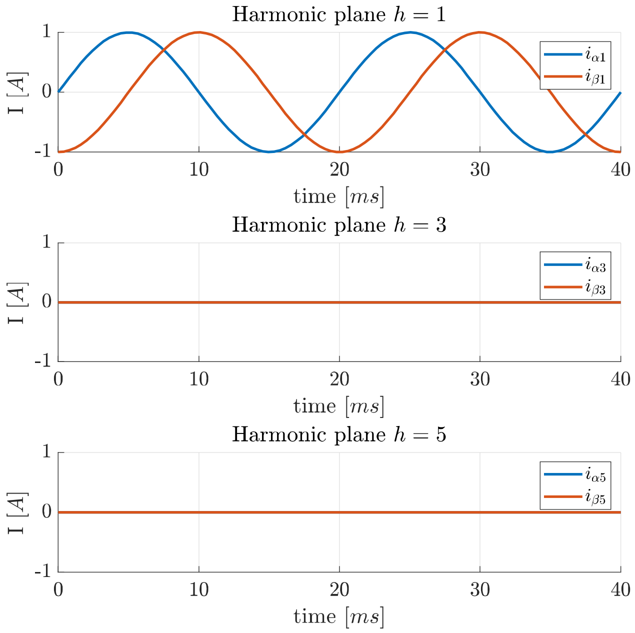

(c) $\alpha_h\beta_h$ stationary reference frames.

Figure 4.5: VSD coincident with HPD ($m_b = 6$) for the six-phase configuration.

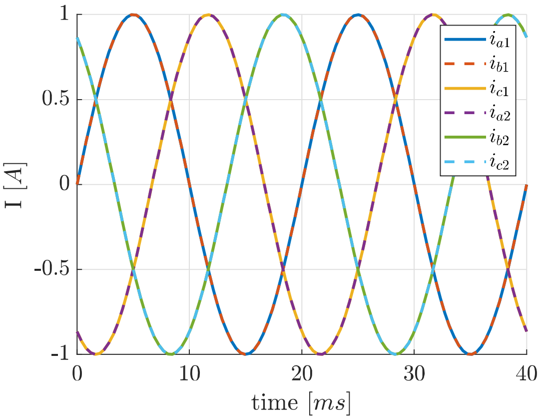

(a) Practical reference frame.

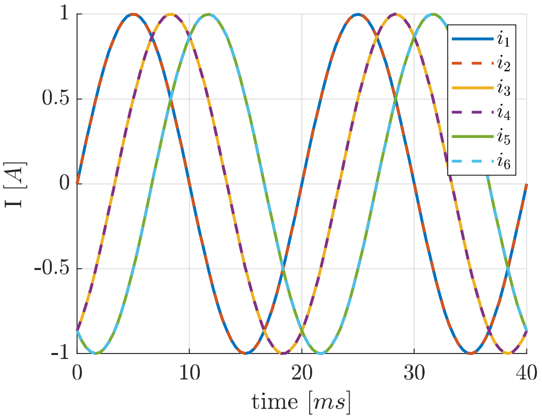

(b) Fundamental reference frame.

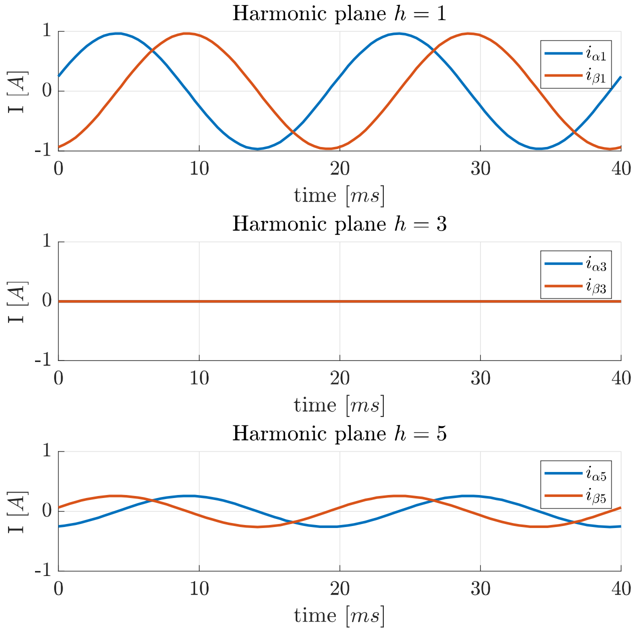

(c) $\alpha_h \beta_h$ stationary reference frames.

Figure 4.6: HPD ($m_b = 6$) for the three-phase configuration.

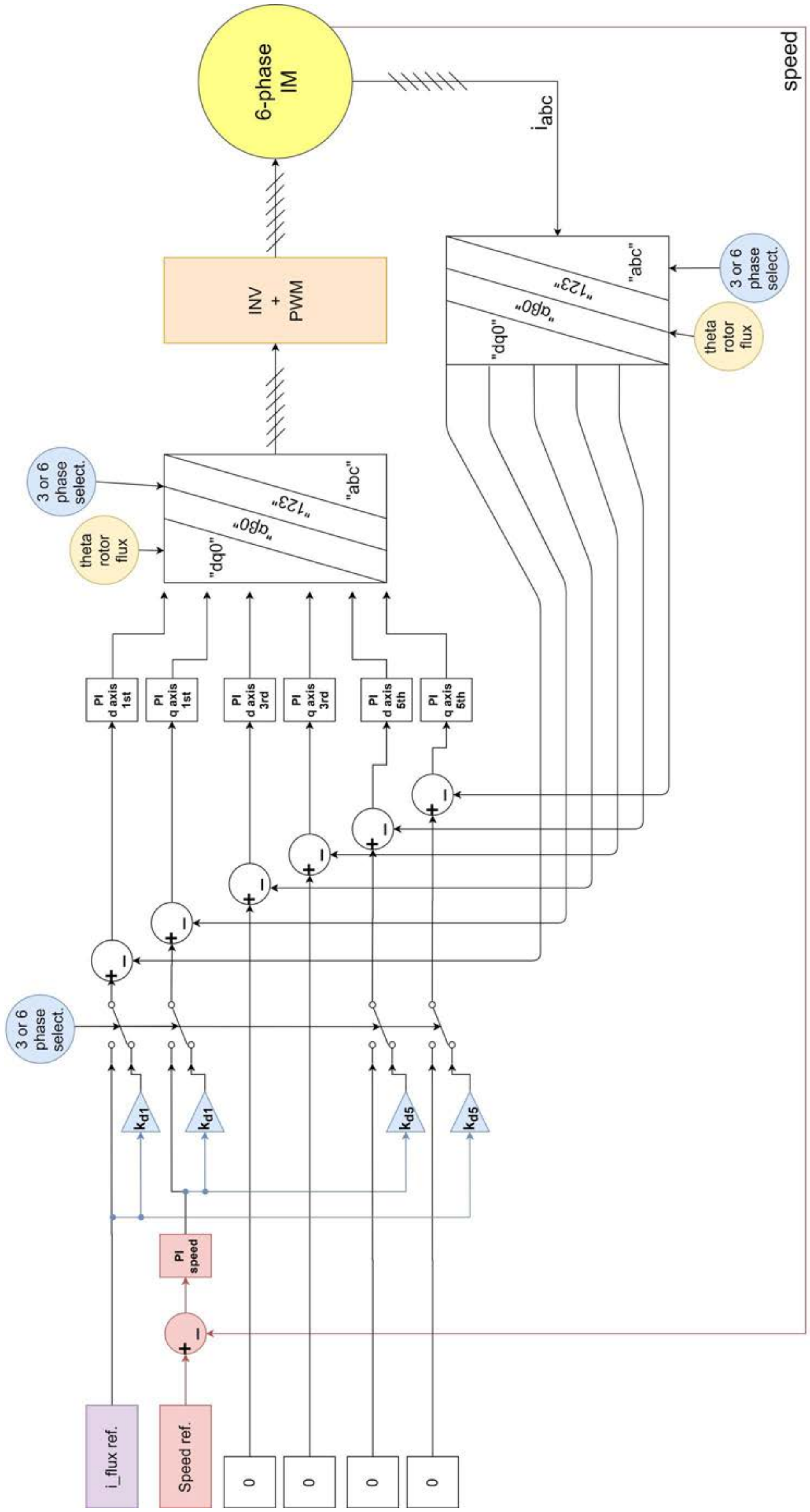

Figure 4.7: Control scheme.

and scaled by the factor $K_{d,5}$ before passing them as a reference for the q_5 and d_5 axis respectively. In all the transformation passages the standard six-phase Park transformation is substituted by the one in (4.13), whereas the IRFOC scheme and the motor model stay the same.

4.3 SIMULATIONS

All the simulations presented here have been performed following the same path:

1. the initial configuration is the regular six-phase mode;
2. flux current reference is set to be $3A$;
3. speed reference is set to be $900rpm$;
4. at $t = 3s$ a $20Nm$ load is inserted;
5. at $t = 30s$ a switch to the three-phase mode is triggered.

Fig. 4.8, 4.9, and 4.10 show the results of the simulation with the control scheme scheme described by Fig. 4.7. In particular from Fig. 4.9 we can see that the currents switch to the three-phase configuration almost instantaneously (less than one period). It is interesting to see how the voltages instead do not change too much between the two configurations: the most evident difference is a difference in amplitude between the two three-phase sets of the YY30 machine (v_{a1}, v_{b1}, v_{c1} have wider amplitude with respect to $v_{a2}, v_{b2}, v_{c,2}$). The HPD of the stator voltage references and of the obtained stator currents are shown in Fig. 4.10. Note that the 5-th harmonic plane voltage components generate the desired 5-th harmonic plane currents with a relative low voltage: this happens because the 5-th harmonic plane motor model presents a relative low impedance with respect to the fundamental. In Fig. 4.8 it can be seen that, as expected, when the machine is switched to the three-phase mode, efficiency decrease from 89.6% to 88.6% at steady state, which anyhow is not a huge difference. In Fig. 4.8 is not clear, but when the switch occur there is also a sudden little decrease in torque and speed, as shown in detail in Fig. 4.14a. This happens because the i^*_{d1} and i^*_{q1} references are suddenly decreased by the factor $K_{d,1} < 1$ and thus flux and torque production are affected. The speed control PI then kicks in and increase i^*_{q1} to bring back the speed to $900rpm$. This particular behaviour is not annoying in the simulations performed here, but in real life conditions with all the non-idealities and in case of machines with a lower value of $K_{d,1}$ could become problematic. Luckily it can be easily fixed: since the important aspect is the ratio between the amplitudes in the different harmonic planes, one solution is to keep the d_1q_1 references unmodified, while scaling the d_5q_5 by a factor equal to the ratio $K_{d,5}/K_{d,1}$. The new and improved

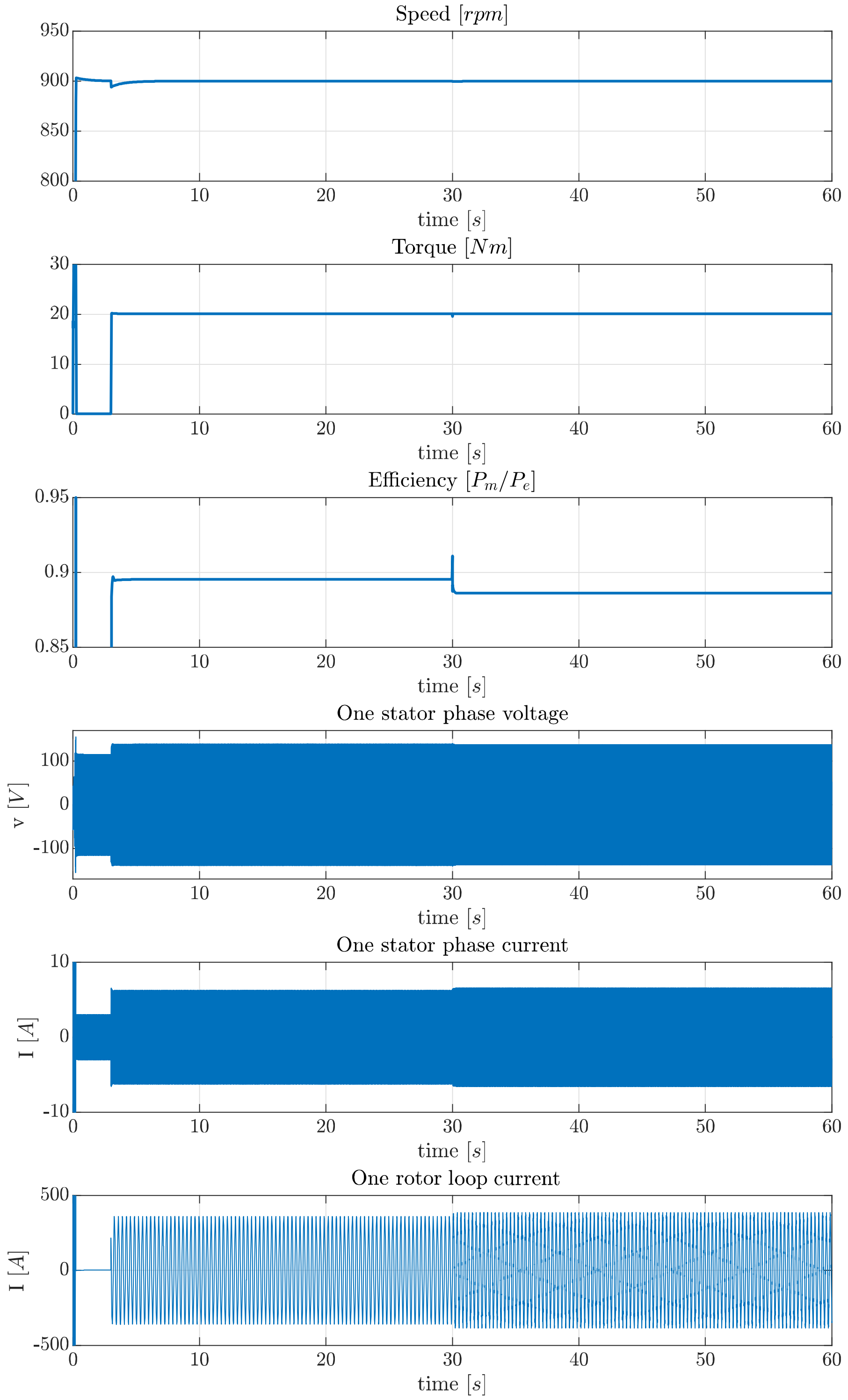

Figure 4.8: Simulation results (switch of configuration at $t = 30s$).

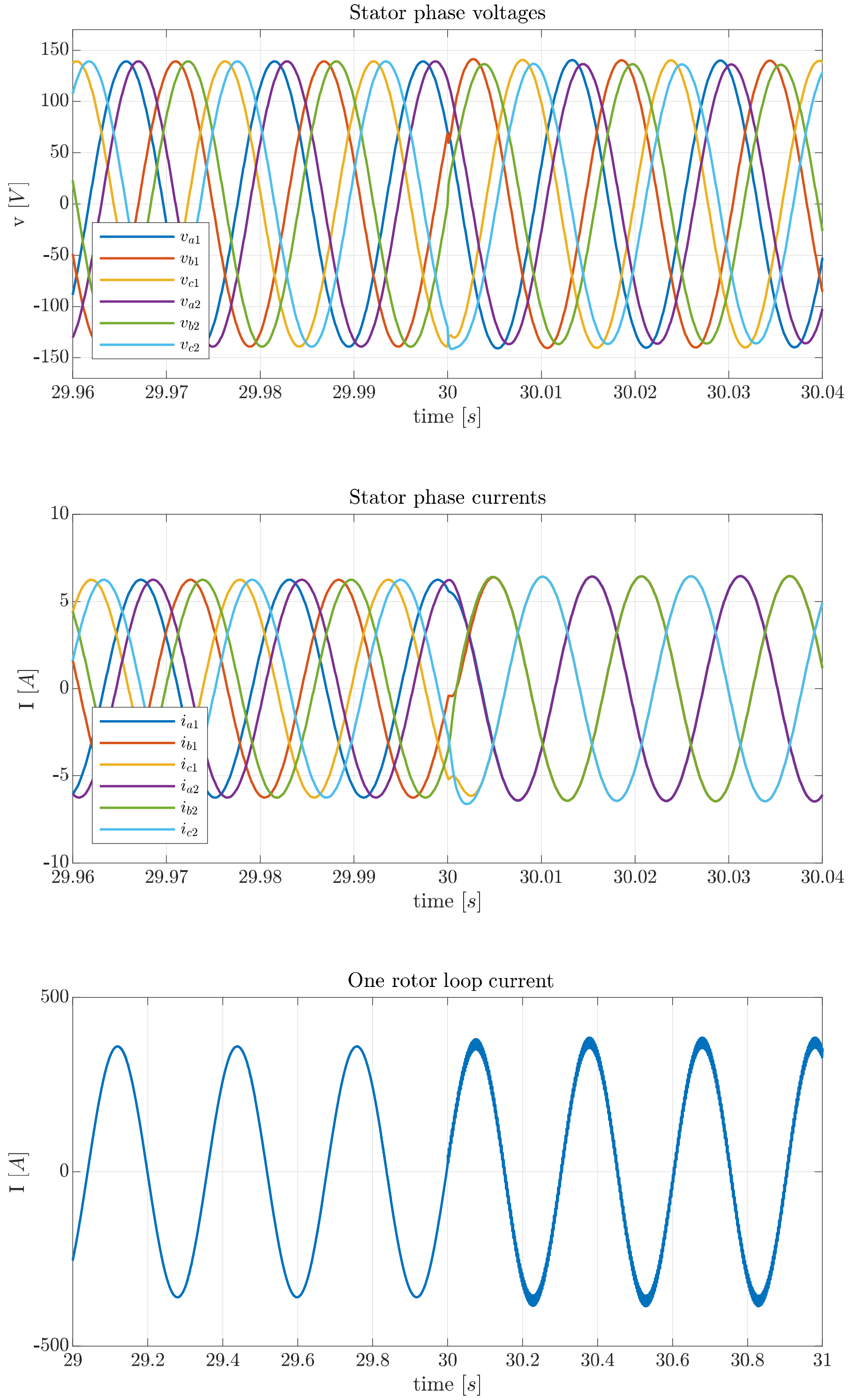

Figure 4.9: Simulation results (switch of configuration at $t = 30s$), details (beware of the different time-scale for the rotor).

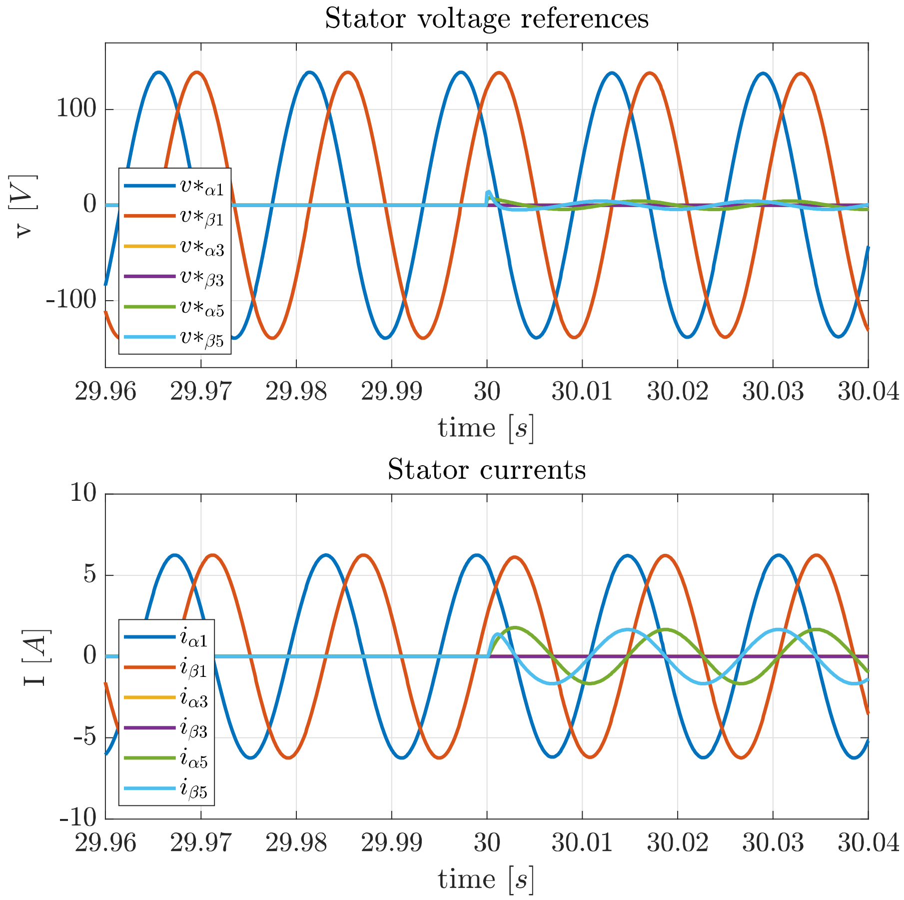

Figure 4.10: Simulation results: HPD of reference voltages and consequent stator currents.

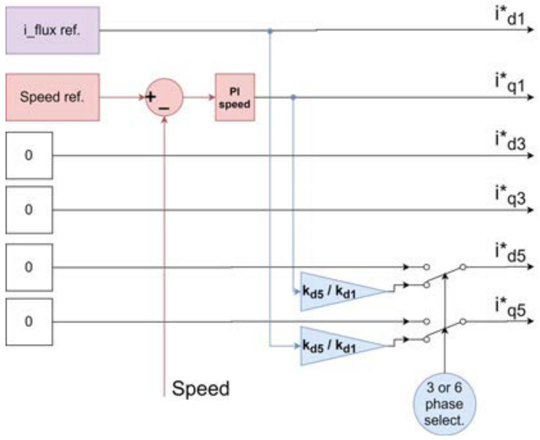

Figure 4.11: Improved control scheme, current references.

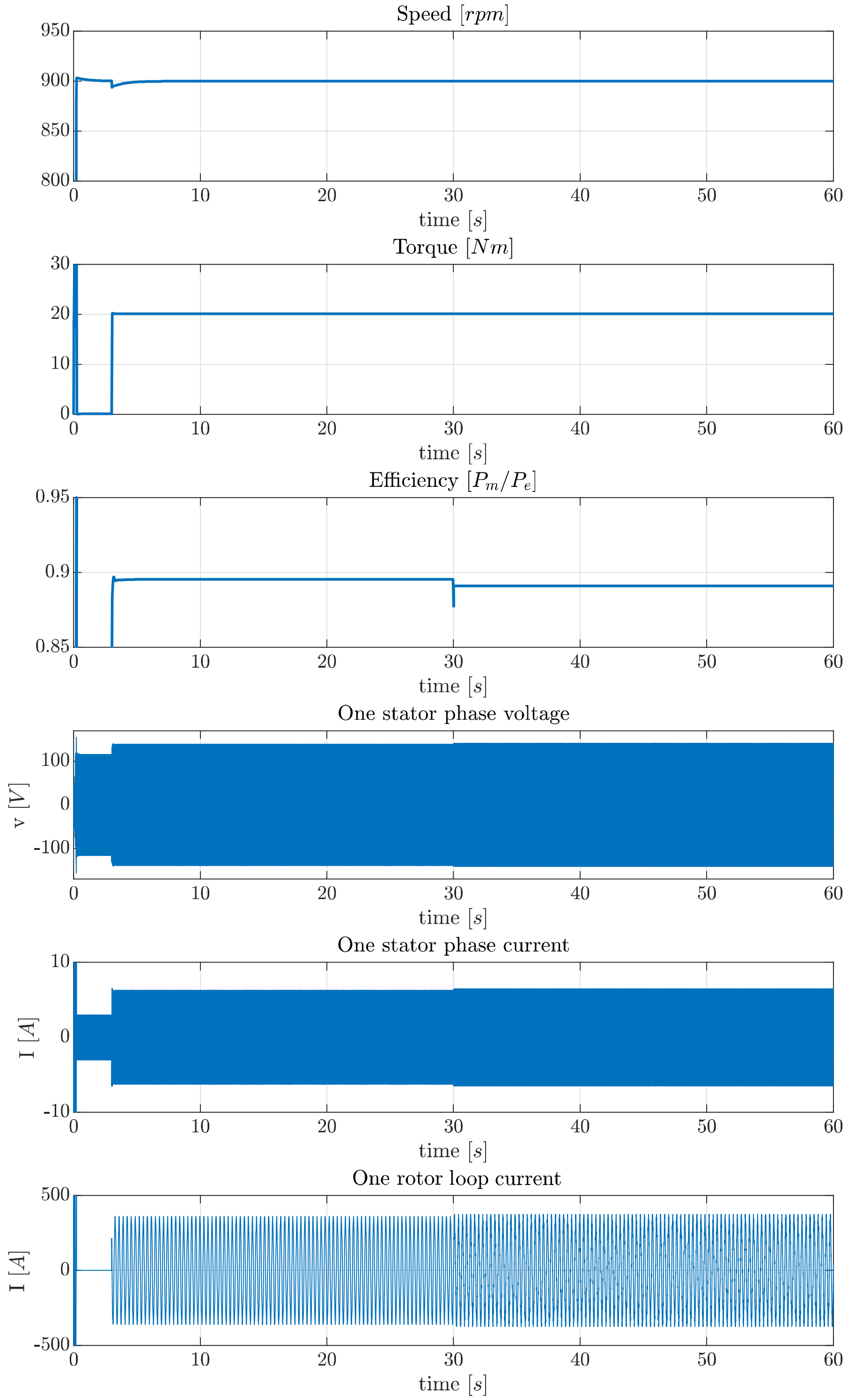

Figure 4.12: Simulation results with improved control scheme (switch of configuration at $t = 30s$).

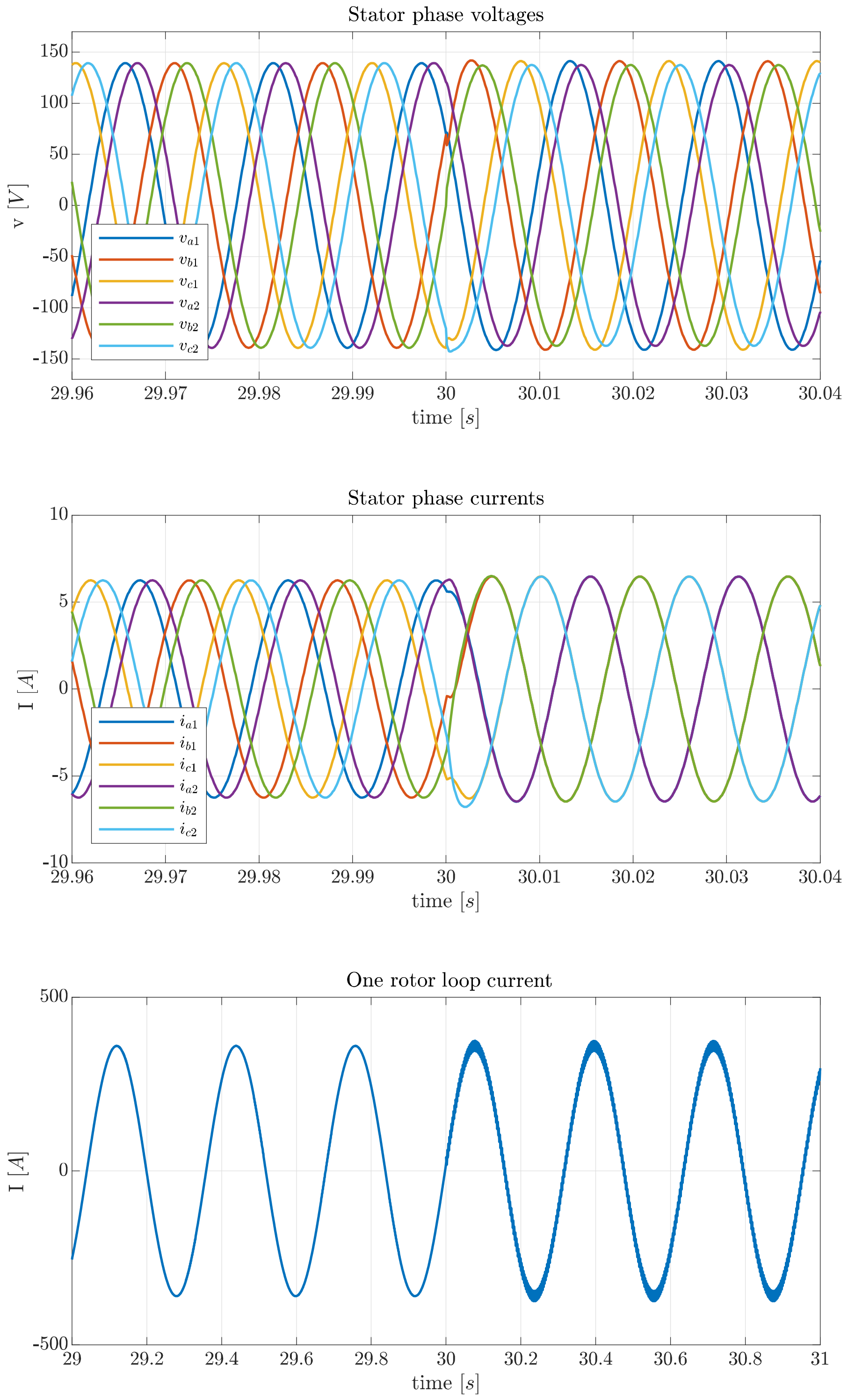

Figure 4.13: Simulation results with improved control scheme (switch of configuration at $t = 30s$), details (beware of the different timescale for the rotor).

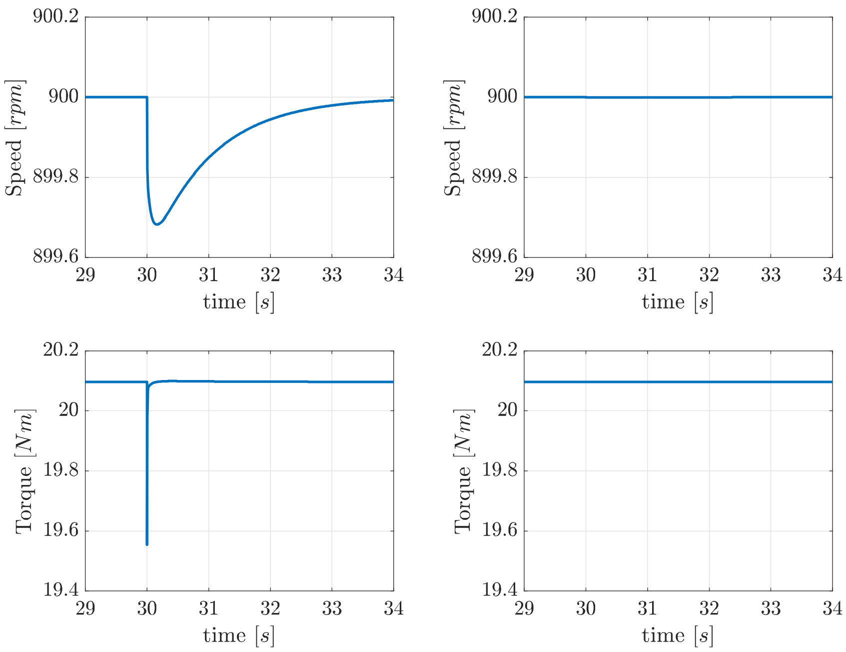

(a) With change of $d1$ and $q1$ references during the switch of configuration.

(b) With no change of $d1$ and $q1$ references during the switch of configuration (improved).

Figure 4.14: Comparison between two different control schemes, detail of speed and torque (switch of configuration at $t = 30s$).

scheme for the current references generation is shown in Fig. 4.11. The results of the simulations with the improved control scheme are shown in Fig. 4.12 and 4.13. The detail of speed and torque during the switch of configuration is shown in Fig. 4.14b: this time torque and speed seems to be not affected at all, and the passage is the smoothest possible. In addition also the efficiency benefits from the new control scheme, in fact at steady steady state in the three-phase mode it stands at 89.1% against the previous 88.6%. The explanation for this is that in the previous scheme the flux current reference was reduced by $K_{d,1}$, thus the machine was not exactly properly fluxed during the three-phase mode.

4.3.1 *Inclusion of dead-time effects*

In the simulations shown up to now, the "PWM+inverter" stage was modelled for the sake of simplicity just as a delay over the voltage references coming from the PIs. Thus, there were not any external source of harmonics to excite the 3-rd and 5-th harmonic planes in particular, making the control over them "useless" for the six-phase mode, while for the three-phase mode the 5-th harmonic plane was exploited for the necessary currents generation. Since the ripple introduced by the dead-time in PWM inverters can be a tricky aspect for MPMs in general,

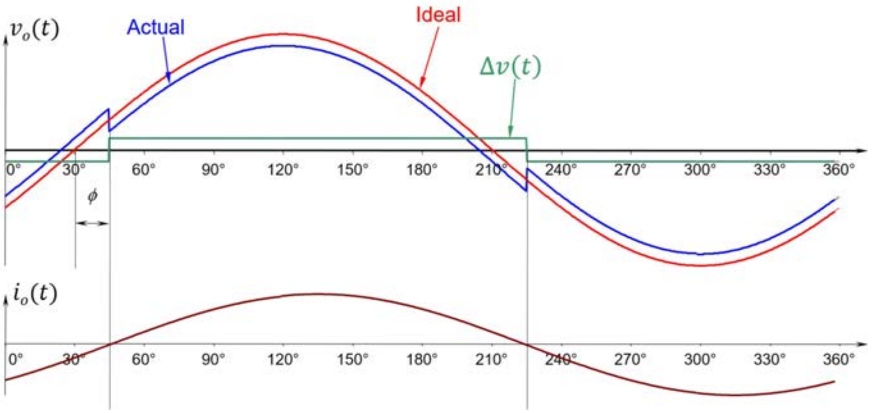

Figure 4.15: Dead-time effects on a leg voltage.

it may be interesting to see its effects on the developed control strategy. It is well known in literature that he actual pole voltage of j-th leg ($j = a_1, a_2, a_3, b_1, b_2, b_3$ in this case), v_j, can be evaluated on the basis of the reference pole voltage, v_j^*, according to the direction of the phase current i_j as:

$$v_j = v_j^* - sign(i_j)\Delta V_d \tag{4.14}$$

where ΔV_d is the averaged voltage contribution due to the dead-time t_d over the switching period T_s , $\Delta V_d = (t_d/T_s)V_{DC}$, [14]. It means that a square wave in phase with the leg current is subtracted from the ideal voltage, as shown in Fig. 4.15. This introduces all the low-order harmonics typical of a square wave. With sophisticated modulation techniques the dead-time effects could be mitigated, but they are not investigated in this work. To appreciate which could be the effects of these harmonics introduced by the inverter on this control strategy, the simple Eq. (4.14) has been implemented with $\Delta V_d = 5V$. The simulation results are shown in Fig. 4.16 and 4.17. In addition the HPD of the voltage references and stator currents during the switch of configuration are shown in Fig. 4.18. Note that 3-rd and 5-th harmonic plane components are not zero even in regular six-phase mode, since the controllers are trying to nullify the 3-rd and 5-th order time harmonics. The deformed voltages and currents generate a torque with some high frequency ripple, and that in three-phase mode this ripple increase in amplitude, since the 5-th harmonic control plane is used to generate the negative sequence currents at fundamental frequency, and do not mitigate anymore the 5-th order time harmonic in the phase currents. It is interesting to have a look at the FFT of one of the stator currents in steady state, shown in Fig. 4.19b for the six-phase mode, and in Fig. 4.19c for the three-phase mode. In the regular six-phase mode it can be seen how the PIs in the rotating reference frames cancel selectively the 3-rd and 5-th order time harmonics, which would be the most important ones, and cannot do much for the higher order

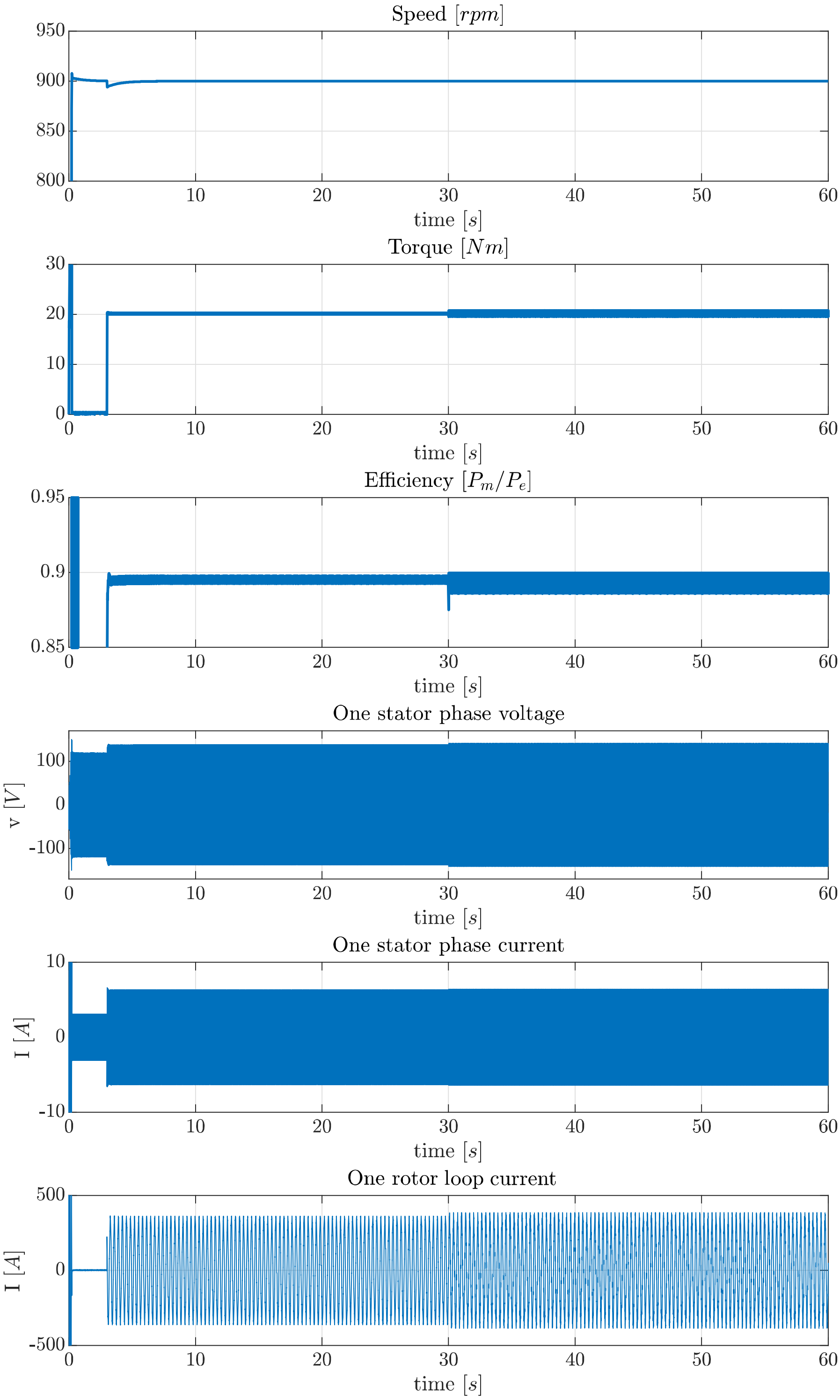

Figure 4.16: Simulation results with dead-time effects (switch of configuration at $t = 30s$).

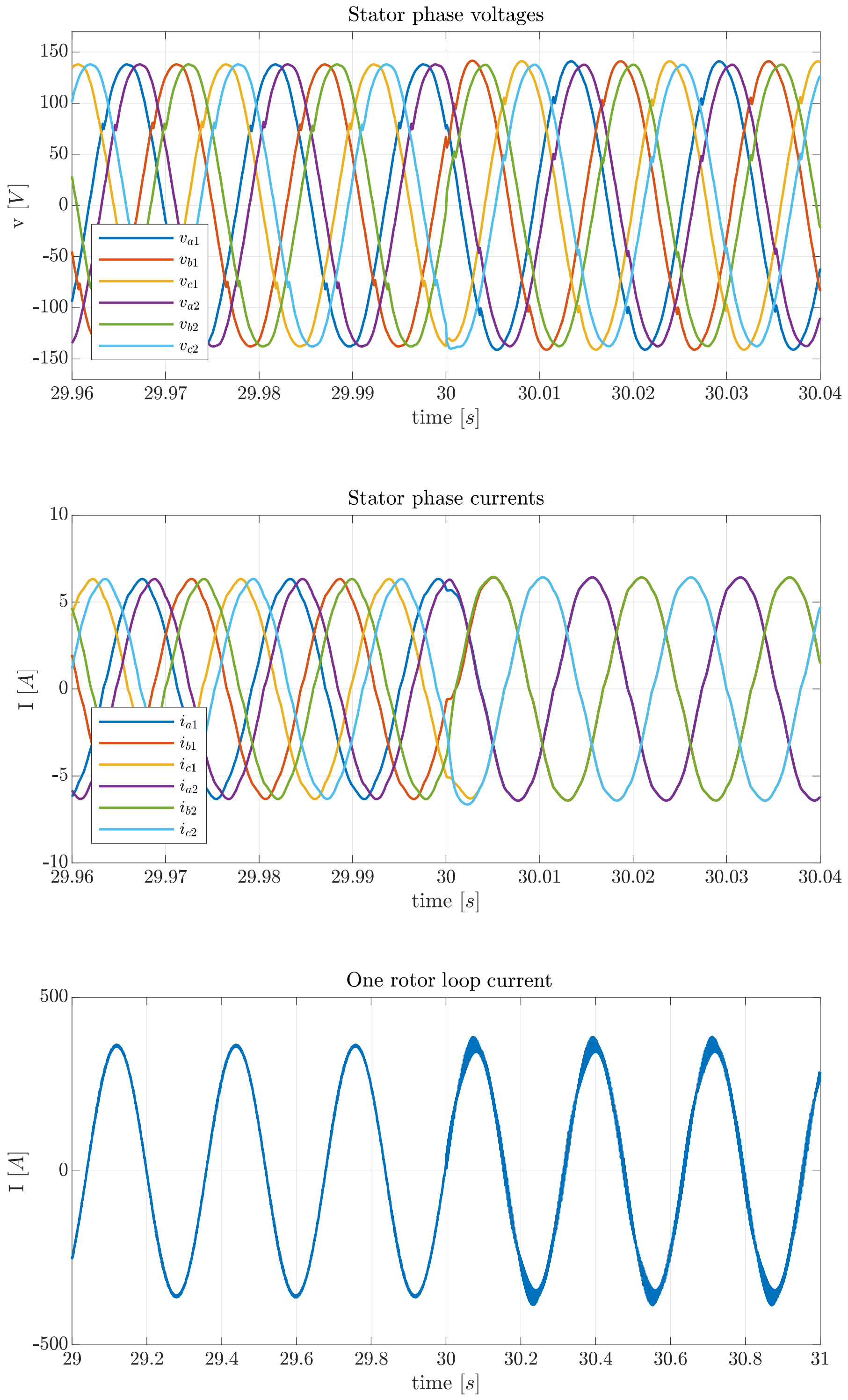

Figure 4.17: Simulation results with dead-time effects (switch of configuration at $t = 30s$), details (beware of the different time-scale for the rotor).

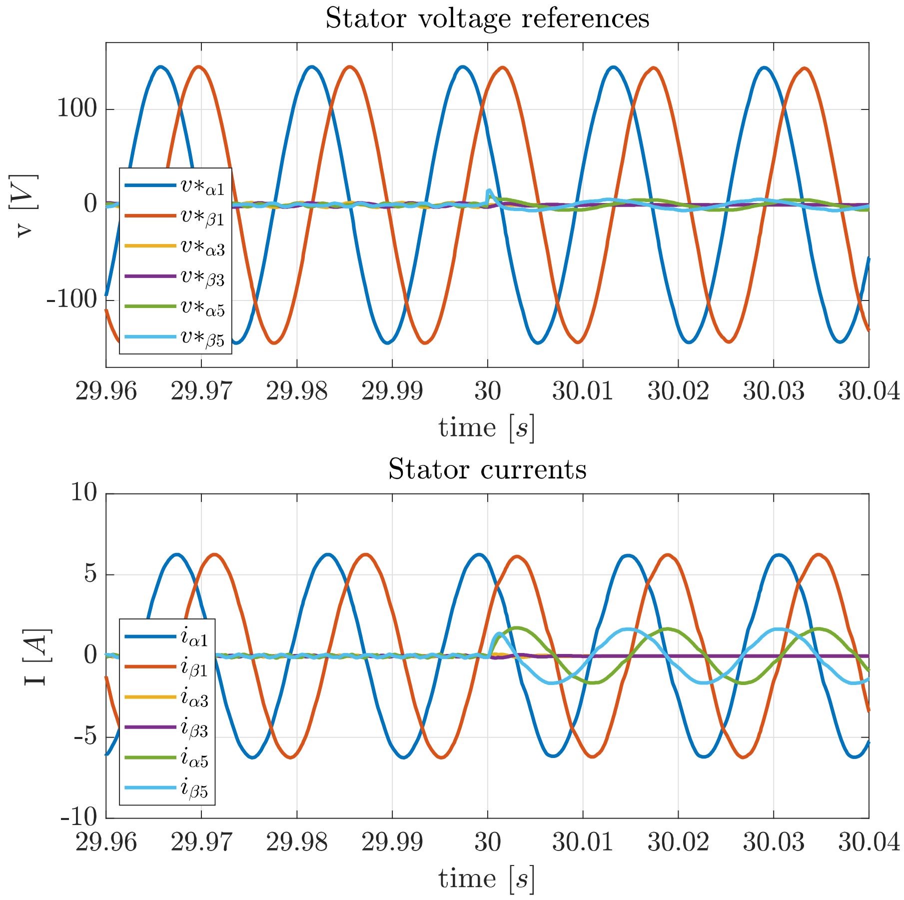

Figure 4.18: Simulation results with dead-time effects: HPD of reference voltages and consequent stator currents.

time harmonics. In the three-phase mode, all the triplen harmonics are not present like in normal three-phase machines because the neutral point is isolated, but the 5-th order time harmonic is present, and since it is quite a big one, the Total Harmonic Distortion (THD) is worse with respect to the six-phase case. Anyhow in both cases the situation is fairly better than in the case only fundamental harmonic plane is controlled while the others are left in open-loop. The FFT of this case (of course in six-phase mode, the only possible with open loop control over the 5-th harmonic plane) is shown for comparison in Fig. 4.19a. In those scenarios where the dead-time effects result problematic there may be the need to adapt some compensating technique.

4.4 CONCLUSIONS OF PART I AND FUTURE DEVELOPMENTS

In this first part we have seen how multiphase IMs are usually modelled and driven, in particular, thanks to the VSD. Unfortunately this technique was not suitable to develop a control strategy capable of dealing with the phase/pole changing capabilities of the WICSC prototype. Then, we have presented HPD, and showed how it should be

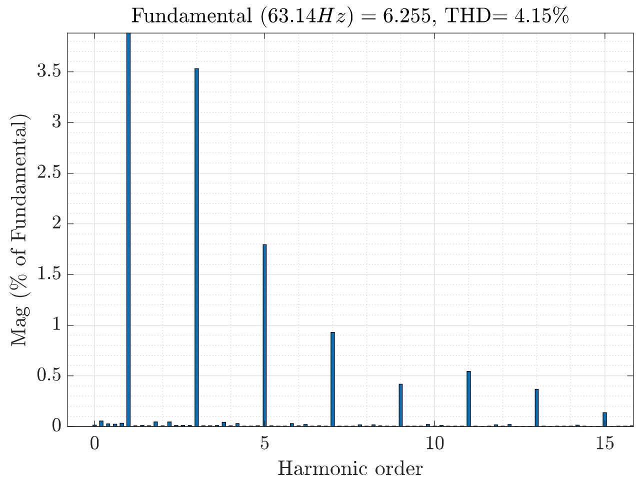

(a) Six-phase mode with open-loop control on the the 3-th and 5-th harmonic plane.

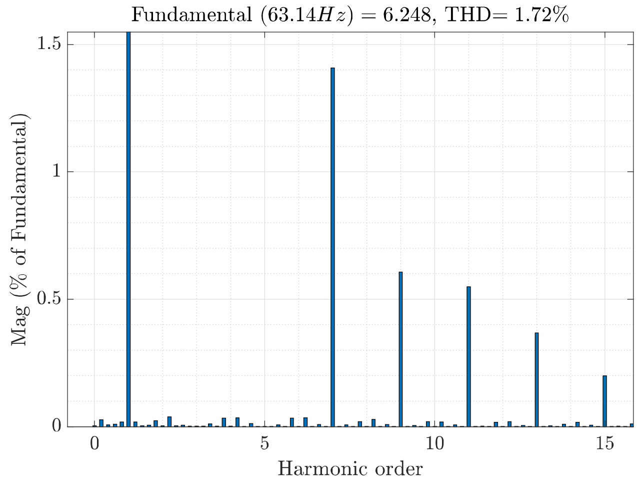

(b) Six-phase mode with closed-loop control on the the 3-th and 5-th harmonic plane.

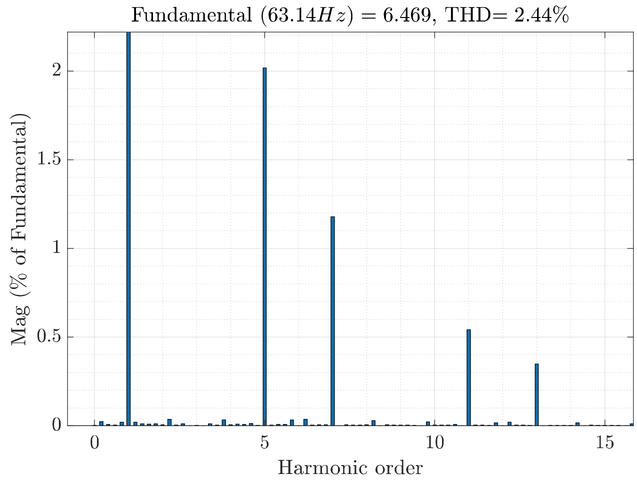

(c) Three-phase mode.

Figure 4.19: FFT of a stator phase current.

possible to build a control strategy capable of dealing with the different configurations of a WICSC machine. We tested the phase changing capabilities on a regular YY30 six-phase machine. The next step in order to build a complete control strategy for the prototype is to test the pole-changing capabilities, which is somehow more important. In fact from a performance point of view the best solution should be to run the machine with the highest number of phases for the number of pole pairs that better suits the torque/speed demands. Change the number of phases only can be interesting from a research point of view, but probably the approach used in this work is not the best to compare machines with different number of phases with the same geometry. In fact we have seen in the simulations that the voltages are actually really similar to the ones of the configuration with the highest number of phases. For this purpose probably it would be better to just physically connect the stator coils in order to create the desired configuration and test it individually. Anyhow the work done was a necessary step for a better comprehension of MPMs in general and WICSC machine in particular, and to build an adequate and solid control strategy. We have seen how to exploit the harmonic planes to reproduce a configuration with a different number of virtual phases, and that this comes at a price, which is a higher complexity due to multiple references in different planes, and the need for dead-time effects compensating techniques in those cases where the harmonic content could reach unacceptable levels. Even from the simulations of a regular MPM, we have seen that setting zero as a reference of controllers in a rotating reference frame eliminates the first odd time-harmonics up to n very selectively, which is not bad since they are the most important, but probably also other approaches that take action also on higher order harmonics should be considered for better performance. Once the pole-changing control will be tested and proved functional, another key aspect will have to be considered, which is the fact that the base-case selected for the protype is made of virtual phases as well, and there will be 36 measured currents but only 18 PI controllers (two for each harmonic plane). One possible solution is to use the current of the first 18 slots to close the loops of the $18-$phase base-case control strategy, and then have the next 18 slot currents to close the loops of a mirror $18-$phase base-case control, which outputs and control opposite currents. This way the total of 36 PIs would employ all the degrees of freedom given by the 36 inverter legs. Finally, it is to be said that other control strategies are possible. For example the ISCAD machine is controlled so that the current in the j-th stator slot has the form $i_{s,j} = \hat{I}\cos\left(\omega t - (j-1)(2\pi/Q_s/p)\right)$, [13], and probably $\hat{I}$ is determined by a V/f control. The equivalent number of phases could even result to be fractional, because the focus is on the number of poles of the generated magnetic field. This control strategy looks much more straightforward, but it does not take into accounts any time-harmonic at all, and in MPMs this aspects can eventually reveal to be one of the trickiest.

Part II

SIGNAL CONDITIONING BOARD PROJECT

The second part of the thesis deals with the project of three signal conditioning boards that will be part of the test-bench of the WICSC machine prototype at KTH laboratories. The boards feature anti-aliasing filters, signal conversion from single-ended to differential, output voltage clamping, and fault signals management. Chapter 5 gives an outline of the WICSC test-bench and introduces the aliasing problem. Chapter 6 shows the main parts of the electrical circuits to be implemented in the board. In Chapter 7 some stability analyses are performed, and finally Chapter 8 showcase the final Printed Circuit Board (PCB) design of the boards.

5

INTRODUCTION

In order to drive and test the WICSC prototype, we need to set up a customized and complete system. Some physical quantities need to be measured and then processed by the control algorithm, and ultimately drive control signals need to be generated. Below there's an overview of the test bench configuration that will be used at KTH laboratories.

5.1 TEST-BENCH CONFIGURATION

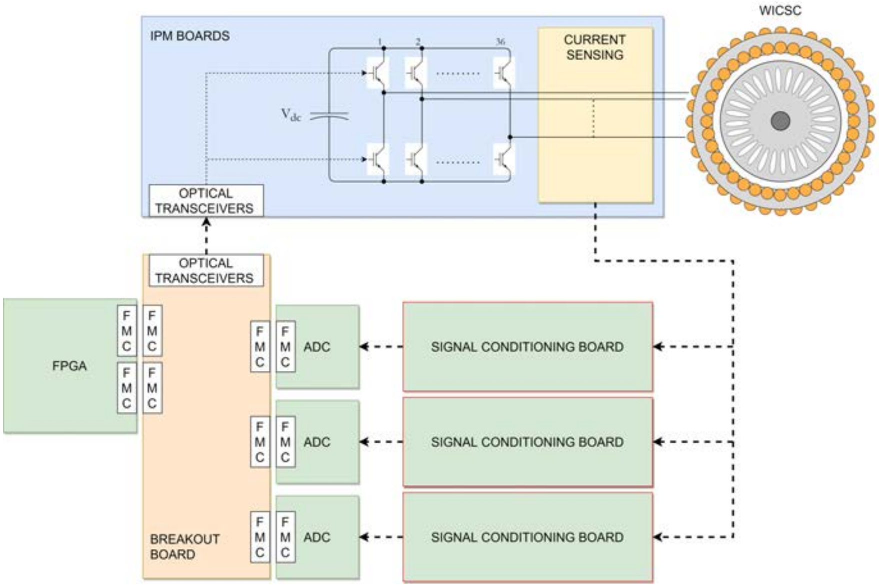

Figure 5.1: Schematic representation of the test-bench configuration for the WICSC prototype.

Fig 5.1 shows a schematic representation of how the test-bench should look like once all of its components are configured and ready to use. The WICSC prototype is supplied by a 36-legs inverter connected, as already mentioned in the previous part of this work, to one of the terminals of each stator coil. The converter itself consists of twelve Intelligent Power Modules (IPMs), with three legs each (with IGBTs) and one DC-bus capacitor each. In the IPM, shown in Fig. 5.2, find place three current sensors (one per leg output) and one DC-bus voltage transducer. All of these signals are sent to three signal conditioning boards, which adapt the values to match the ADC requirements. Then the three ADCs send the digitalized measurements to a Field Programmable Gate Array (FPGA) (the Xilinx Zynq-7000 ZC702). Here the signals are elaborated, together with the other external inputs

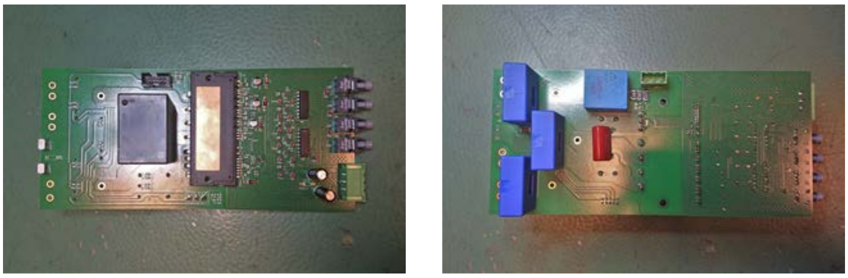

(a) IPM front. (b) IPM back.

Figure 5.2: IPM pictures.

and requests, and the IGBT's gates commands are generated according to the chosen modulation technique. The signals are sent to the IPMs through an optical interface. In between the ADCs, the FPGA, and the IPMs, a breakout board untangles the signals coming and going through FPGA Mezzanine Card (FMC) connectors and manages the optic interface.

The realization of such a type of system requires knowledge in many different fields: electrical machine design, electric drive techniques, electronic design, firmware programming (the control algorithm will be implemented in the Zynq's built-in processor), and hardware description languages (like the VHDL) for the realization of dedicated hardware in the FPGA. This work deals with the project of the three signals conditioning boards, highlighted in red in Fig. 5.1. The main task of these boards, which deal with a total of 36 current measurement channels and 12 voltage measured angle channels, is to accommodate anti-aliasing filters.

5.2 THE ALIASING PHENOMENON

In signal processing, aliasing is an effect that causes different signals to become indistinguishable (or aliases of one another) when sampled. In Fig. 5.3 it is shown the case of a signal whose spectrum has a bandwidth limited between $\pm\omega_{max}$. The spectrum of the sampled signal presents copies centred at the multiples of the sampling angular frequency Ω. The half of the sampling angular frequency is known as the Nyquist angular frequency $\Omega_N = \Omega/2$. For $\omega_{max} < \Omega_N$ the spectrum components of the sampled signal are separate, and theoretically it is possible to reconstruct the original time continuos signal with an ideal low pass filter with a unitary gain inside $\pm\Omega_N$ and null outside. If $\omega_{max} > \Omega_N$ the components of the sampled signal overlap and it is not possible (not even theoretically) to extract the original spectrum. This phenomenon is known as *aliasing* or *frequency folding*, and it is always present in the sampling of real signals. The components of the original spectrum with angular frequency above Ω_N contribute

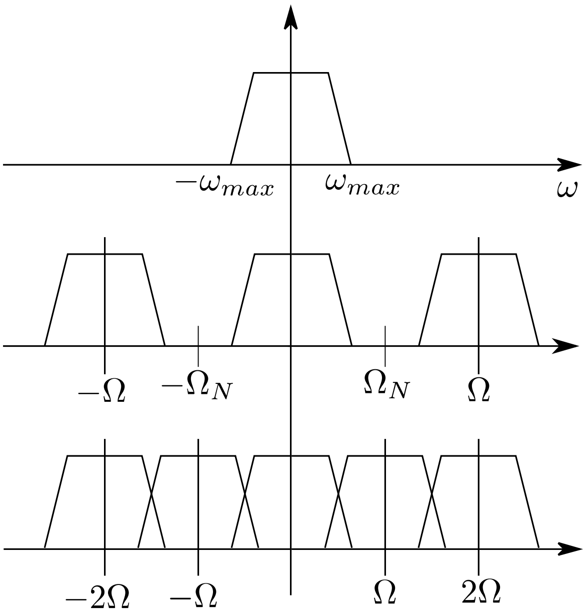

Figure 5.3: Sampling effects.

to form the spectrum of the sampled signal in the region of $\omega < \Omega_N$. To avoid this issue is necessary to precede the ADC that samples the signal with a low pass filter called anti-aliasing filter. That filtering process, because it happens in the analogue world, requires real analogue hardware: circuits made of resistors, capacitors, and amplifiers. The task is to eliminate or at least heavily attenuate all the components of the signal to be sampled above $\Omega/2$. The filter can introduce a shifting that influences the stability and the dynamic behaviour of the overall system.

6

ELECTRICAL CIRCUITS SCHEMES

In this chapter are shown the basic circuits that need to be implemented in the signal conditioning boards and some particular design choices are explained.

6.1 MEASURING RESISTANCE

Before the filter stage, the signal coming from the current and voltage transducer needs to be converted into a voltage signal. In fact both the sensors, the LEM LA 100-P current transducer (datasheet [4]), shown in Fig. 6.1a, and the LEM LV 25-P/SP5 voltage transducer (datasheet [35]), output a current proportional to the measured value. To get a voltage signal a very simple approach has been used: a simple high precision measuring resistance R_m generates a voltage drop when the current coming from the secondary circuits of the transducer I_s flow through it, as shown in Fig. 6.2. In this case, following also the indications of the datasheets, a 44.2Ω resistor was chosen for the

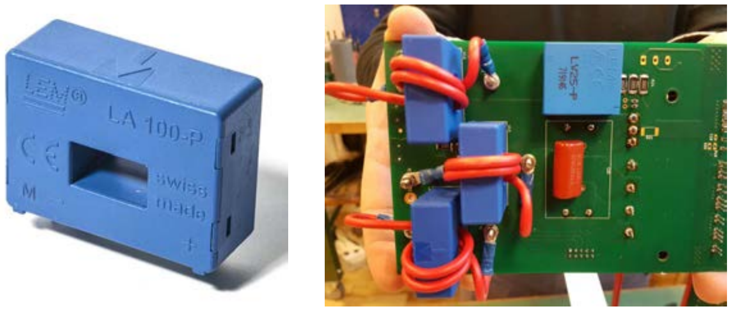

(a) LEM la-100p current transducer.

(b) Winding of a leg output conductor on the LEM la-100p.

Figure 6.1: Implementation of the current transducer

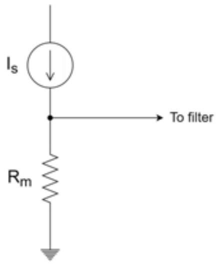

Figure 6.2: Measuring resistance circuit.

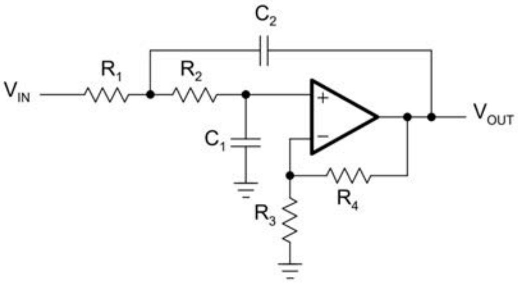

Figure 6.3: General Sallen-key low-pass filter.

current measurement channels, and a 100Ω resistor was chosen for the voltage measurement channels.

6.2 ANTI-ALIASING FILTERS

For the project of the anti-aliasing filters, the design references available in [2, 16, 23] have been followed. The final design has been determined with the help also of Texas Instruments' filter design tool* and then simulated on a SPICE circuit simulator (Tina-TI by Texas Instruments in this case). The choice has been a second-order Butterworth low-pass filter (characterized by a frequency scaling factor $FSF = 1$ and a quality factor $Q = 0.707$) with Sallen-Key architecture. The Butterworth low-pass is often used as anti-aliasing filter in data converter applications where precise signal levels are required across the entire passband because it provides maximum passband flatness. A second-order low pass filter has two possible topologies, i.e. the Sallen-Key, shown in Fig. 6.3 and the Multiple Feedback topology. The latter inverts the input and is usually used with high gain values, which is not the case, and this is why the first has been preferred. Referring to Fig. 6.3 the gain K, the quality factor Q, and the corner frequency f_c (breakpoint between the passband and stop band, and is not necessarily the $-3dB$ point) are given by the following expressions:

$$K = 1 + \frac{R4}{R3}, \tag{6.1}$$

$$Q = \frac{\sqrt{R1R2C1C2}}{R1C1 + R2C1 + R1C2(1-K)}, \tag{6.2}$$

$$f_c = \frac{1}{2\pi\sqrt{R1R2C1C2}}. \tag{6.3}$$

The final antialiasing filters for the currents measurement channels and the voltage measurements channels respectively are shown in Fig. 6.4 and 6.5. To study the circuits the measuring resistance has been replaced by a voltage signal generator, with the assumption that all the current flowing from the transducers passes through Rm.

---

* Available at `https://webench.ti.com/filter-design-tool/filter-type`

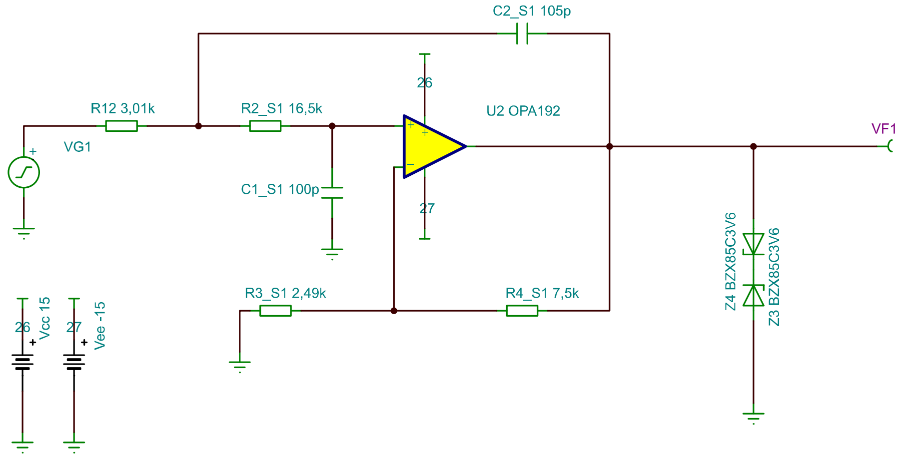

Figure 6.4: Anti-aliasing filter scheme of one current measurement channel.

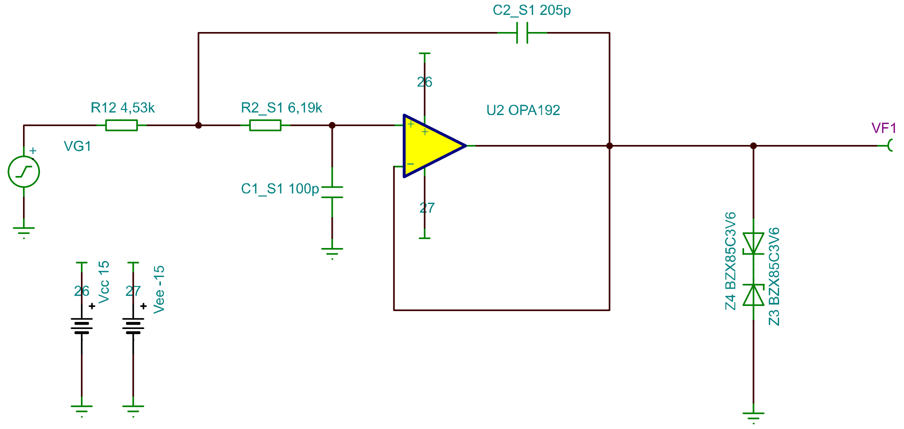

Figure 6.5: Anti-aliasing filter scheme of one voltage measurement channel.

For the current measurement channels it has been set a gain of 4, whereas for the voltage measurement channels a unitary gain is used. Gains have to do with the ranges of current/voltages that one wants to be able to measure. This aspect will be discussed later in this Chapter. Both the configurations present a corner frequency around $200kHz$. The Nyquist frequency will actually be in the order of some MHz but, since $200kHz$ is also the bandwidth of the LEM transducer, everything above that frequency would be just noise. The operational amplifier used in the board is the low input bias current, 4 channels, OPA4192 (datasheet [25]), supplied with $\pm 15V$, which were voltage levels already present in the system's power supply since they're used also from the IPMs.

6.3 SINGLE-ENDED TO DIFFERENTIAL SIGNAL CONVERSION

Even though the main task of the board looks accomplished with the filters that have just been presented, a compatibility issue with the

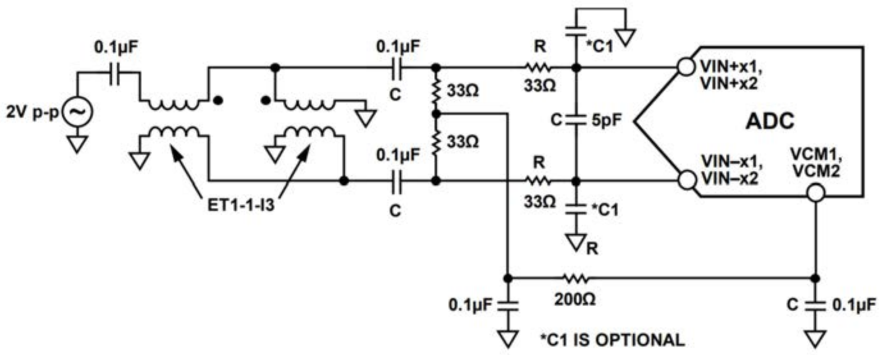

Figure 6.6: Differential double balun input configuration for baseband applications, [1]

purchased ADC, made it necessary to implement also a conversion of the signal from single-ended to differential.

6.3.1 *ADC compability issues*

The ADC board chosen for the test-bench of the WICSC prototype is the AD9249-65EBZ (datasheet [1]), a 16 channels, 14 bit, $65M$ samples per second, ADC evaluation board from Analog Devices Inc. Each of the 16 channels has a BNC connector to input the signal to be sampled as a single-ended signal. The ADC itself, however, needs to be driven with differential inputs. The conversion takes place in the analog front-end of each channel, and in these circuits is where who is writing realized that unfortunately there was quite a significant compatibility issue. The analog front-end of a channel is shown in Fig. 6.6. The $0.1\mu F$ immediately stands out, blocking DC components. Then there are two balun transformers that generate the differential signals, and finally the common mode voltage of $1V$ (coming from the ADC itself that integrates the voltage reference) is superimposed to both the signals. If all the analog front-end input configuration is reproduced in Tina-TI, the Bode diagrams of the AC transfer characteristics that you get are shown in Fig. 6.7. It is clearly a high-pass filter with a $-3dB$ cutoff frequency around $73kHz$, and that reaches no attenuation at all above $300kHz$. This is of course in sharp contrast with our target of sampling the signal coming from the anti-aliasing filter. Nevertheless, the AD9249-65EBZ suggested application reported in its datasheet is in communications receivers, and in general it is meant to sample high frequency signals in the range of MHz. Thus, it has not been a wise choice. To make it work, some tricky modifications need to be done. All the involved components are shown in the schematic of the first analog front end in Fig. 6.8. In particular, the two balun transformers (T402A and T403A) need to be removed, and shorting the two capacitors C404A and C405A the differential signals can be directly connected soldering wires in the big pads of the not-installed

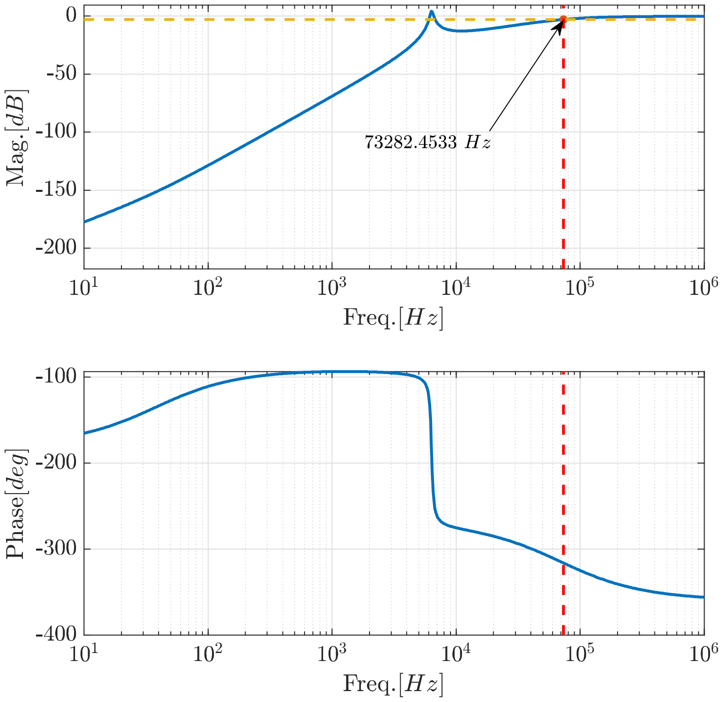

Figure 6.7: AC transfer characteristics, input configuration of the AD9249-65EBZ.

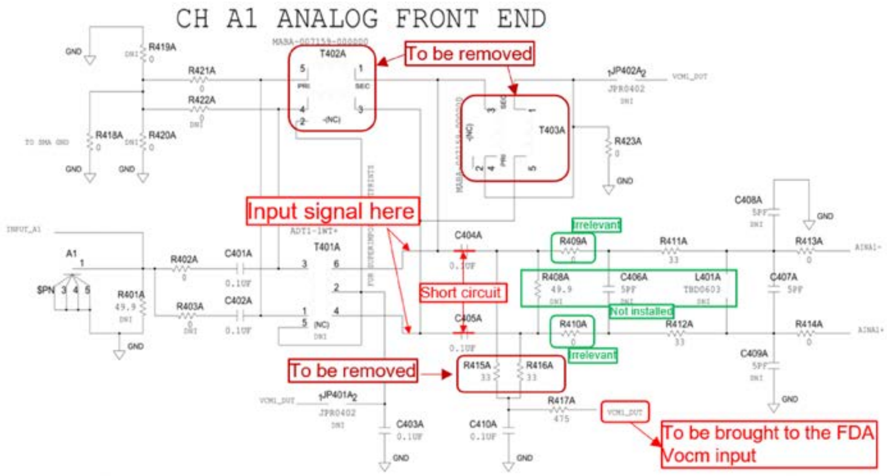

Figure 6.8: Modifications to be done on the analog-front end of the AD9249-65EBZ.

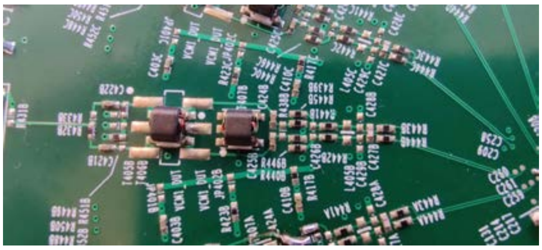

(a) Before

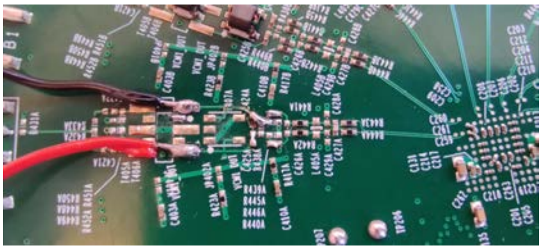

(b) After

Figure 6.9: AD9249-65EBZ before and after the required modifications

T401A component. The result of this operation is shown in Fig. 6.9. Of course, this new configuration requires a differential signal at the inputs, thus a conversion from single-ended to differential of the signals had to be implemented in the signal conditioning boards.

6.3.2 *ADC input requirements*

Before jumping to how the conversion has been implemented let's take a look at the AD9249 input requirements, shown in Fig. 6.10. Each one of the two input signals V_{in+} and V_{in-} has absolute maximum ratings as low as $-0.3V$ and as high as $2V$. The common mode voltage should range between $0.5V$ and $1.3V$. The differential signal has a specification of $2V_{pp}$ peak-to-peak in order for the ADC to work properly, thus, if it is set a common mode voltage of $1V$, both V_{in+} and V_{in-} should range between $0.5V$ and $1.5V$, even if the absolute maximum ratings are much wider. The interpretation given is that if the input signals present a wider range, the differential signal goes out of specification and the sampled output becomes less reliable, but nothing risk breaking until the absolute maximum ratings are reached.

6.3.3 *Conversion implementation with FDA*

Following the guidelines in [17, 31], a circuit like the one shown in Fig. 6.11 has been implemented. It makes use of an FDA in order to generate the differential signal. In particular, the choice fell on the 4 channels THS4524-ep (datasheet [32]), implemented with a single-side supply at $+5V$. Again, a $+5V$ power supply was already present

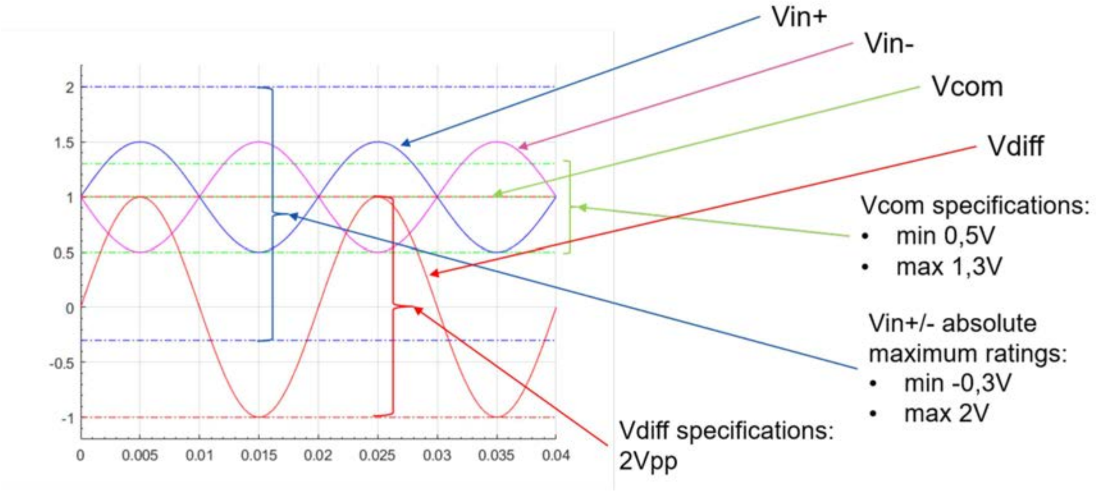

Figure 6.10: AD9249 input requirements

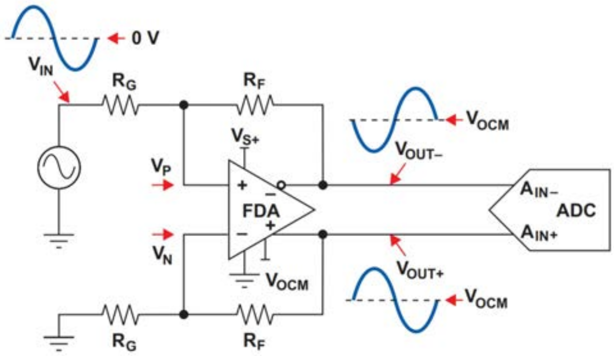

Figure 6.11: Single-ended bipolar input circuit, [17].

in the system for other purposes. Referring to Fig. 6.11 the gain is set by R_F/R_G. In the final design, the gain has been set to $1/4$ because the single-ended input signal is limited to $\pm 4.35V$ by the two opposing Zener shown at the output of the filter in Fig. 6.4 and 6.5. The waveform is limited to the Zener voltage ($3.6V$) plus the forward voltage ($0.75V$) on both polarities, and with the gain of $1/4$ in the new stage, the differential input signal of the ADC has a range of $\pm 1.075V$, and with a common mode voltage imposed by the FDA of around $1V$, both the V_{in+} and the V_{in-} signals comply with the requirements. The differential signal can slightly go out of specifications, but it is limited soon after, and way before the V_{in+} and the V_{in-} signals go above the absolute maximum ratings. The $1V$ common mode voltage reference is taken from the AD9249-65EBZ voltage reference and brought to the signal conditioning boards with wires. In each board, it is buffered using the operational amplifier OPA350 (datasheet [26]), to prevent any current flowing into the AD9249-65EBZ voltage reference pin, since this could happen due to the internal structure of the FDA and its potential effects are not mentioned in the AD9249 datasheet.

6.4 FINAL CONFIGURATION OF CURRENT AND VOLTAGE MEASUREMENT CHANNELS

The final configuration of a current measurement and voltage measurement channel are shown in Fig. 6.14 and 6.14 respectively. They differ only in the anti-aliasing filter stage.

6.4.1 *Ranges*

The current measurement channel has been projected to measure currents up to $10.6A$ rms, i.e. instantaneous values in the range of $\pm 15V$. In fact, going backwards from the ADC $2V_{pp}$ specification for the differential signal, it corresponds to a $\pm 1V$ signal at the input of the filter stage (gain of 4 in the filter stage and of $1/4$ in the single-ended to differential stage have a net unitary gain), which on the 44.2Ω measuring resistor corresponds to $\pm 22.6mA$. Since the ratio in the current transducer is of $1 : 2000$, in the primary circuit at the limits of the ADC specifications we find $\pm 45.24A$, which is around the aforementioned $\pm 15A$ in the WICSC coil, because the primary circuit is wound with three turns as shown in Fig. 6.1b. For the outputs of a current measurement channel of the signal conditioning boards, when the input of the filter stage is a $1V$ amplitude, $50Hz$, sine wave, corresponding to a $15A$ amplitude, $50Hz$, sine wave current flowing on the coil, see Fig. 6.12. Fig. 6.13 shows instead a case above the limits, with the input of the filter stage set as a $2V$ amplitude, $50Hz$, sine wave, corresponding to a $30A$ amplitude, $50Hz$, sine wave current flowing on the coil. In this case, we can appreciate the intervention of the Zener diodes to protect the ADC inputs.

The voltage measurement channel instead has been projected to measure DC-bus voltages up to $+(-)960V$. In fact, again going backwards from the ADC $2V_{pp}$ specification for the differential signal, it corresponds to a $\pm 4V$ signal at the input of the filter stage (unitary gain in the filter stage and of $1/4$ in the single-ended to differential stage make for an overall signal conditioning path gain of $1/4$), which on the 100Ω measuring resistor corresponds to $+(-)40mA$. Since the ratio in the voltage transducer is of $2500 : 1000$, in the primary circuit at the limits of the ADC specifications we find $+(-)16mA$, which is the current flowing through a $60k\Omega$ resistor installed on the IPM board across the DC-bus. Thus, it corresponds to the aforementioned $+(-)960V$. Fig. 6.12 and 6.13 can be obtained almost identical for the voltage measurement channel with a sine wave input at the filter stage with 4 times the amplitude, but actually, this channel will measure only positive and DC values.

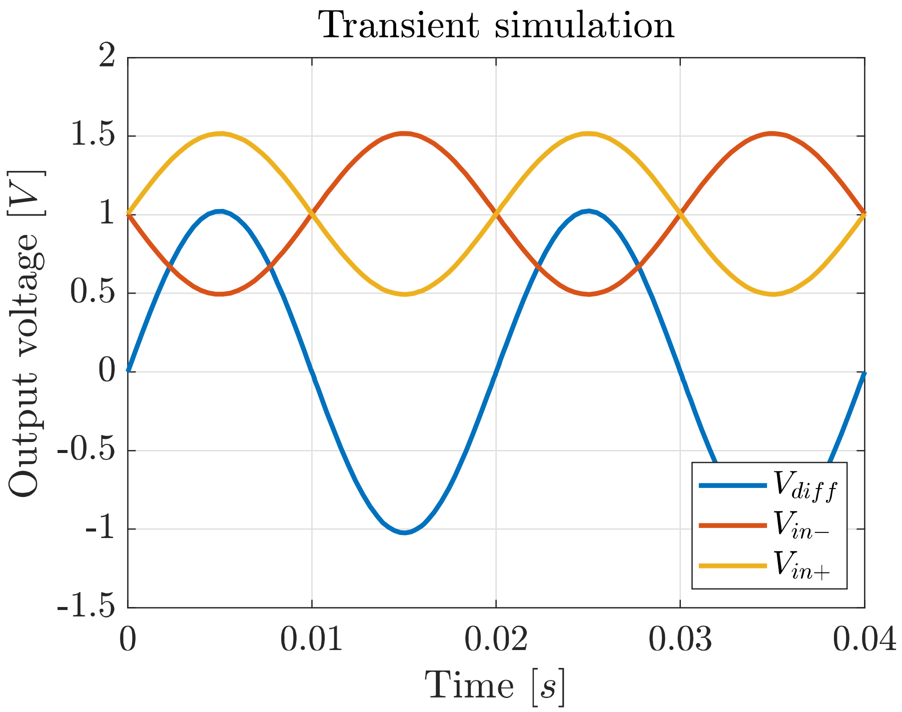

Figure 6.12: Transient simulation of the current measurement channel outputs, when the input is a $1V$ amplitude, $50Hz$, sine wave.

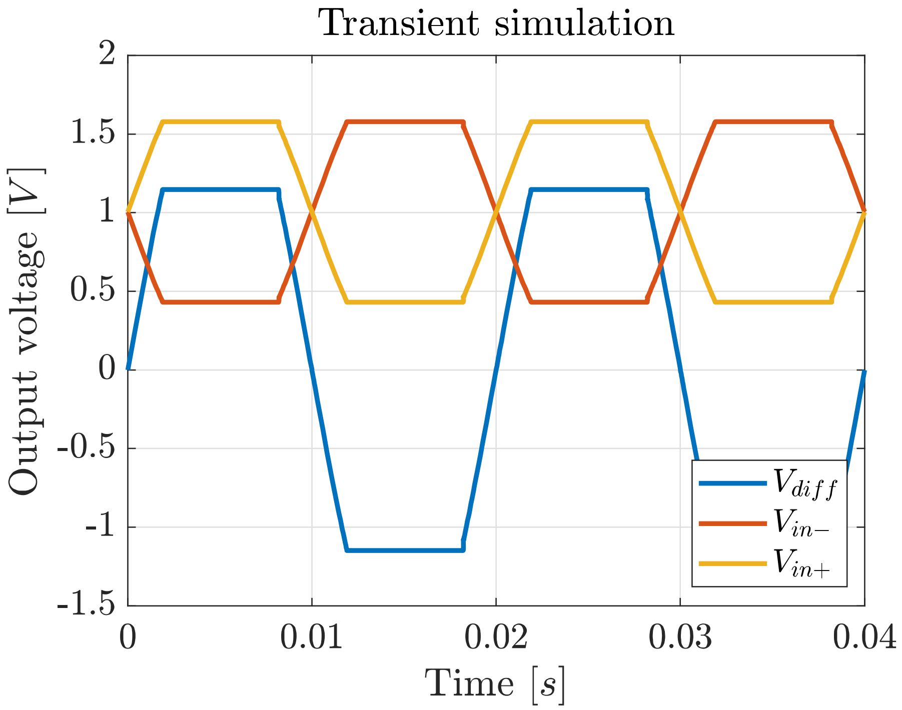

Figure 6.13: Transient simulation of the current measurement channel outputs, when the input is a $2V$ amplitude, $50Hz$, sine wave.

6.4.2 *Frequency response*

The frequency response of the current measuring and voltage measuring channels as a whole (as in Fig. 6.14 and 6.15) are reported in Fig. 6.16 and 6.17 respectively, with the $-3db$ highlighted (which for the voltage measurement channel is found actually at $-15dB$ due to the overall gain of $1/4$ that corresponds to $-12dB$). They confirm that the behaviour corresponds to the desired one of a low-pass filter with a cutoff frequency of around $200kHz$.

6.4.3 *DC response*

Again referring to Fig. 6.14 and 6.15, the DC responses are reported in Fig. 6.18 and 6.19 respectively. They confirm that the opposing Zener diodes protect the ADC keeping the signals comfortably inside the required range. This is very important, especially for the current measurement channels, since in case of a short circuit, before the protections cut the supply, the current could reach very high values. It has also to be said that when the Zener diodes have a breakdown the output of the OPA4192 result shorted. Fortunately, this is not a problem since he OPA4192 presents built-in protection and can be shorted for an undefined amount of time (see datasheet [25]).

6.5 FAULT SIGNALS

Together with the signal coming from the current and voltage transducers each IPM board sends to one of the signal conditioning boards a fault signal coming from the IGBTs, which is high when everything is right, and set to zero by the internal logic when a problem occurs. There was the will to have a signal connected through an optocoupler directly to the Zynq-7000 ZC702 board where the FPGA and an integrated microprocessor are found. This signal needs to be triggered as soon as any of the 12 original fault signals is triggered, in order to be able to safely shut down the machine and investigate what caused the issue. Since a 12-inputs AND gate is not commercially available, the scheme of Fig. 6.20, which implies only 2-inputs and one 3-inputs AND gates, has been implemented. Each one of the three signal conditioning boards receives four fault signals. Let us name the boards "A", "B" and "C". In each of them with three 2-inputs AND gates, a 4-inputs AND gate is created and used to get a signal representative of the four IPMs that send the signals to that board, for example for board "A" we will refer to this signal as $FaultA\backslash$, where the "\" indicates that the signal is actually low when a fault occurs. The signals $FaultA\backslash$ and $FaultB\backslash$ are buffered and sent through wires to board "C". In this board the three signals $FaultA\backslash$, $FaultB\backslash$ and $FaultC\backslash$ become the inputs of a 3-ports AND gate in order to obtain the $Fault\backslash$ signal, comprehensive

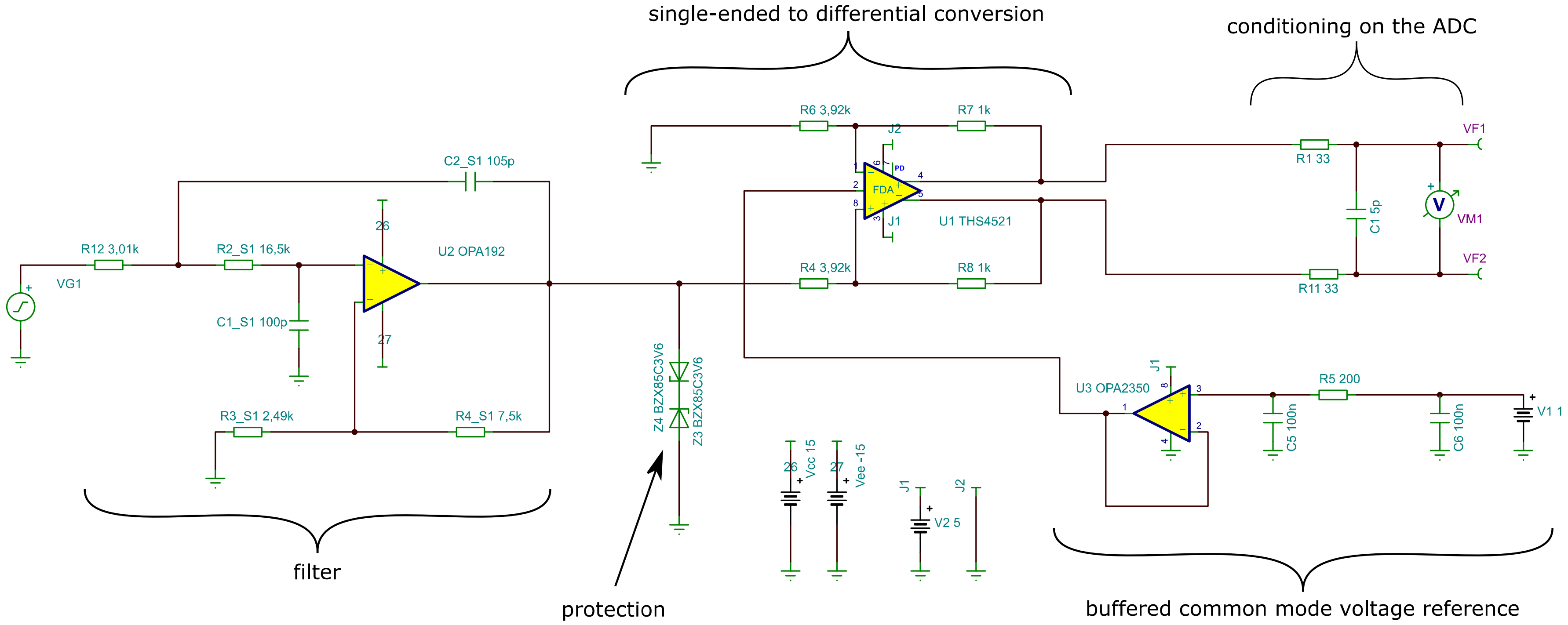

Figure 6.14: Complete scheme of one current measurement channel.

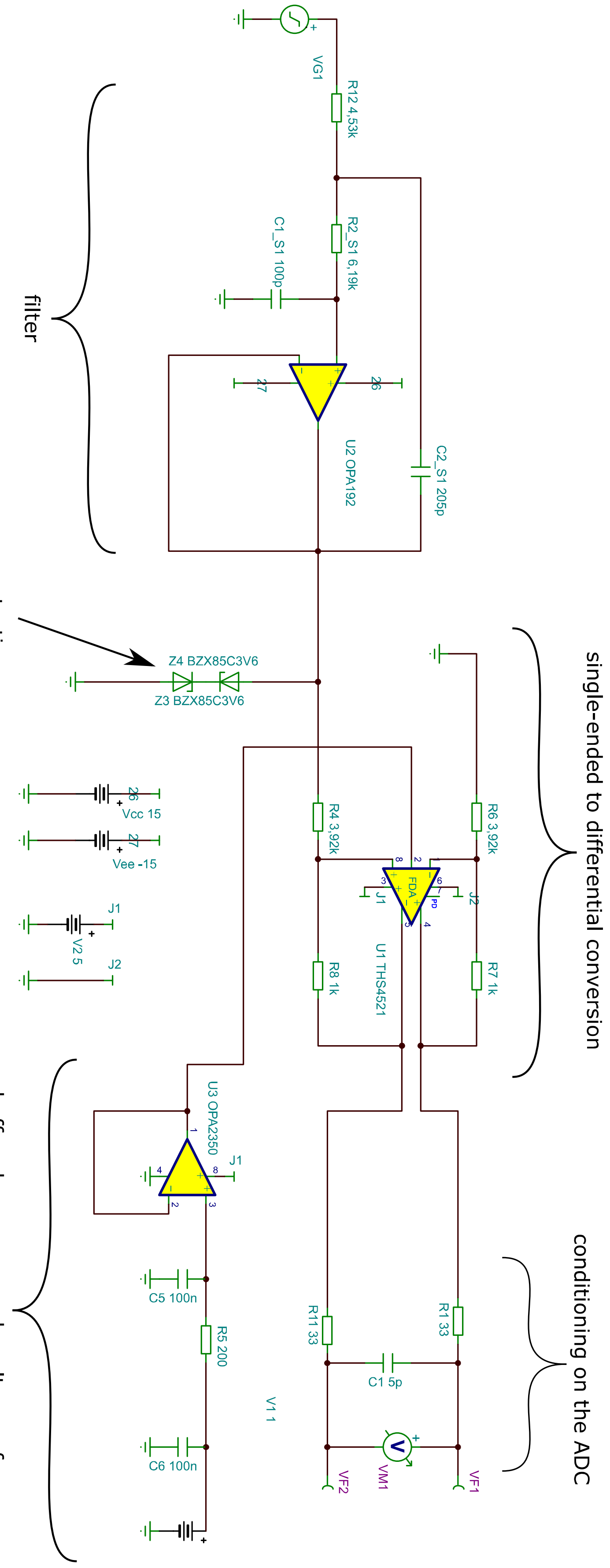

Figure 6.15: Complete scheme of one voltage measurement channel.

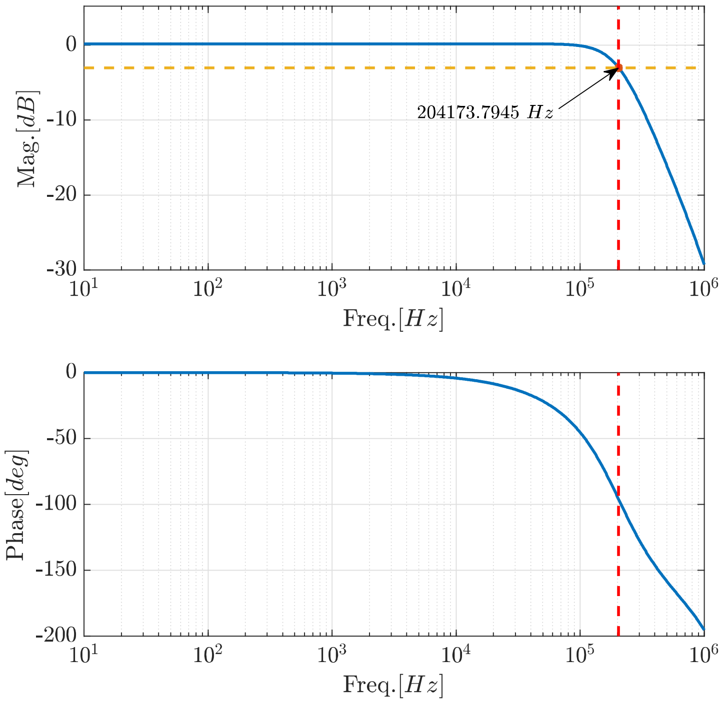

Figure 6.16: AC transfer characteristics of the current measuring channel.

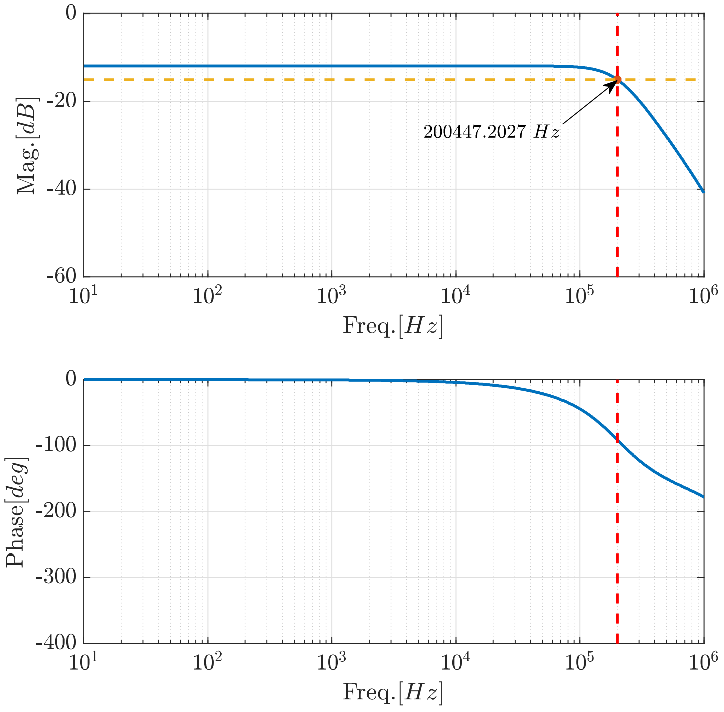

Figure 6.17: AC transfer characteristics of the voltage measuring channel.

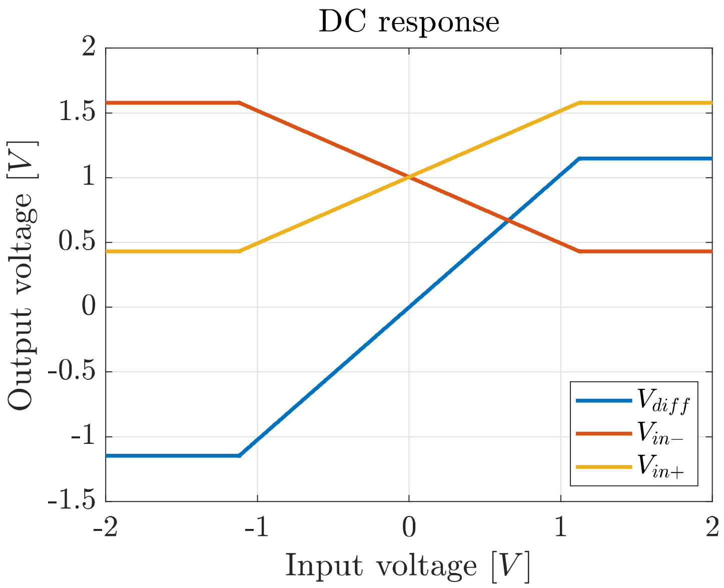

Figure 6.18: DC transfer characteristics of the current measuring channel.

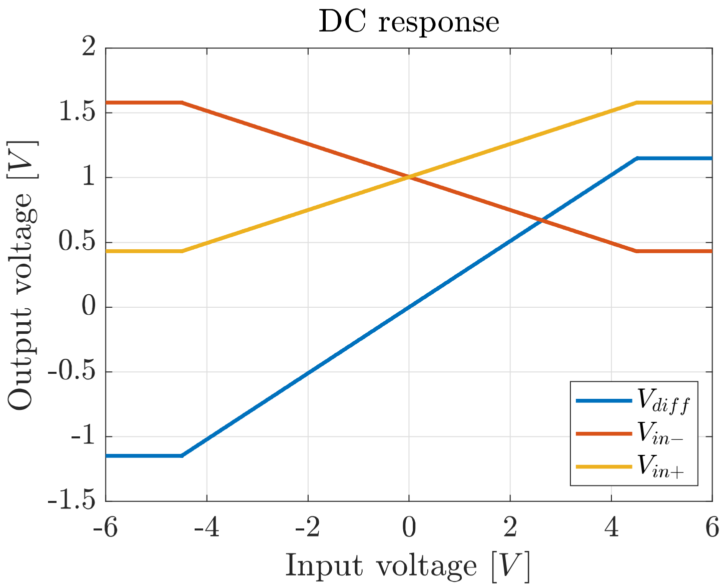

Figure 6.19: DC transfer characteristics of the voltage measuring channel.

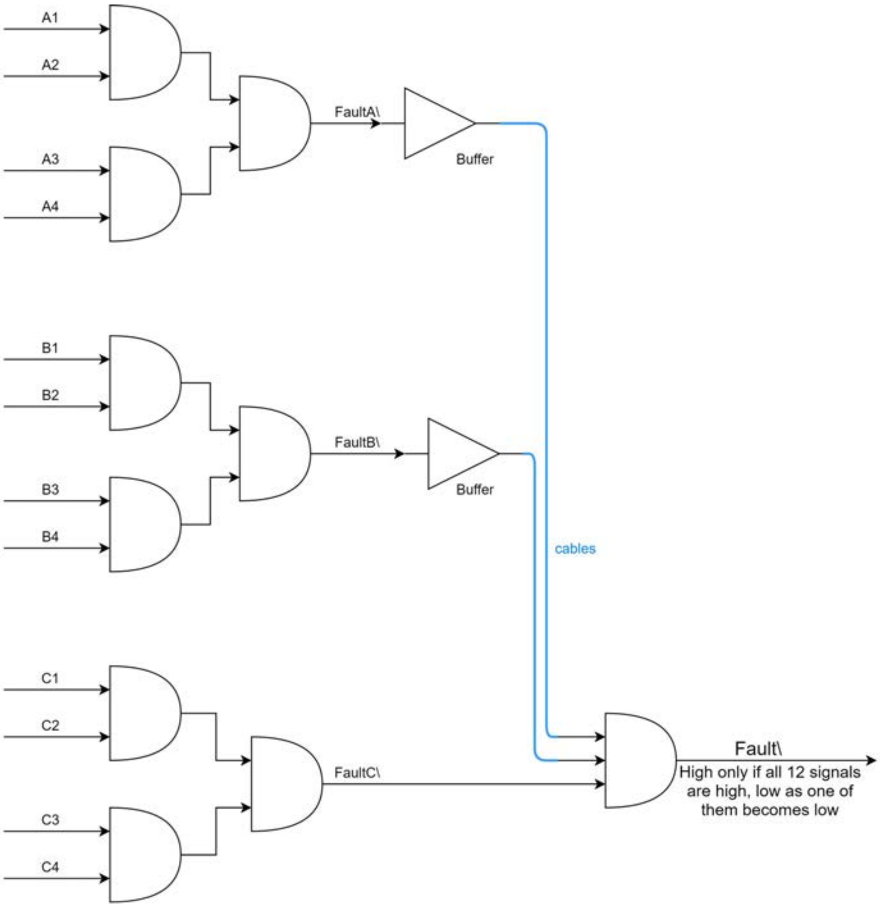

Figure 6.20: Fault signals management

of all the IGBTs. Finally, the signal is sent to the Zynq-7000 ZC702, but not before galvanically isolate it from the signal conditioning board "C" with the use of an optocoupler (the On Semiconductors FOD8173, datasheet [8]).

7

STABILITY ANALYISIS

In order to avoid unexpected behaviours once the boards were already built, some stability analyses have been performed, and are presented in this chapter.

It is common when dealing with the stability of operational amplifiers circuits to refer to the control loop equivalent scheme of Fig. 7.1, where:

- A_{ol} = open loop gain;
- β = feedback factor = $\frac{V_{fb}}{V_{out}}$;
- A_{cl} = closed loop gain = $\frac{A_{ol}}{1+A_{ol}\beta}$;
- $A_{ol}\beta$ = loop gain.

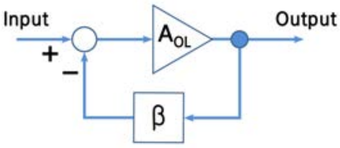

Figure 7.1: Control loop equivalent scheme of a feedback op amp circuit.

The circuit is unstable when $A_{ol}\beta = -1$, i.e. when $|A_{ol}\beta| = 0dB$ and $\angle(A_{ol}\beta) = 180°$. Thus, the phase margin is how close the system is to a 180° phase shift in $A_{ol}\beta$. For optimal stability, a rule of thumb states that a phase margin of 45° or higher is required. Issues happen because of too much delay from output to feedback. Many standard op amps circuits inadvertently create stability issues when external components interact with non-ideal amplifier's properties. For example, the open loop output impedance interacts with the circuit load capacitance to form a delay, or a feedback resistance interacts with the amplifier's input capacitance. There are many techniques to "break" the feedback loop of a circuit that can be represented by Fig. 7.1, and extract the $A_{ol}\beta$ loop gain Bode diagrams to check the phase margins.

The filter stage of the current and voltage measurement channel of the signal conditioning boards (see Fig. 6.4 and 6.5 respectively) present two feedback loops and the situation is better represented by the control loop equivalent of Fig. 7.2, where we can write:

- A_{ol} = open loop gain;
- β = feedback factor = $\beta_- - \beta_+$;

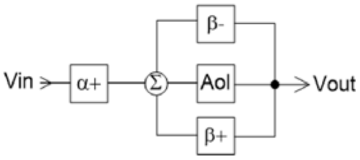

Figure 7.2: Control loop equivalent scheme of a dual feedback op amp circuit.

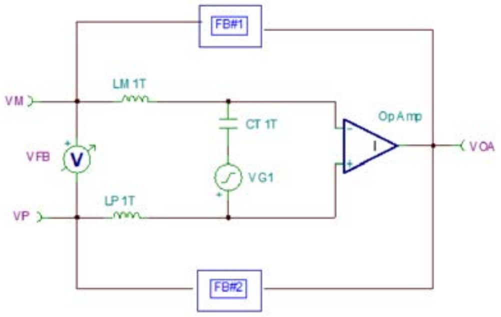

Figure 7.3: Double L Loop Gain Break Test circuit, example.

- A_{cl} = closed loop gain = $\frac{A_{ol}\alpha_{+}}{1+A_{ol}\beta}$;
- $A_{ol}\beta$ = loop gain.

In this cases, the loop gain can be extracted with a SPICE circuit simulator (like Tina-TI) with a so-called *Double L Loop Gain Break Test* [*], shown in Fig. 7.3. Referring to that circuit example $A_{ol}\beta = VFB$. The test has been performed for both the current measurement and the voltage measurement channels. The test circuits are shown in Fig. 7.4 and 7.6 respectively. The output stages have been loaded with the input impedance (from the datasheet) of the FDA THS4524 that would follow. The corresponding loop gain Bode diagrams for the current measurement channel of Fig. 7.5 reveal a phase margin of $180° - 84.3° = 95.7°$. The loop gain Bode diagrams for the voltage measurement channel of Fig. 7.7 reveal instead a phase margin of $180° - 112.93° = 67.07°$. In both cases, the phase margin results acceptable and any further actions should not be required. For the single-ended to differential conversion stage, i.e. for the FDA circuit, the control loop equivalent of Fig. 7.1 is still valid if as V_{in} and V_{out}, the differential input and differential output are considered. The loop gain test circuit, in this case, is shown in Fig. 7.8, where $A_{ol}\beta = VM1$. The circuit is loaded with the remaining elements of the analog front-ent of the AD9249-65EBZ after the modifications showed in 6.3.1, and with the differential input impedance of the AD9249, from its datasheet. The loop gain Bode diagrams of Fig. 7.9 reveal a phase margin of $180° - 90.76° = 89.24°$, which is pretty good. Anyhow just one decade

---

[*] Explained by Tim Green in: `https://e2e.ti.com/cfs-file/__key/communityserver-discussions-components-files/14/4048.Dual-FB-Beta_5F00_plus-and-Beta_5F00_minus-RevD.pptx`

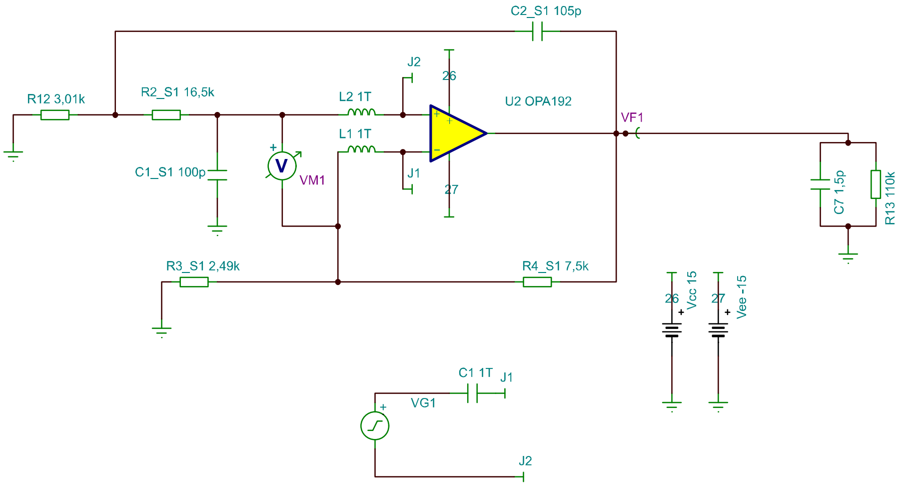

Figure 7.4: Double L Loop Gain Break Test circuit, filter of current measurement channel.

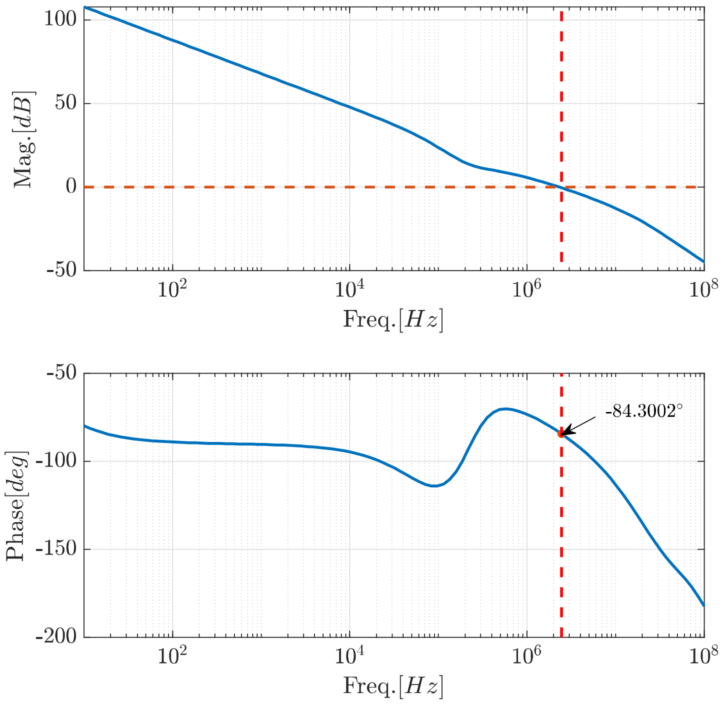

Figure 7.5: Loop gain AC transfer characteristics, filter of current measurement channel.

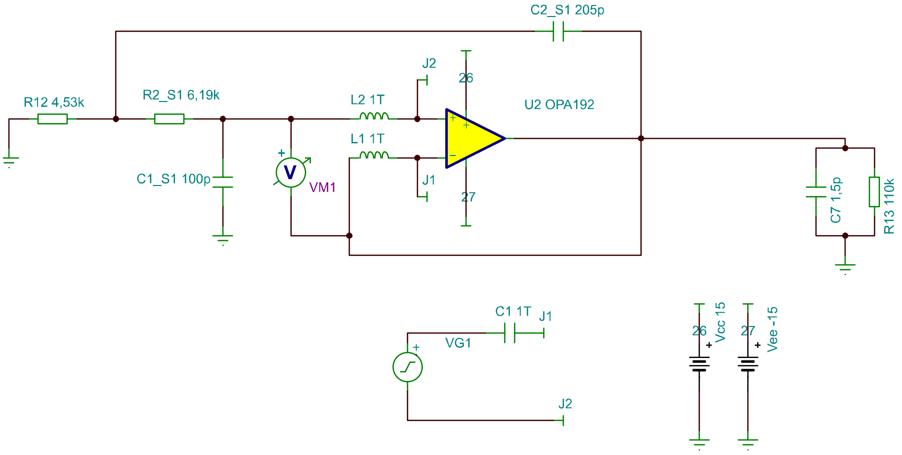

Figure 7.6: Double L Loop Gain Break Test circuit, filter of voltage measurement channel.

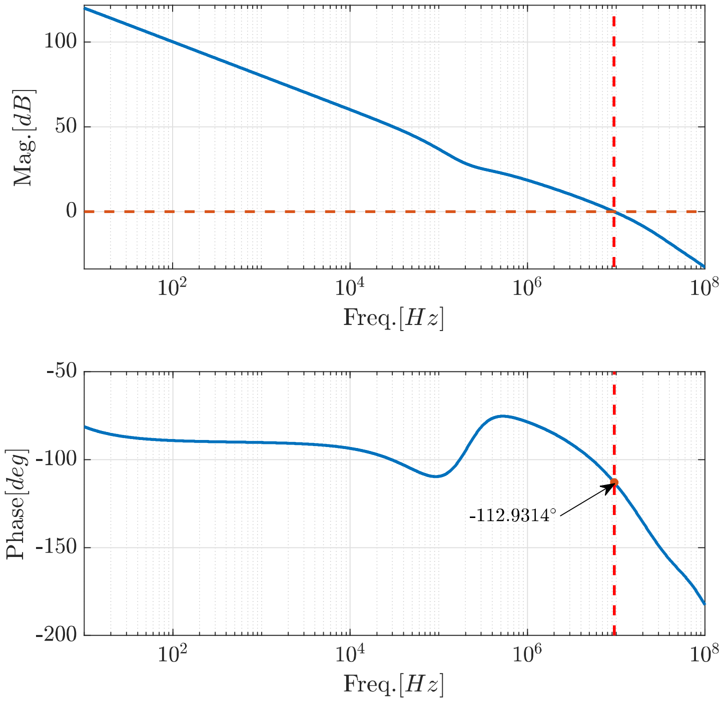

Figure 7.7: Loop gain AC transfer characteristics, filter of voltage measurement channel.

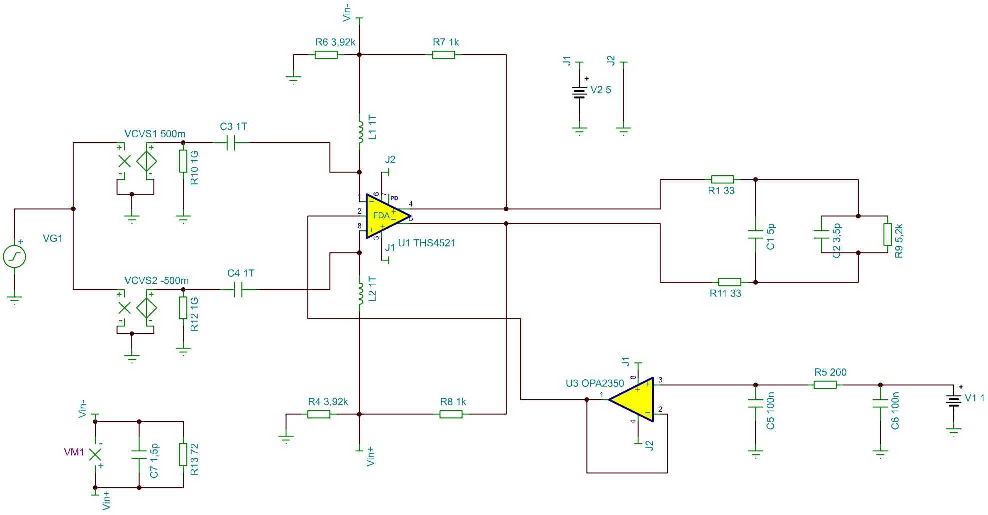

Figure 7.8: Loop gain test circuit, FDA.

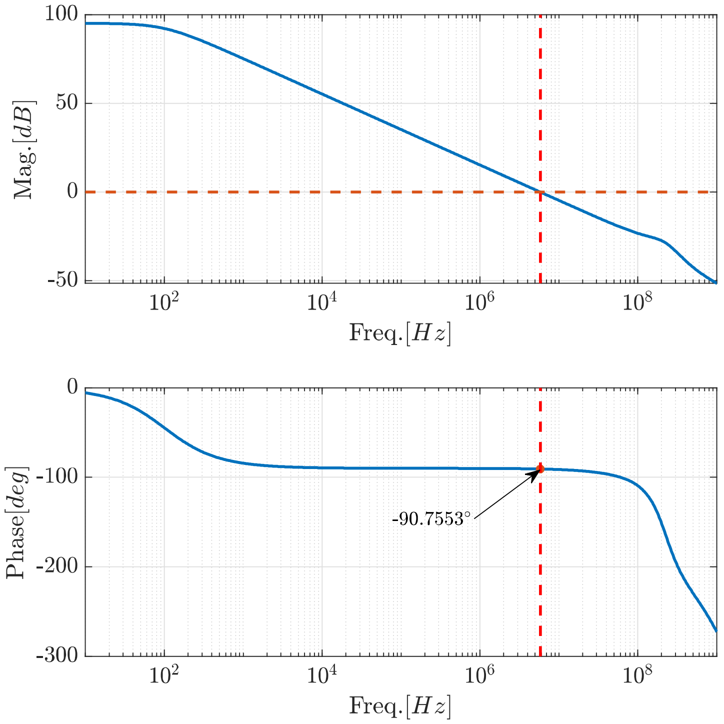

Figure 7.9: Loop gain AC transfer characteristics, FDA.

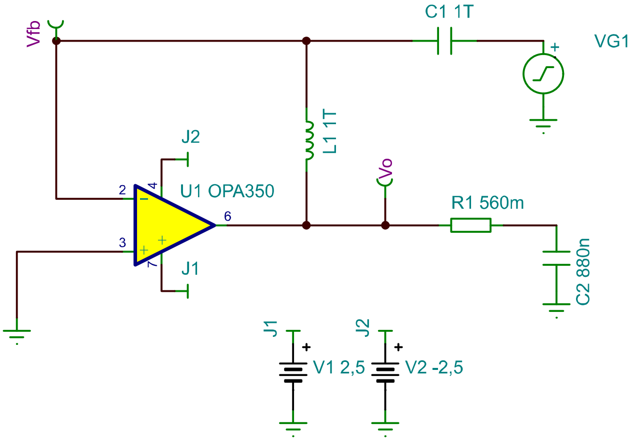

Figure 7.10: Loop gain test circuit, buffer of the FDA's V_{ocm} reference.

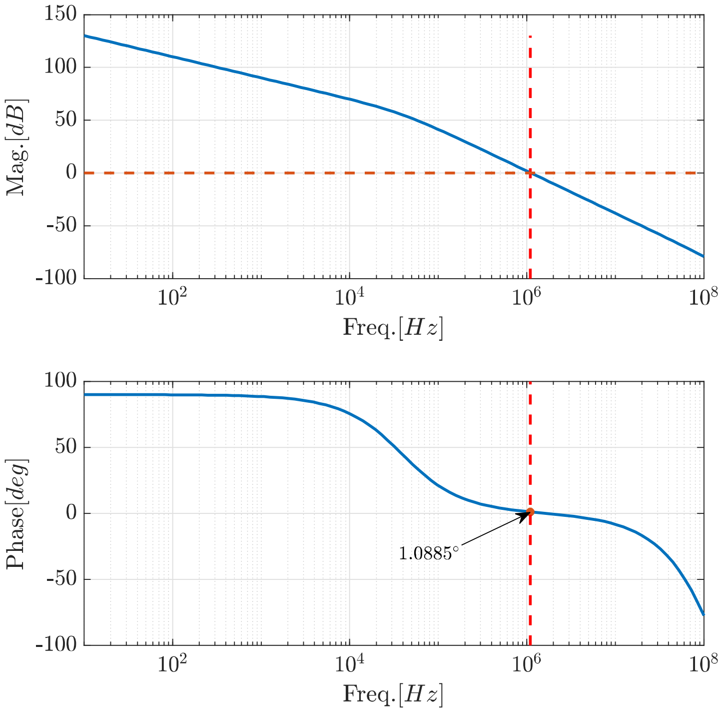

Figure 7.11: Loop gain AC transfer characteristics, buffer.

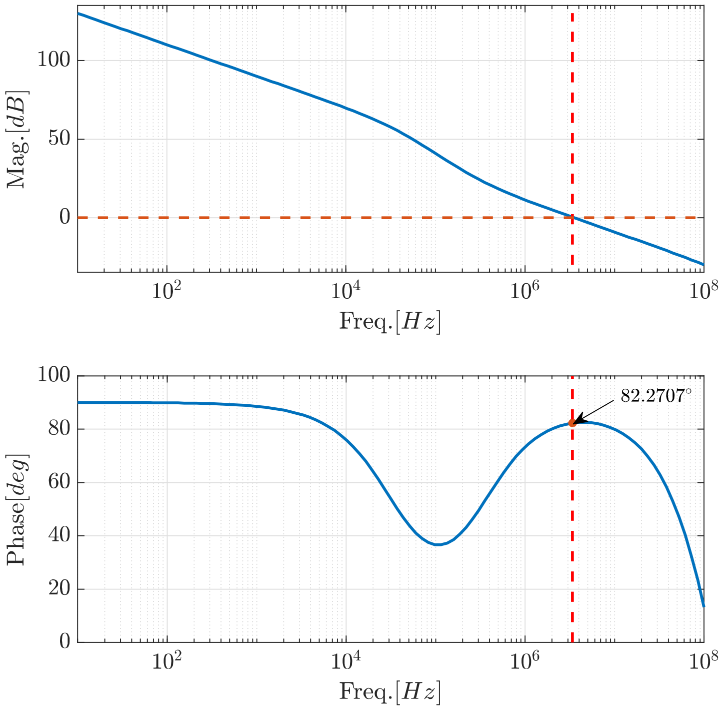

Figure 7.12: Loop gain AC transfer characteristics with added output isolation resistor, buffer.

after we can see a very rapid decade of the phase margin, due to the low gain of $1/4$. If any problems occur in real-life conditions it is suggested to take advantage of the *Noise Gain Shaping* technique explained in [11]. Since the *Vocm* common mode voltage reference input pin of the THS4524 requires, according to its datasheet, a $220nF$ filtering capacitor, also the stability of the buffer that drives that input has been checked. In each one of the three conditioning board, there is one buffer that drives four THS4524 *Vocm* pins. Thus, it has to be considered a capacitance of $880nF$ at the OPA350 output. The test circuit in this case is the one shown in Fig. 7.10, where $A_{ol}\beta = V_o$. In the original configuration the $560m\Omega$ resistor is not present and the obtained Bode diagrams of the loop gain, shown in Fig. 7.11, reveals a critical situation, with a phase margin of only $1.09°$. Fortunately, the problem can be easily solved with the very small isolation resistance of $560m\Omega$. This time, in fact, we can see from the Bode diagrams of the loop gain of Fig. 7.12 that we get a much better margin of $82.27°$. Usually, the problem with isolation resistors is the voltage drop but in our case from simulations, with such a small resistance, the voltage drop will be only a very few hundreds of μV, which is irrelevant, also considering that the common mode voltage, provided it is kept in the required range, does not affect the differential signal measure done by the ADC.

8

PCB DESIGN AND CONCLUSIONS

In this chapter, the design of the PCBs is briefly showcased, and finally, all the features implemented in the projected signal conditioning boards are summarised in the conclusions.

8.1 PCB DESIGN

The three PCBs have been designed with the help of the KiCad software. To keep things simple an economic two-layer design was chosen. The size of the boards is $26 \times 5cm$, the same of the IPMs, in order to be placed in the same stack. To further simplify space management in the stack, all the components have been placed only on one side of the board. When possible, the Surface-Mount Device (SMD) version of the needed components has been preferred, to take advantage of the solder hoven available at KTH laboratories. In addition, for the resistors and the ceramic capacitors the package 0805 was chosen. Even if it is oversized in most of the cases, its physical dimensions are small but not extremely small, making the handling and the board construction process less difficult. Only the high precision measuring resistors have a different package, and they are even bigger to ensure they do not overheat in case of an unfortunate event like a short circuit in the motor coils. The reason to have three separate boards is just related to the spacing between components, and to the will of not to have messy and intricate tracks with loads of vias. The design follows the basic rules and the good practices of PCB design: some examples are the Kelvin connetions for the measuring resistors, and the use of power planes, the biggest of which dedicated to ground.

Fig. 8.1 shows the rendering of the final design. Even though in Chapt. 6 when dealing with the faults signal management we talked about board "A" and "B" with the same circuit layout, and board "C" with a different one, the actual PCB design is unified, and the physical boards differ only for the installed components. The most important differences are highlighted in Fig. 8.1, as well as the main components of the signal conditioning path and the I/O connectors. The green connectors are used for power supply ($\pm 15V$ and $+5V$) as well as for the connection of the $1V$ common mode voltage reference for the single-ended to differential signal conversion, that comes from the AD9249. The four dark grey connectors are the input of the signals sent by the IPMs. Each one sends three current measurements, one voltage measurement, and one IGBT's fault signal. After being conditioned, the transducer's signal are outputted at the light blue connectors and

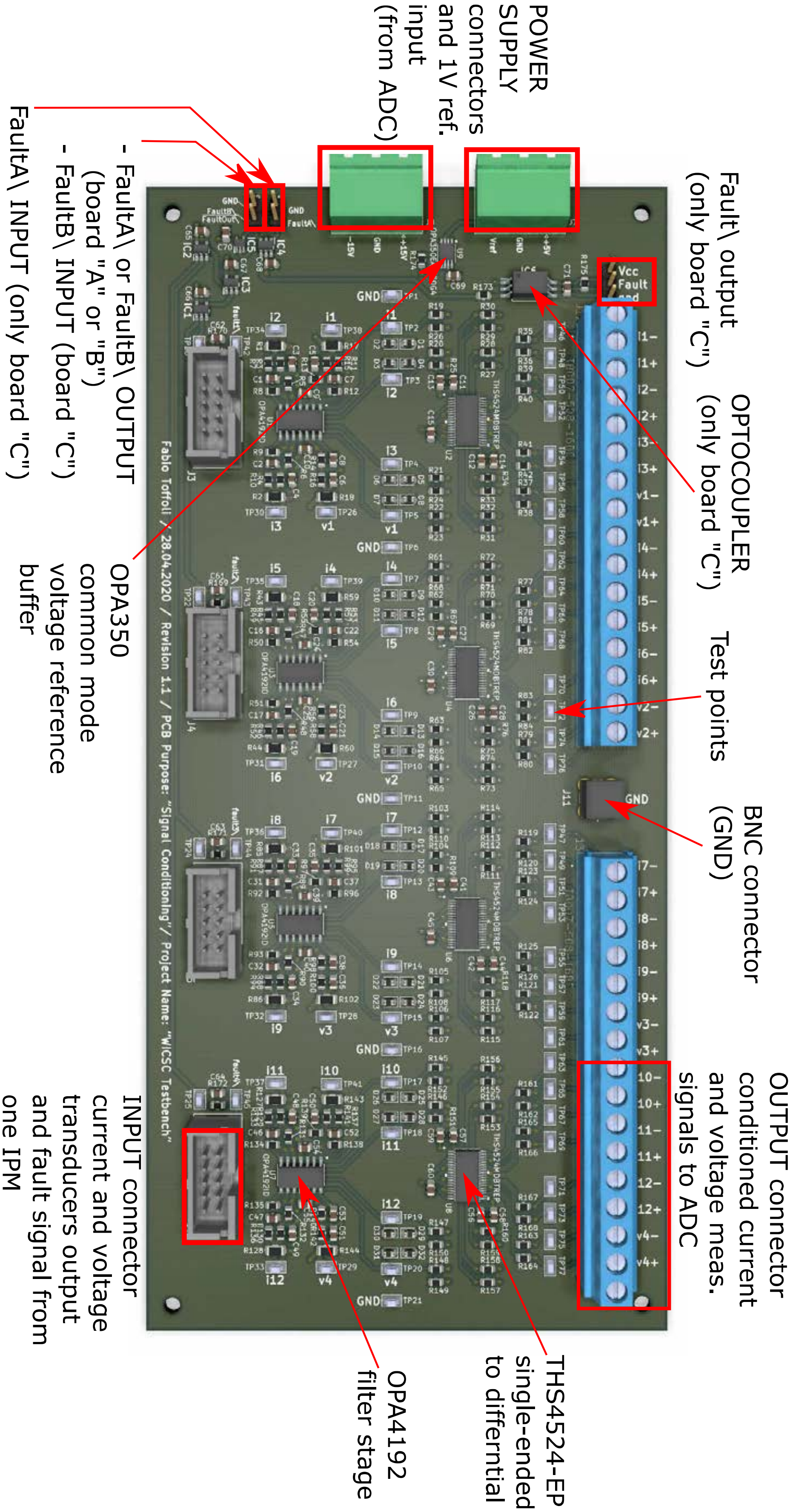

Figure 8.1: Rendering of the signal conditioning board, front side.

have to be sent through wires to the ADC. In between the two big light blue connectors find place a BNC connector for a connection via coaxial cable of the grounds of the signal conditioning board itself and of the AD9249-65EBZ (after the necessary modifications there are 16 "useless" BNC connectors on each board, any of them can be used for this purpose). The faults signals instead are manged as already explained in Chapt. 6, and only one board will have the optocoupler and the pins for the connection with the Zynq-7000 ZC702 installed.

Figure 8.2: Signal conditioning board picture.

8.2 CONCLUSIONS OF PART II

In this second and last part of the thesis, we have seen the most important reasonings done during the definition of the electrical schemes and of the PCB design of the signal conditioning boards. To conclude we can summarize all the features they integrate:

- transformation of current signals into voltage signals via measuring resistors;
- anti-aliasing filters with a cutoff frequency of around $200kHz$;
- conversion of single-ended signals into differential signals;
- ADC input protection with opposing Zener diodes;
- management of fault signals coming from the IGBTs, grouped into one single signal sent to the control system unit, with galvanic isolation thanks to an optocoupler.

The three signal conditioning boards have now been built. One of them is shown in Fig. 8.2. They are ready for testing at KTH laboratories.

CONCLUSIONS

In the first part of this work we have taken the first steps that are necessary to develop a control strategy for the WICSC prototype capable of dealing with a change of phase/pole configuration. After an introduction to the VSD method, used to exploit the increased degrees of freedom of regular MPMs, we have seen how unfortunately that was not perfect to deal with a switch of configuration during operation that the WICSC prototype can achieve. Thus we have presented the HPD theory and showed its potential. We have tested a control scheme based on HPD on a regular six-phase YY30 machine model and we managed to successfully switch between a six-phase mode and a three-phase mode on-the-fly. This example was pretty simple but yet the control scheme appears much more complex with respect to the one of a regular MPM. We also cited the steps necessary to adapt it for the WICSC prototype: first a change in the number of pole pairs needs to tested, then a mirrored 18-phase base-case control scheme needs to be implemented in order to deal with the possible unbalances between two coils belonging to the same virtual phase of the base-case.

In the second part we have shown the project of three signal conditioning boards that will be part of the final setup of the WICSC prototype test-bench. They receive signals generated in the IPMs boards, coming from current and voltage transducers as well as the fault signals of the IGBTs. The signal from the transducers are adapted to the ADC input requirements, whereas the fault signals are grouped and sent to the main control board, where the FPGA and the microprocessor are situated. We have shown the problems that arose with the ADC board analog front end configuration and how they have been fixed. We showed the project of the electrical schemes that have been implemented to achieve all the required features of the boards. Finally, the PCB design has been showcased. The boards will be soon tested at KTH laboratories.

BIBLIOGRAPHY

[1] *AD9249, 16 Channel, 14-Bit, 65 MSPS, Serial LVDS, 1.8 V ADC*. Datasheet. Analog Devices, Inc., 2013. URL: `https://www.analog.com/media/en/technical-documentation/data-sheets/AD9249.pdf`.

[2] *Analysis of the Sallen-Key Architecture*. Application Report. Texas Instruments, Inc., Sept. 2002. URL: `https://www.ti.com/lit/an/sloa024b/sloa024b.pdf`.

[3] Konstantina Bitsi, Oskar Wallmark, and Sjoerd Bosga. "An Induction Machine with Wound Independently-Controlled Stator Coils." In: *2019 22nd International Conference on Electrical Machines and Systems (ICEMS)* (2019). DOI: `10.1109/icems.2019.8921779`.

[4] *Current Transducer LA 100-P*. Datasheet. LEM Europe GmbH, Nov. 2018. URL: `https://www.lem.com/sites/default/files/products_datasheets/la_100-p_e_.pdf`.

[5] Gurakuq Dajaku and Dieter Gerling. "Low costs and high efficiency asynchronous machine with stator cage winding." In: *2014 IEEE International Electric Vehicle Conference (IEVC)* (2014). DOI: `10.1109/ievc.2014.7056083`.

[6] Obrad Dordevic, Martin Jones, and Emil Levi. "A Comparison of Carrier-Based and Space Vector PWM Techniques for Three-Level Five-Phase Voltage Source Inverters." In: *IEEE Transactions on Industrial Informatics* 9 (2013), pp. 609–619. ISSN: 1551-3203. DOI: `10.1109/tii.2012.2220553`.

[7] Mario J. Duran, Emil Levi, and Federico Barrero. "Multiphase Electric Drives: Introduction." In: *Wiley Encyclopedia of Electrical and Electronics Engineering, J.G. Webster (Ed.)* (), pp. 1–26. DOI: `10.1002/047134608x.w8364`.

[8] *FOD8173, FOD8173T, 3.3 V/5 V, 20 Mbit/sec, LogicGate Optocoupler inStretched Body SOP 6-Pin*. Datasheet. ON Semiconductor, Semiconductor Components Industries, Aug. 2018. URL: `https://www.onsemi.com/pub/Collateral/FOD8173-D.PDF`.

[9] J. Faiz and I. Tabatabaei. "Extension of winding function theory for nonuniform air gap in electric machinery." In: *IEEE Transactions on Magnetics* 38 (2002), pp. 3654–3657. ISSN: 0018-9464. DOI: `10.1109/tmag.2002.804805`.

[10] C. L. Fortescue. “Method of Symmetrical Co-Ordinates Applied to the Solution of Polyphase Networks.” In: *Transactions of the American Institute of Electrical Engineers* XXXVII (Aug. 1918), pp. 1027–1140. ISSN: 0096-3860. DOI: `10.1109/t-aiee.1918.4765570`.

[11] Jacob Freet. *Using noise-gain shaping to stabilizefully-differential amplifiers*. Design Guidelines. Texas Instruments, Inc., 2017. URL: `https://www.ti.com/lit/an/slyt733/slyt733.pdf`.

[12] S. Gataric. “A polyphase cartesian vector approach to control of polyphase AC machines.” In: *Conference Record of the 2000 IEEE Industry Applications Conference. Thirty-Fifth IAS Annual Meeting and World Conference on Industrial Applications of Electrical Energy* (Oct. 2000). DOI: `10.1109/ias.2000.882102`.

[13] D. Gerling, G. Dajaku, F. Bachheibl, and A. Patzak. “Analytical calculation of the novel Stator Cage Machine.” In: *18th International Conference on Electrical Machines and Systems (ICEMS)* (Oct. 2015). DOI: `10.1109/icems.2015.7385248`.

[14] Gabriele Grandi, Jelena Loncarski, and Roland Seebacher. “Effects of current ripple on dead-time distortion in three-phase voltage source inverters.” In: *2012 IEEE International Energy Conference and Exhibition (ENERGYCON)* (2012). DOI: `10.1109/energycon.2012.6347753`.

[15] T. M. Jahns. “IEEE Transactions on Industry Applications.” In: *IEEE Transactions on Industry Applications* 16 (3) (1980), pp 321–331. ISSN: 0093-9994. DOI: `10.1109/tia.1980.4503814`.

[16] Jim Karki. *Active Low-Pass Filter Design*. Application Report. Texas Instruments, Inc., 2002. URL: `https://www.ti.com/lit/an/sloa049b/sloa049b.pdf`.

[17] Jim Karki. *Using Single-Supply Fully Differential Amplifiers With-Negative Input Voltages to Drive ADCs*. Application Report. Texas Instruments, Inc., Nov. 2010. URL: `https://www.ti.com/lit/an/slyt394/slyt394.pdf`.

[18] E. Levi. “Multiphase Electric Machines for Variable-Speed Applications.” In: *IEEE Transactions on Industrial Electronics* 55 (2008), pp. 1893–1909. ISSN: 0278-0046. DOI: `10.1109/tie.2008.918488`.

[19] E. Levi, R. Bojoi, F. Profumo, H. A. Toliyat, and S. Williamson. “Multiphase induction motor drives - a technology status review.” In: *IET Electric Power Applications* 1 (2007), p. 489. ISSN: 1751-8660. DOI: `10.1049/iet-epa:20060342`.

[20] T. A. Lipo. *Transient Analysis of Synchronous Machines*. CRC Press, 2017, pp. 265–313. DOI: `10.1201/b12211-5`.

[21] Zicheng Liu, Yongdong Li, and Zedong Zheng. "A review of drive techniques for multiphase machines." In: *CES Transactions on Electrical Machines and Systems* 2 (2018), pp. 243–251. ISSN: 2096-3564. DOI: 10.30941/cestems.2018.00030.

[22] Jano Malvar, Oscar Lopez, Alejandro G. Yepes, Ana Vidal, Francisco D. Freijedo, Pablo Fernandez-Comesana, and Jesus Doval-Gandoy. "Graphical Diagram for Subspace and Sequence Identification of Time Harmonics in Symmetrical Multiphase Machines." In: *IEEE Transactions on Industrial Electronics* 61 (2014), pp. 29–42. ISSN: 0278-0046. DOI: 10.1109/tie.2013.2242415.

[23] Ron Mancini. *Op Amps For Everyone: Design Refrence*. Texas Instruments, Inc., Aug. 2002. URL: https://web.mit.edu/6.101/www/reference/op_amps_everyone.pdf.

[24] A. R. Munoz and T. A. Lipo. "Complex vector model of the squirrel-cage induction machine including instantaneous rotor bar currents." In: *IEEE Transactions on Industry Applications* 35 (1999), pp. 1332–1340. ISSN: 0093-9994. DOI: 10.1109/28.806047.

[25] *OPAx192 36-V, Precision, Rail-to-Rail Input/Output, Low Offset Voltage, Low Input Bias Current Op Amp with e-trim^{TM}*. Datasheet. Texas Instruments, Inc., Mar. 2015. URL: https://www.ti.com/lit/ds/symlink/opa192.pdf.

[26] *OPAx350 High-Speed, Single-Supply, Rail-to-Rail Operational Amplifiers MicroAmplifierSeries*. Datasheet. Texas Instruments, Inc., Dec. 2015. URL: https%3A%2F%2Fwww.ti.com%2Fproduct%2FOPA350.

[27] Gustaf Falk Olson, Yixuan Wu, Luca Peretti, and Oskar Wallmark. "Harmonic Plane Decomposition: An Extension of the Vector-Space Decomposition - Part II." In: *Proceedings of the 46th Annual Conference of the IEEE Industrial Electronics Society (IECON), Singapore* (Oct. 2020). To be presented.

[28] Luca Peretti and Giovanni Zanuso. "Technology aspects and analytical modelling of multi-phase synchronous and induction machines." Sept. 2019.

[29] A. A. Rockhill and T. A. Lipo. "A generalized transformation methodology for polyphase electric machines and networks." In: *2015 IEEE International Electric Machines & Drives Conference (IEMDC)* (2015). DOI: 10.1109/iemdc.2015.7409032.

[30] S. Runde, A. Baumgardt, O. Moros, B. Rubey, and D. Gerling. "ISCAD - Design, control and car integration of a 48 volt high performance drive." In: *CES Transactions on Electrical Machines and Systems* 3 (2019), pp. 117–123. ISSN: 2096-3564. DOI: 10.30941/cestems.2019.00017.

[31] Evan Sawyer. *Single-ended-to-differential circuit using an op amp andfully-differential amplifier (FDA) for bipolar signals*. Design Guidelines. Texas Instruments, Inc., Aug. 2019. URL: `https://www.ti.com/lit/an/sbaa246a/sbaa246a.pdf`.

[32] *THS4524-EP, VERY LOW POWER, NEGATIVE RAIL INPUT, RAIL-TO-RAIL OUTPUT,FULLY DIFFERENTIAL AMPLIFIER*. Datasheet. Texas Instruments, Inc., Nov. 2013. URL: `https://www.ti.com/product/THS4524-EP?qgpn=ths4524-ep`.

[33] A. Tessarolo. "Modeling and analysis of multiphase electric machines for highpower applications." PhD thesis. University of Padova, School of Industrial Engineering, Jan. 2011. URL: `http://paduaresearch.cab.unipd.it/4076/1/PHD_THESIS.pdf`.

[34] H. A. Toliyat, T. A. Lipo, and J. C. White. "Analysis of a concentrated winding induction machine for adjustable speed drive applications. II. Motor design and performance." In: *IEEE Transactions on Energy Conversion* 6 (1991), pp. 684–692. ISSN: 0885-8969. DOI: `10.1109/60.103642`.

[35] *Voltage transducer LV 25-P/SP*. Datasheet. LEM Europe GmbH, Sept. 2014. URL: `https://www.lem.com/sites/default/files/products_datasheets/lv_25-p_sp5.pdf`.

[36] E. E. Ward and H. Härer. "Preliminary investigation of an invertor-fed 5-phase induction motor." In: *Proceedings of the Institution of Electrical Engineers* 116 (1969), p. 980. ISSN: 0020-3270. DOI: `10.1049/piee.1969.0182`.

[37] S. Williamson and S. Smith. "Pulsating torque and losses in multiphase induction machines." In: *IEEE Transactions on Industry Applications* 39 (2003), pp. 986–993. ISSN: 0093-9994. DOI: `10.1109/tia.2003.813722`.

[38] Yixuan Wu, Gustaf Falk Olson, Luca Peretti, and Oskar Wallmark. "Harmonic Plane Decomposition: An Extension of the Vector-Space Decomposition - Part I." In: *Proceedings of the 46th Annual Conference of the IEEE Industrial Electronics Society (IECON), Singapore* (Oct. 2020). To be presented.

[39] Alejandro G. Yepes, Jesus Doval-Gandoy, Fernando Baneira, Diego Perez-Estevez, and Oscar Lopez. "Current Harmonic Compensation for n -Phase Machines With Asymmetrical Winding Arrangement and Different Neutral Configurations." In: *IEEE Transactions on Industry Applications* 53 (2017), pp. 5426–5439. ISSN: 0093-9994. DOI: `10.1109/tia.2017.2722426`.

[40] Y. Zhao and T. A. Lipo. "Space vector PWM control of dual three phase induction machine using vector space decomposition." In: *Proceedings of 1994 IEEE Industry Applications Society Annual Meeting* (). DOI: `10.1109/ias.1994.345429`.

[41] Y. Zhao and T. A. Lipo. "Modeling and control of a multiphase induction machine with structural unbalance." In: *IEEE Transactions on Energy Conversion* 11 (1996), pp. 570–577. ISSN: 0885-8969. DOI: 10.1109/60.537009.